PROBABILISTIC SEISMIC INVERSION BASED ON ROCK-PHYSICS

MODELS FOR RESERVOIR CHARACTERIZATION

A DISSERTATION

SUBMITTED TO THE DEPARTMENT OF GEOPHYSICS

AND THE COMMITTEE ON GRADUATE STUDIES

OF STANFORD UNIVERSITY

IN PARTIAL FULFILLMENT OF THE REQUIREMENTS
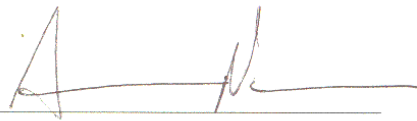
FOR THE DEGREE

OF DOCTOR OF PHILOSOPHY
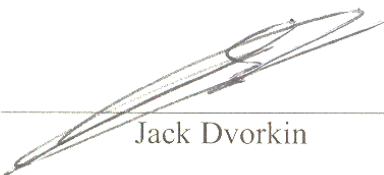

Kyle Thomas Spikes

January 2008

I certify that I have read this dissertation and that, in my opinion, it is fully adequate in scope and quality as a dissertation for the degree of Doctor of Philosophy.

Amos Nur (Principal Adviser)

I certify that I have read this dissertation and that, in my opinion, it is fully adequate in scope and quality as a dissertation for the degree of Doctor of Philosophy.

Jack Dvorkin

I certify that I have read this dissertation and that, in my opinion, it is fully adequate in scope and quality as a dissertation for the degree of Doctor of Philosophy.
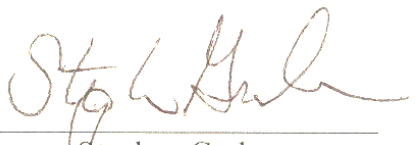
Tapan Mukerji

I certify that I have read this dissertation and that, in my opinion, it is fully adequate in scope and quality as a dissertation for the degree of Doctor of Philosophy.

Gary Mavko

I certify that I have read this dissertation and that, in my opinion, it is fully adequate in scope and quality as a dissertation for the degree of Doctor of Philosophy.

Stephan Graham

Approved for the University Committee on Graduate Studies

Abstract

This dissertation addresses recurrent questions in hydrocarbon reservoir characterization. What properties of rock stand behind recorded seismic reflections? How and to what extent can these rock properties be quantified from these reflections. To answer these questions, I link reservoir thickness, lithology, porosity, and saturation to seismic data by coupling deterministic rock-physics relationships and Bayesian statistics. The key innovation is a seismic-inversion method that functions on the principles of deterministic physics *and* probabilistically accounts for possible variations of rock properties within a potential reservoir unit. This is intended for use in *practical* reservoir characterization. Within it, I engage into the *fundamental* issue of reconciling spatial scale differences between seismic imaging, geology and stratigraphy, and rock physics.

Seismic-based reservoir characterization is an inherently non-unique problem. This ambiguity necessitates the use of statistical method to constrain the problem and quantify an associated uncertainty. This dissertation contributes to both deterministic and statistical seismic-based reservoir characterization. Complementary, I examined empirical velocity-porosity transforms to determine their consistencies with fluid-substitution equations. Results indicated that some transforms do not require an intermediate fluid-substitution step to provide accurate porosity values when brine is not the *in situ* fluid. Work done on deterministic reservoir characterization combined multiple elastic prop-

erties to simultaneously predict lithology and porosity with a constant fluid-saturation value. If a relationship between lithology and porosity was established, then the problem reduced to allow lithology and porosity to be estimated from a combination of P-impedance and Poisson's ratio.

The probabilistic reservoir-characterization technique simultaneously predicts up to four reservoir properties and associated uncertainty corresponding to a reflection from a potential reservoir unit. This involves exhaustive forward modeling of the prior model and a full-grid search in the inverse problem. A seismic- and well-data set from offshore Africa provided the basis to develop and perform the inversion. Inversion results included predictions of combinations of reservoir thickness, porosity, and saturation that matched well data within the limits of the associated uncertainty. Lithology predictions for the data set, however, were too uncertain to provide a full solution. An additional application to North Sea data demonstrated that if seismic resolution was high enough, then the inversion provided independent predictions of thickness and porosity. Given these results, the inversion technique lays the foundation for the decomposition of a measured seismic reflection into combinations of probabilistic reservoir properties. In the future, this method could readily be extended to incorporate other types of geophysical data to refine the predictions of reservoir properties in hydrocarbon exploration settings.

Acknowledgments

First, I want to express my thankfulness to my advisers. I consider each member of my committee as one. Beginning with Amos Nur, he is the one that made me feel that the door to Stanford was open when I was applying to schools. Throughout my time here, the questions Amos asked helped me to set the specific goals laid out in this dissertation. Second, I thank Jack Dvorkin for all the help on making me finish the solution and not settle for the 80% one. This happened many times, and he was so diligent in getting me to make the one last push. Next is Tapan Mukerji. If a question needed answered, he was the one person I knew who could answer it and make me to understand it. Gary Mavko, through his sense of humor and clear sense of practicality, provided many enjoyable conversations that kept me from going off on unrelated tangents. Steve Graham always provided that bit of rationale on the geologic side that always seemed to be just out of reach. Thank you, Amos, Jack, Tapan, Gary, and Steve for the outstanding help and friendship. It was an honor and privilege to have you all as advisers.

A great deal of thanks goes to the SRB program and all its sponsors for the funding and support during my time here. Without this generous support, the time here would not have been possible, nor would I have been allowed the freedom to choose this research topic. Along with that, I express thanks to Margaret Muir for her amazing ability to help with every situation that presented itself. Thanks in addition to Fuad Nijim for making sure that all complications that arose were taken care of. You deserve a standing ovation.

Jacob, Warren, and Dawn. Thanks to all who shared a good time or two with me, the list of which is too long to include.

One person who helped me get this far is my friend, mentor, and former adviser – Don Steeples. Years ago he convinced me that research could be fun. He was right. He convinced me to apply and to go Stanford. He was right. He told me that after I finished here that I would have options. He was right. Thanks, Don. I owe you a great deal of appreciation that these words cannot fully describe.

I thank my best friend from pre-school who did not make it, but who helped me through some tough times. To Dr. Heath J Schroeder: I wish we could have spoken now. We could have talked about finishing school, starting careers, while revisited fond memories. Your family, Kim, Karolyn, and Heather will always be in my thoughts. I wish you could have been here.

Last but certainly not least, I thank my family. Although sometimes they never thought I would finish, they always were encouraging, supportive, and patient. Without them, I would not have accomplished this goal. I dedicate this dissertation with all my heart and soul to my mother – Kay, my father – Kirk, my sisters and brother-in-law – Leslie, Amanda, and Dave, and my niece – Emory. Thank you.

Contents

List of Tables

List of Figures

Chapter 1
Introduction

"It would be an unsound fancy and self-contradictory to
expect that things which have never yet been done can be
done except by means which have never yet been tried."
--Francis Bacon

1.1 Motivation and objectives

Characterizing the subsurface of the Earth using geophysical remote-sensing technology is inherently an ambiguous problem. Many geophysical methods have been applied to solve this dilemma, but none provide the means or resolution to characterize the subsurface exhaustively or at a scale fine enough for estimating petroleum reserves. The hydrocarbon industry commonly and predominantly uses one such method: reflection seismology. Arguably, only this technique can characterize large volumes of the earth using responses to seismic waves.

Seismic-based descriptions of a subsurface volume, however, lack uniqueness and resolution. One reason is that the heterogeneous and complex earth distorts and attenuates seismic waves, which makes image focusing challenging. Even if these focusing issues are adequately addressed, seismic reflections can constrain only one or two elastic

properties at a point in space, although the traveling wave actually samples a large sub-volume in the earth. Furthermore, the seismic reflections depend on contrasts of the elastic properties, and each elastic property depends on several rock parameters (e.g., porosity, mineralogy, pore fluid, differential pressure). Nevertheless, the hydrocarbon industry must try to extract multiple petroleum-reservoir properties from these inherently limited inputs.

A typical reservoir characterization problem consists of quantitatively mapping a single seismic reflection into reservoir properties, namely thickness, lithology, porosity, and saturation. This task requires that all the wave-propagation effects, sampling, as well as noise issues, must be accounted for properly to provide an accurate translation of the elastic properties (velocity and/or impedance) into reservoir properties. Even with appropriate corrections for these problems, ambiguity still exists in relating elastic rock properties to reservoir properties. Rock-physics relationships allow point-by-point translations of elastic properties to reservoir properties. They do not, however, provide unique one-to-one mappings of elastic properties to reservoir properties. Most importantly, laboratory-scale rock-physics relations are not valid at the seismic scale, because seismic data represent some average of the rock properties. Seismic reservoir characterization, therefore, requires simultaneously linking point-based rock-physics relationships to band-limited seismic data and statistical methods to account for the ambiguous relationships between elastic and reservoir properties. Statistical inversion methods afford this linkage through the implementation of appropriate, physically based assumptions and prior information where necessary. The assumptions constrain the problem, and the prior information introduces controlled uncertainty into a potentially incomplete deterministic solution.

This dissertation presents contributions to both deterministic and probabilistic seismic reservoir characterization. In addition, rock-physics work analyzes the consistency of the Gassmann (1951) equation with two porosity-velocity relationships. This latter piece can be viewed as separate from the reservoir-characterization work. The deterministic tool serves as a prelude to the more sophisticated probabilistic reservoir-characterization tool.

The main contribution of this thesis is a Bayesian seismic-inversion method that accounts for possible variations of rock properties within a potential reservoir unit. It is a trace-based algorithm that requires a prior interpretation of the seismic data to identify the potential reservoir interval. Within that potential reservoir unit, the inversion algorithm combines prior information with a likelihood function based on correlations of real and synthetic seismic data. Outputs are trace-to-trace posterior distributions of continuous variables. These distributions account for uncertainty in the seismic data to provide probabilistic estimates of thickness, clay content, porosity, and saturation. Most importantly, this method combines point-based rock-physics relationships and band-limited seismic data, and it treats each properly at its own respective scale. As a result, this method requires neither downscaling of the seismic data nor upscaling of the rock-physics relationships.

The forward problem consists of an exhaustive simulation of the reservoir properties within the potential reservoir unit. A complete set of three-layer earth models results. By operating on a single unit instead of an entire seismic volume, the problem is reduced to allow this exhaustive simulation. An appropriate rock-physics transform translates the earth models to elastic models. A convolutional P-P ray-tracing algorithm generates the corresponding complete set of seismic models.

At the core of the statistical algorithm is the likelihood function calculation, encompassing an acceptance/rejection criterion within a full-grid search. Correlations between real and synthetic seismic traces and the number of accepted synthetic traces control the width and shape of the non-parametric likelihood function. Accordingly, sampling of the prior or posterior distributions is not necessary. Although it requires no formal objective function, the goal of the inversion is to maximize the correlation between synthetic and real data while minimizing the number of synthetic traces that are accepted in the full-grid search.

This work has a clear impact on *practical* reservoir characterization. Within it, I have progressed towards a synthesis of several still-disparate pieces of earth science—seismic imaging; geology and stratigraphy; statistics; and last but not least, rock physics—to

reveal the rock properties behind the seismic amplitude. At the same time, I have addressed the *fundamental* question of scale and interconnection of various properties of the subsurface. Specifically, how might we derive rock properties relevant to reserve and production forecasts from coarse-scale remote sensing? One result from this inversion technique indicates that although it may not be possible to predict porosity and geometric quantities separately, the product of the two provides a fairly robust and reliable output.

The two primary foundations of this methodology are statistics and rock physics. For the former, Tarantola (1987); Malinverno and Parker (2006); Scales and Tenorio (2001); and Takahashi (2000) provide the primary references. The rock physics is described by Mavko et al. (1998), Avseth et al. (2005), Avseth (2000), and Gutierrez (2001). Although the method does not include a geostatistical basis or account for spatial uncertainty, work by Gonzalez (2006) and Bosch (2004) could be extended to characterize the uncertainty in the inversion.

1.2 Chapter description

Chapter 2 examines the consistency between the Gassmann (1951) equation and the Raymer et al. (1980) and Wyllie et al. (1956) time-average equations. The conclusions state that the Gassmann (1951) fluid-substitution equation can be omitted when fluids other than brine are used in the Raymer et al. (1980) equation. Conversely, changing from brine to a different fluid in the time-average equation requires an intermediate fluid-substitution step to calculate accurate velocity values as a function of porosity. This work appeared in *The Leading Edge* (Spikes and Dvorkin, 2004).

Chapter 3 presents the deterministic reservoir characterization method that provides a basis for the probabilistic work. It shows how a combination of elastic properties (impedance and Poisson's ratio) can be used to predict values of clay content and porosity for a given saturation. This is done at the well-log scale and at the seismic scale by using Backus-averaged elastic-property well curves. Publication of this technique was in *Exploration Geophysics* (Spikes and Dvorkin, 2005).

Chapter 4 introduces a new Bayesian inversion technique to predict probabilistic values of clay content, porosity, and saturation given seismic amplitudes on a trace-by-trace basis. Exhaustive forward modeling of the prior model provides a complete set of earth, elastic, and accompanying seismic models. A full grid search, utilizing an acceptance/rejection criterion, identifies the synthetic traces that match a real trace within a predefined threshold. The modeled reservoir properties corresponding to the matching traces constitute the likelihood function, allowing the calculation of the conditional posterior distribution. A test on well and seismic data from offshore Africa reveals an overprediction of porosity and uncertain predictions of clay content and saturation. Secondary results, however, indicated a tight negative correlation between porosity and thickness. This work appeared in *Geophysics* (Spikes et al., 2007) with contributions from Tapan Mukerji, Jack Dvorkin, and Gary Mavko.

Chapter 5, the most important contribution to this dissertation, extends the inversion technique to include a full parameterization of thickness. Results from applying the method to the same offshore Africa dataset showed how the predicted relationship between porosity and thickness varies by including the less certain clay content and saturation parameters in the inversion. This work demonstrates both the benefits and limitations of the inversion technique. For a given reservoir interval below seismic resolution, this example illustrated the trade-off between porosity and thickness. At the same time, including the reservoir parameters that minimally affect the seismic response in this specific case (clay content and gas saturation) introduces statistical noise that can be mistaken for reservoir heterogeneity. Interestingly, joint inversion of thickness, porosity, and saturation can provide probabilistic conditional estimates of saturation even in stiff reservoir rocks. Tapan Mukerji and Jack Dvorkin provided suggestions and critiques of this work.

Chapter 6 includes two applications of the inversion method to predict thickness, clay content, porosity, and saturation. The first is to use a full stack of the amplitude data, rather than near- and far-angle stacks, from the offshore Africa dataset. Using the full stack produced results very similar to those using the angle stacks. In the second

example, a North Sea dataset included a well with a stack of gas sands. Given the thickness of this package, top, bottom, and internal reflections were present. This tested a different aspect of the inversion; because the reservoir could be resolved, the inversion provided independent estimates of porosity and thickness. Clay content and saturation predictions were still uncertain. Jack Dvorkin and Marie Schneider contributed to this paper during its preparation for publication in *The Leading Edge.*

Chapter 7 is a sensitivity analysis of the inversion on synthetic data. Three user-defined parameters, the cross-correlation window length, the correlation threshold, and the number of accepted synthetic traces were varied systematically and tested as a function of noise in the synthetic seismic data. Results showed that seismic data containing less than 1% noise provided reliable predictions of the rock properties. At or above this noise level, the seismic signatures deviated too much relative to the noise-free synthetic realizations to provide accurate results. Therefore, this analysis indicated that the inversion may falter if noise in the seismic data exceeds this level.

The appendix serves as a guide to potential users and developers to reproduce the workflow. It details with graphics and supporting text the main points of the workflow. Those points include the prior seismic interpretation and rock physics model, the forward problem, the inverse problem, and the analysis of the results.

Chapter 2
Gassmann-consistency of velocity-porosity transforms

"Everything should be made as simple as possible, but not simpler."

--Albert Einstein

2.1 Abstract

Two commonly used empirical rock-physics models, the Wyllie time average and the Raymer-Hunt-Gardner model, include terms to account for lithology, porosity, and fluid. More specifically, the corresponding equations contain an explicit fluid P-wave velocity term. The derivations for both transforms were based on experimental data mostly for brine-saturated consolidated rocks. The purpose of this work is to determine whether these two transforms can be used directly to accurately predict the velocity in rock with hydrocarbon, or instead rigorous fluid substitution from the wet-rock moduli is required for accurate velocity prediction. First, we calculate the bulk and compressional moduli of brine-saturated rock using the two models over wide ranges of total porosity and clay content. Next, we calculate these moduli in gas-saturated rock (a) using theoretical fluid-substitution equations; and (b) directly from the models using the P-wave velocity of gas. We find that for the Raymer-Hunt-Gardner model very little

difference exists between the elastic moduli calculated using these two approaches. However, for the Wyllie time average, the two methods yield substantially different elastic moduli. The conclusion is that the Wyllie time average should not be used to calculate the velocity in rock with gas or light oil. Conversely, the Raymer-Hunt-Gardner model can be used directly to assess the velocity in rock with any type of pore fluid. The latter result is both theoretically and practically significant because (a) an empirical equation appears to implicitly and rigorously account for a theoretically predicted effect of the pore fluid; and (b) a single rock-physics transform can be applied with confidence to reservoirs with a variety of fluid types as long as the model is appropriate for the rocks under examination.

2.2 Introduction

Rock-physics results have shown that the effective elastic moduli, and thus the seismic velocity of rock, depend on the porosity, lithology, and pore fluid. Laboratory experimentation combined with empirical statistical regression has resulted in several porosity-velocity transforms or models for siliciclastic rocks (e.g., Wyllie et al., 1956, 1958; Raymer et al, 1980; Tosaya and Nur, 1982; Kowallis et al., 1984; and Han, 1986). The development of these models led to deterministic interpretation of petrophysical properties, porosity in particular, from seismic velocity data.

Effective moduli and velocity depend not only on porosity, lithology, and pore fluid, but also on geometric variations of minerals and pores, textural positions of minerals, compaction trends, and diagenetic history. Empirical rock-physics transforms do not explicitly consider these latter factors and, thus, do not directly model the intricacies of the actual physical systems. However, these transforms are easy to use, and if they quantitatively explain field data, users favor them over more complex theoretical models. Two such ermpirical models used frequently in the petroleum industry are the Wyllie et al. (1956) time average (WTA) and Raymer-Hunt-Gardner (1980) (RHG) models.

We focus on these two models because each contains an explicit term for the P-wave velocity of the fluid. Both models were derived based on experimental data mostly for brine-saturated consolidated rocks. The question we ask is can these models be used with any fluid to obtain the appropriate corresponding velocity and effective elastic moduli, or is a theoretically rigorous fluid-substitution step (Gassmann, 1951; or Mavko et al., 1995) necessary?

The goal of this work is to determine whether the velocity and effective elastic moduli obtained from these models when using any pore fluid are consistent with the effective moduli obtained when translating from one fluid to another, drastically different pore fluid (such as from brine to gas) through theoretical fluid substitution. To assess that question, we model the effective elastic moduli for a gas-saturated scenario using the two transforms under examination. The modeling of moduli for gas-saturated rock is performed in two ways. The first way is to calculate the moduli using gas as the saturating fluid directly in the transforms. The second way is to use brine as the saturating fluid and then apply brine-to-gas fluid substitution (Gassmann, 1951; and Mavko et al., 1995) to translate the wet-rock elastic moduli into those at 100% gas saturation. The modeled results from the two gas-saturated-rock scenarios are then compared.

In the original publications, Wyllie et al. (1956) and Raymer et al. (1980) stated that the proposed transforms can be used regardless of the nature of the saturating fluid. Here we assess the validity of this statement and the consistency of these empirical transforms with rigorous theoretical fluid substitution.

2.3 Modeling methodology

Both the WTA and RHG models link the P-wave velocity V_p to the total porosity ϕ, the velocity in the solid phase V_{ps}, and the velocity in the fluid V_{pf}:

$$\frac{1}{V_p} = \frac{1-\phi}{V_{ps}} + \frac{\phi}{V_{pf}} \tag{2.1}$$

for WTA and

$$V_p = (1 - \phi)^2 V_{ps} + \phi V_{pf} \tag{2.2}$$

for RHG. The bulk density ρ_b can be calculated from the density of the mineral phase ρ_s and that of the pore fluid ρ_f as

$$\rho_b = (1 - \phi)\rho_s + \phi\rho_f. \tag{2.3}$$

Both original publications provide ranges for V_{ps} in various lithologies. A more universal way to calculate V_{ps} is to mix the elastic moduli and densities of the constituent minerals using the Voigt-Reuss-Hill (1952) average for the moduli and the arithmetic average for the density:

$$
\begin{aligned}
V_{ps} &= \sqrt{(K_s + \frac{4}{3}\mu_s)/\rho_s}; \\
K_s &= \frac{1}{2}\left[(1 - C)K_q + CK_c + \frac{1}{(1 - C)/K_q + C/K_c}\right]; \\
\mu_s &= \frac{1}{2}\left[(1 - C)\mu_q + C\mu_c + \frac{1}{(1 - C)/\mu_q + C/\mu_c}\right]; \\
\rho_s &= (1 - C)\rho_q + C\rho_c,
\end{aligned}
\tag{2.4}
$$

where the equations are given for a quartz/clay mixture; K_s and μ_s are bulk and shear moduli of the solid phase, respectively; ρ_s is the density of the solid phase; C is the volume fraction of clay in the solid phase; and the subscripts "q" and "c" refer to quartz and clay, respectively. The bulk moduli of quartz and clay are 36.6 and 21 GPa, respectively, and their shear moduli are 45 and 7 GPa, respectively. The density of quartz is 2.65 g/cc, and that of clay is 2.58 g/cc.

The velocity and density of the pore fluid can be calculated from the Batzle-Wang (1992) equations. In this example we use a brine with a salinity of 35000 ppm at 75° C and 30 MPa pore pressure. The gas gravity is 0.65. The resulting bulk moduli are 2.73 GPa for brine and 0.07 GPa for gas. The densities are 1.01 g/cc for brine and 0.21 g/cc

for gas. The corresponding velocities are 1.64 km/s in brine and 0.59 km/s in gas.

We examine a model rock where the only two minerals present are quartz and clay. First we calculate the P-wave velocity and density from Equations (2.1) to (2.3) for brine- and gas-saturated rock. We also calculate the compressional modulus $M = \rho_b V_p^2$ as well as the bulk modulus $K = M - (4/3)\mu$, where the shear modulus $\mu = \rho_b V_s^2$. The S-wave velocity V_s is calculated from V_p using the Greenberg-Castagna (1992) model, which, for water-saturated sand-shale sediment, can be approximated by the Castagna et al. (1985) mudrock equation, $V_s = 0.862 V_p - 1.172$, where the velocity is in km/s.

Next, the elastic moduli in rock with brine are used again, but this time to calculate the moduli in rock with gas through fluid substitution. The bulk modulus in rock with gas (K_2) is calculated from that in rock with brine (K_1) using Gassmann's (1951) equation

$$\frac{K_1}{K_s - K_1} - \frac{K_{Brine}}{\phi(K_s - K_{Brine})} = \frac{K_2}{K_s - K_2} - \frac{K_{Gas}}{\phi(K_s - K_{Gas})}, \qquad (2.5)$$

where K_{Brine} and K_{Gas} are the bulk moduli of brine and gas, respectively. The compressional modulus in rock with gas (M_2) is calculated directly from that in rock with brine (M_1) using the Mavko et al. (1995) V_p-only fluid substitution equation:

$$\frac{M_1}{M_s - M_1} - \frac{K_{Brine}}{\phi(M_s - K_{Brine})} = \frac{M_2}{M_s - M_2} - \frac{K_{Gas}}{\phi(M_s - K_{Gas})}, \qquad (2.6)$$

where M_s is the compressional modulus of the mineral phase.

Although any two fluids or fluid mixtures can be used for this study, we choose to use brine and gas because they are significantly different from each other, and as such, they represent the two end members of a large spectrum of natural pore fluids. The high bulk modulus and density of brine and the low bulk modulus and density of gas provide two extrema in the effective elastic moduli. Therefore, we compare effective moduli only for 100% gas-saturated rock.

2.4 Modeling results: Wyllie's time average

The bulk modulus for gas-saturated rock with C between zero and 100% and ϕ up to 40% is plotted versus ϕ and C in Figure 2.1. The upper-surface values are predicted by Gassmann's (1951) fluid substitution applied to the brine-saturated-rock bulk modulus, whereas the lower-surface values are directly predicted by WTA. The difference between the two estimates can be very significant, reaching 15 GPa (about 50% relative error) at low C and low ϕ.
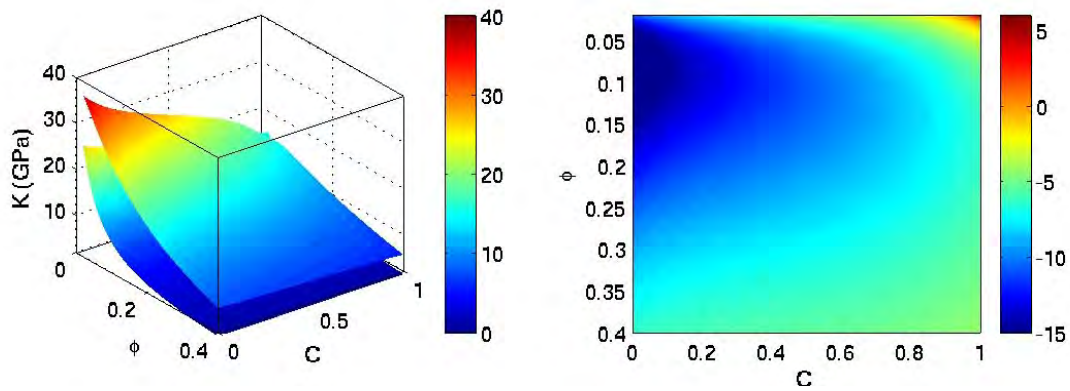
Figure 2.1. Left: Bulk modulus in gas-saturated rock as predicted directly by WTA (lower surface) and using fluid substitution from brine-saturated rock (upper surface). The colorbar represents bulk modulus values Right: The difference between the upper- and lower-surface values, where color represents this value in GPa.

The compressional-modulus values calculated in the same fashion using WTA are shown in Figure 2.2. The difference in this case reaches 25 GPa (about 30% relative error). This largest difference is at low C and low-to-medium ϕ. The difference becomes small only at very large C and small ϕ.
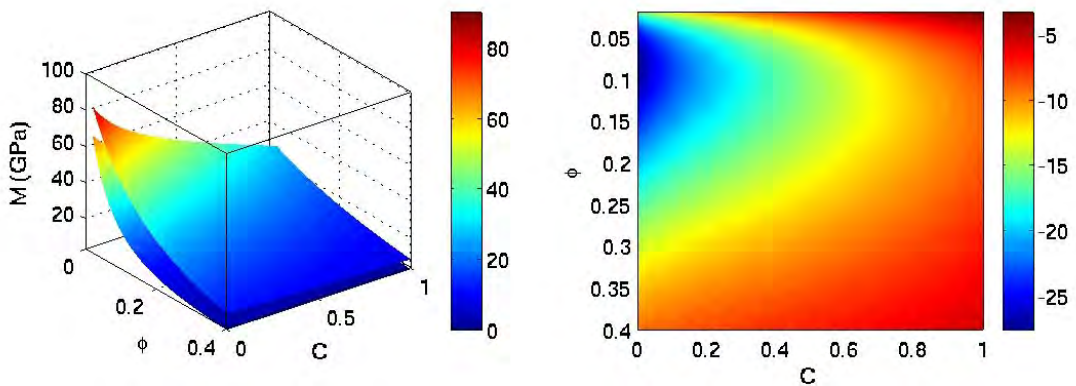
Figure 2.2. Same as Figure 2.1 but for the compressional modulus.

2.5 Modeling results: Raymer, Hunt, and Gardner

The same procedures were used to calculate the elastic moduli in gas-saturated rock using RHG. The modeled values presented in Figures 2.3 and 2.4 indicate that the difference between the two results is very small and can be neglected for all practical purposes. Remarkably, this empirical model appears to be fully consistent with rigorous theoretical fluid-substitution equations.
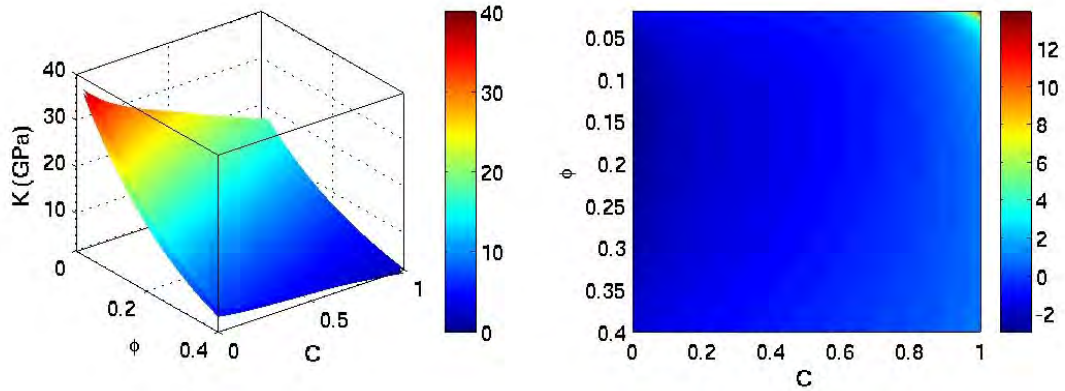
Figure 2.3. Same as Figure 2.1 but for RHG.
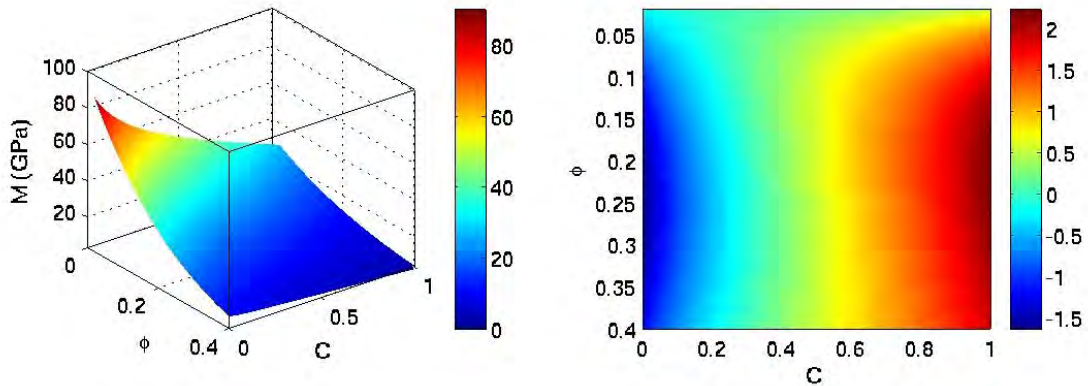
Figure 2.4. Same as Figure 2.2 but for RHG.

2.6 Discussion and conclusions

The K surfaces (Figure 2.1) and M surfaces (Figure 2.2) indicate clearly that if one uses gas directly in the WTA equation, the modeled values are significantly different than those obtained when using fluid-substitution methods to transform the effective moduli from brine-saturated to gas-saturated rock. For either the K or M surfaces, the question remains as to which surface is correct. Due to the heuristic nature of the

equation, neither method of calculating the moduli can be claimed as absolutely correct, nor can one method be called more correct than the other. Because substantially different moduli, and thus velocity values, possibly can be obtained when using WTA with or without fluid substitution, care should be taken when using this model with any fluid. Most likely, fluid substitution should be performed from brine- to gas-saturated conditions because the original model was derived primarily from data from wet rocks.

WTA is used for two primary purposes. The first is to estimate seismic velocities with a given mineralogy and pore fluid, and the second is to estimate porosity from seismic velocity with knowledge of rock type and pore-fluid content. Therefore, this model can be used for both reservoir and non-reservoir rocks. The most significant differences in the calculated moduli occur for C less than 0.2 and ϕ between 5% and 15%. The smallest difference occurs for very high C for all ϕ. Therefore, depending on the lithology, the accuracy of the porosity estimate from seismic velocity may vary substantially, particularly between reservoir and non-reservoir rock.

The most important conclusion is that WTA is not consistent with the fluid-substitution equations.

In contrast to the results of modeling with the WTA, the results of RHG modeling indicate that any pore fluid may be used within this model without using fluid-substitution methods. Calculated K and M values result in only a few GPa difference when using gas directly in the RHG as opposed to using brine-to-gas fluid substitution. This model was derived based mostly on brine-saturated sandstones, and technically it should be used only to estimate seismic velocity in brine-saturated sandstones. However, because of the similarity in the modeled effective elastic moduli, the RHG can be used with any pore fluid.

The most important conclusion is that RHG is consistent with the fluid-substitution equations.

The examples shown here are for two extreme fluid cases, brine and gas, so that differences in the calculated moduli are greater than those between any other two fluids. Therefore, if the fluid of interest is gas, fluid substitution from brine to gas should be

used with WTA to calculate the elastic moduli for gas-saturated rock. Conversely, based on the models shown here, any pore fluid can be used with confidence directly in the RHG model without an intermediate fluid-substitution step.

2.7 Acknowledgments

Chapter 3
Simultaneous model-based inversion for lithology, porosity, and fluid

"In questions of science, the authority of a thousand is

not worth the humble reasoning of a single individual."

--Galileo Galilei

3.1 Abstract

The three main variables that determine the elastic response of sediment within a clastic environment are porosity, mineralogy, and pore fluid. The number of the elastic variables offered by seismic data does not exceed two (e.g., the impedance and Poisson's ratio). Therefore, resolving seismic data for reservoir properties is formally unattainable, even if a perfect elastic rock physics model exists. We solve this problem by utilizing an additional petrophysical link, the one between the clay content and total porosity, which is often observed in a dispersed-shale environment. First, we establish a rock physics model. Next, we identify the reservoir through a combination of impedance and Poisson's ratio. Then, within the reservoir, we invert the P-wave impedance for both the total porosity and clay content by using two relations: (a) the rock physics model that links the P-wave impedance to the total porosity and clay content; and (b) the petrophysical model

that links the clay content to total porosity. The results are accurate when the method is applied directly to well-log data. Most importantly, we obtain accurate reservoir property estimates by using the method with upscaled well-log curves, which demonstrates its relevance to real seismic data.

3.2 Introduction

Recent advances in seismic inversion may help to map elastic properties, such as the P-wave impedance (I_P), Poisson's ratio (ν), and density (ρ), in the subsurface. The ultimate goal, however, is to map the porosity (ϕ), clay content (C), and pore fluid or water saturation (S_w). Such transformation of the elastic properties into reservoir properties requires a rock physics model that links I_P and ν to ϕ, C, and S_w. However, even if a perfect rock physics model is available, we cannot resolve two equations for three unknowns — an underdetermined system. The problem is that no more than two elastic properties can be obtained from seismic data.

This problem can be solved by taking advantage of findings of Thomas and Stieber (1975), Marion (1990), and Yin (1992). These authors showed that in certain depositional environments, ϕ and C are related. This relation can serve as an additional constraint and help complete an underdetermined system of rock-physics equations. As a result, an inversion of I_P and ν for ϕ, C, and S_w becomes possible. Such an inversion procedure is developed in this paper.

An example that we use here comes from a geologically mature fluvial environment where the elastic properties are linked to sediment properties by the rock-physics models of Raymer et al. (1980) and Greenberg and Castagna (1992). We also find that ϕ and C are linked by an approximately linear petrophysical transform that reflects the dispersed-shale depositional mode. In this mode, the reduction of ϕ is due to small shale particles filling the pore space of the sand-grain frame. Rock physics and petrophysics are used together to identify the reservoir and then to resolve I_P from the log data within the reservoir for ϕ and C. As expected, we arrive at the correct ϕ and C values.

Our main task, however, is to show that this method can be used with seismic-impedance inversion data, whose scale is much larger than that of well-log data. To address this issue, we upscale the original elastic-property logs using the Backus (1962) average and then apply the same procedure to calculate the clay content and porosity within the reservoir. The results appear to be accurate.

The approach we take has been utilized by Goldberg and Gurevich (1998) who proposed to invert the P- and S-wave velocity data for the clay content and total porosity. We build upon this approach to explicitly include a textural petrophysical relation in the inversion scheme and also show that it is valid at the seismic scale.

3.3 Original data and upscaling

The well-log data used in this study are from a fluvial environment characterized by a thick shale layer located above oil sand. Beneath the sand are several coarsening-up sand/shale sequences (Figure 3.1). The I_P contrast between the sand and surrounding shale is small. Therefore, no noticeable normal-incidence or small-angle seismic reflections are expected at these interfaces. Compared to the surrounding shale, however, the small-ν interval of the hydrocarbon-filled sand may result in a pronounced AVO effect.

In order to understand how the log-scale features present in these data appear at the seismic scale, we apply the Backus (1962) average to upscale the elastic moduli, and the running arithmetic mean to upscale the bulk density (see also Mavko et al., 1998, for this upscaling method). The upscaling window is approximately 1/4 of the seismic wavelength, about 18.5 m for 50 Hz. The I_P and ν at the seismic scale (Figure 3.1) are calculated from the upscaled moduli and density.

3.4 Methodology

In this inversion method we assume that the two known quantities are I_P and ν, whereas the three unknowns are ϕ, C, and S_w. The main steps are to (1) establish a rock-physics model using well-log data; (2) identify the reservoir through a combination of I_P and ν; (3) find a petrophysical link between ϕ and C; and (4) combine the $I_P - \phi$

and $\phi - C$ equations to calculate ϕ and C from I_P in the reservoir.

3.4.1 Rock-physics model

To select a rock-physics model, we assume that the elastic properties of the sediment depend on the total porosity, mineralogy, and pore fluid. We also assume that the only minerals present in the interval are clay and quartz. Consider the Raymer et al. (1980) model (RHG) that relates the P-wave velocity (V_p) of the rock to ϕ, the mineral-phase velocity (V_{ps}), and the pore-fluid velocity (V_{pf}):

$$V_p = (1 - \phi)^2 V_{ps} + \phi V_{pf} \; , \qquad (3.1)$$

where V_{pf} is calculated from the bulk modulus and density of the pore fluid (Table 1) and V_{ps} is the velocity in the pure-mineral (zero-porosity) phase. For a mixture of clay and quartz, V_{ps} is calculated according to Hill's average (Mavko et al., 1998). The bulk density (ρ_b) is a function of ϕ, the density of the mineral phase (ρ_s), and that of the pore fluid (ρ_f):

$$\rho_b = (1 - \phi)\rho_s + \phi \rho_f . \qquad (3.2)$$

Table 1. Fluid and mineral properties.

	Bulk Modulus (GPa)	Shear Modulus (GPa)	Density (g/cm^3)
Brine	2.721	0	1.024
Oil	0.597	0	0.685
Quartz	36.6	45	2.65
Clay	21	7	2.58

To calculate the S-wave velocity, we use the Greenberg-Castagna (1992) P-to-S-wave velocity transform (GC), which, in water-saturated siliciclastic rocks, is close to the mudrock equation of Castagna et al. (1985):

$$V_s = 0.862 V_p - 1.172 . \qquad (3.3)$$

Equations 3.1 to 3.3 are also used for conditions where $S_w < 1$. I_P and ν are calculated from V_P, V_S, and ρ_b as

$$I_p = \rho_b V_p, \quad \nu = \frac{1}{2} \frac{V_p^2 / V_s^2 - 2}{V_p^2 / V_s^2 - 1} .$$ (3.4)

I_P, ν, V_p, V_s, and ρ_b are, therefore, functions of ϕ, C, and fluid properties.

Out next task is to validate the applicability of the RHG-GC model to the well-log data under examination. For this purpose we use the measured velocity and density as well as the total porosity calculated from the bulk density according to the mass-balance equation:

$$\phi = \frac{2.65 - \rho_b}{2.65 - \rho_w} ,$$ (3.5)

where ρ_w (the density of brine) is given in Table 1. Equation (3.5) assumes that the density of the mineral phase is fixed as 2.65 g/cm^3, and the measured bulk density corresponds to fully brine-saturated conditions resulting from mud-filtrate invasion.

The next task is to calculate C from the well data. Two principal ways are used to determine C from well data. One is from lithology-indicator measurements, such as the gamma-ray (GR) or spontaneous-potential (SP) logs. The simplest approach is to linearly scale GR so that the maximum and minimum clay content in the section correspond to the maximum and minimum GR.

Another approach is model-based and uses the V_p and V_s data. If we know how these two variables depend on ϕ and C, then it is possible to obtain C from the measured V_p, V_s, and ϕ log curves. Various rock-physics models can be used for this purpose, such as the empirical relations by Han et al. (1986) and Tosaya (1982). In this specific case we evaluate the applicability of the RHG model and thus determine C in the entire interval, by requiring that I_P be calculated from Equations (3.1), (3.2), and (3.4), and that the ϕ curve corresponds to the measured I_P.

The resulting *C* curve is plotted in Figure 3.1, in red. Compare this *C* to the curve obtained from linear scaling of *GR* where we assume that the clay content is 0.07 in "pure sand" (i.e., at the minimum *GR*) and 0.93 in "pure shale" (i.e., at the maximum *GR*). The resulting curve is plotted in black in Figure 3.1. The model-based *C* is reasonably close to the *GR*-based *C*, and the RHG-GC-based *C* is used below throughout the paper.
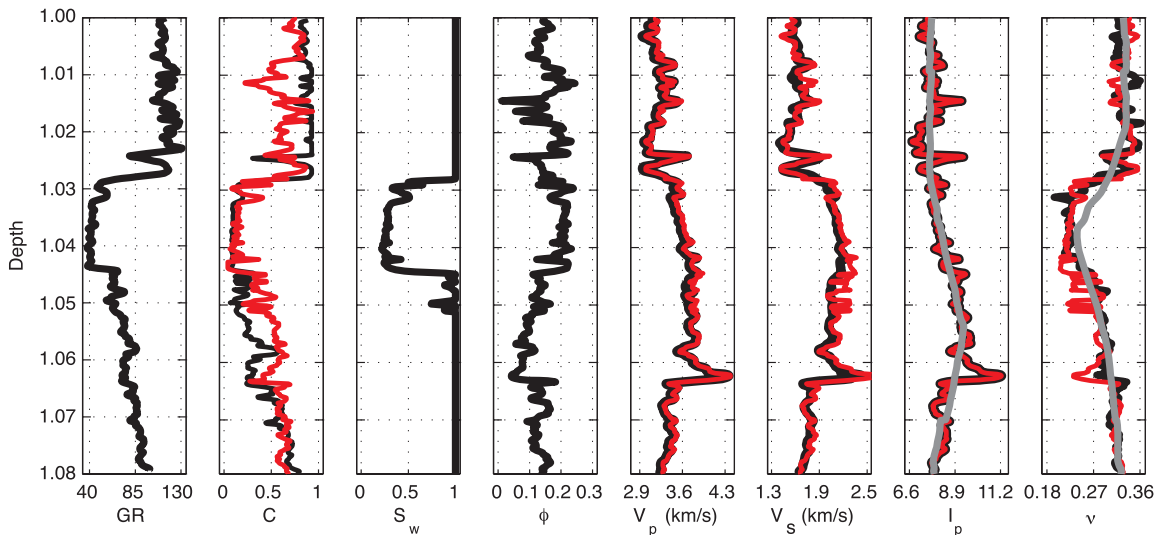
Figure 3.1. Well-log curves used in this study. From left to right: gamma ray, clay content, water saturation, total porosity, P-wave velocity, S-wave velocity, P-wave impedance, and Poisson's ratio. The depth is fictitious. In the clay-content frame, the black curve comes from linearly scaling the gamma-ray curve, whereas the red curve is calculated as to match the Raymer et al. (1980) model predictions. In the last four frames, the black curves are for the original log data while the red curves are calculated from porosity and clay content using the Raymer et al. (1980) and Greenberg and Castagna (1992) models, using the measured saturation log. The gray curves (frames seven and eight) are for the upscaled values.

The RHG-GC model curves for I_P and ν calculated for different *C* and 100% brine saturation accurately match the data in Figure 3.2, which further illustrates the utility of the model selected here.
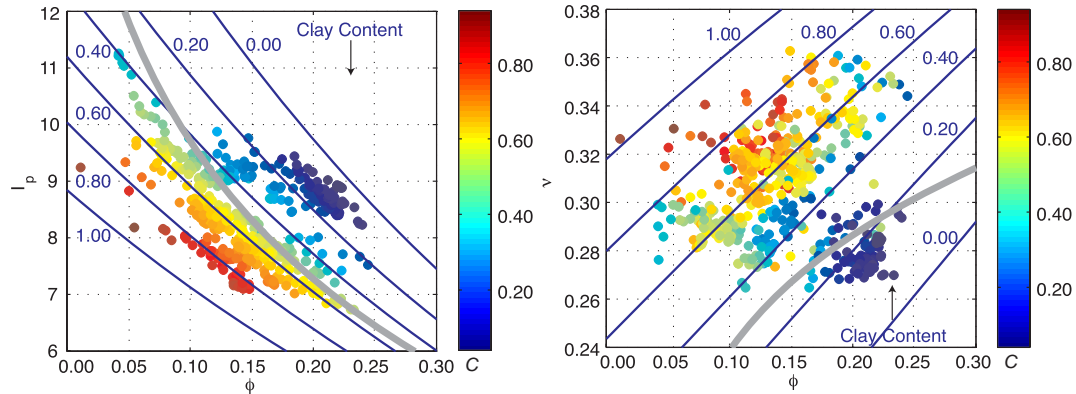
Figure 3.2. P-wave impedance (left) and Poisson's ratio (right) versus the total porosity. The elastic properties are calculated for 100% water saturation. The data are color-coded by the clay content. The blue curves are from the RHG-GC model, each drawn for a fixed clay content starting at 0.0 and ending at 1.0 with 0.2 step (clay content is shown on the curves). The bold gray curves are from the uncemented sand/shale model drawn for zero clay content. This curve is drawn to show that the Raymer et al. (1980) model is appropriate.

The most important result of this model-to-data-matching exercise is the consistency between the selected rock-physics model and the data under examination. Let us emphasize that our selection of the model is not random. It is instructive to mention that RHG was derived from empirical data for brine-saturated consolidated sediments. The fact that this model matches the data is consistent with the geological nature of the interval, which is located within a relatively geologically mature and consolidated sand/shale sequence. This fact makes the model predictive beyond the data set used for matching. To emphasize the importance of choosing a geologically consistent rock-physics model, we also compute model curves for pure-quartz sand using the soft sand/shale model of Dvorkin and Nur (1996). These curves (plotted gray in Figure 3.2) significantly underestimate I_P and overestimate ν in the sand.

RHG-GC is robust, yet one of the simplest transforms between porosity, lithology, and fluid and the elastic-wave velocity. The RHG-GC equations were derived from large sets of well-log and core data, which provides assurance that these transforms are predictive and can be applied outside of the original datasets to rock whose geological history is analogous. We have further confirmed the generality of RHG-GC equations by finding that the curves produced using these equations for quartz/clay mixtures are very

close to those produced by the modified upper Hashin-Shtrikman bound (similar to the modified lower Hashin-Shtrikman bound of Dvorkin and Nur, 1996, although not shown here). We choose to use RHG-GC here instead of a more mathematically involved rock-physics model simply because these equations are simpler and are easier to use in inversion.

Other simple empirical equations appropriate to use for mature sediment, such as those of Wyllie et al. (1956) and Krief (1990), are available in the literature and possibly could be tested here. However, because RHG-GC accurately describes and explains the data, we elect to use it in our inversion procedure.

It is apparent in Figure 3.2 that both ϕ and C strongly affect I_P. At a constant C, a small ϕ corresponds to a large I_P, whereas at a fixed ϕ, a large C corresponds to a small I_P. This dependence of V_p and I_P on both ϕ and C was documented implicitly by Wyllie et al. as early as 1956. Raymer et al. (1980) further confirmed such dependence in 1980. Laboratory experiments verified this effect in clean and shaley sandstone (Han et al., 1986) and shale samples (Tosaya, 1982).

Let us point out once again that in Figure 3.2, right, we present ν calculated at full water saturation, which serves the purpose of understanding the dependence of ν on porosity and lithology. The dependence of ν on ϕ is pronounced in shaley sand and shale. It is apparent that this dependence is also strongly linked to lithology because ϕ and lithology (as manifested by the clay content) vary together. The strong lithology dependence of ν is also manifested by the fact that its range in the shale is approximately from 0.30 to 0.35, whereas the ν range in water-saturated sand is from 0.27 to 0.29.

3.4.2 Reservoir delineation

Figure 3.3 (left) shows the $I_P - \nu$ plane, where we map three domains using RHG-GC: brine-saturated shale with ϕ from 0.05 to 0.25 and C from 0.20 to 0.95; sand with 60% oil saturation, ϕ from 0.15 to 0.25 and C from 0.0 to 0.2; and the same sand with 80% oil saturation. The two sand domains overlap one another, which means that the model domains are not very sensitive to variations in fluid saturation. The well data

displayed in the same figure fall within these model-based domains. The pay-sand domains and shale domain do not overlap, which means, in principle, that the oil sand can be identified from seismic data by using a combination of I_P and v. To make this identification, we draw a cut-off line just below the shale domain. The corresponding equation is

$$I_p = 18.6 - 39.2\,v \ . \tag{3.6}$$

If $I_p < 18.6 - 39.2\,v$, then the domain is oil-saturated sand. If $I_p \geq 18.6 - 39.2\,v$, then the rock is water-saturated shale. This cut-off criterion is apparently valid with the log data. Will it be valid at the seismic scale? To address this question, we cross-plot the upscaled I_P and v (Figure 3.3, right). We find that although the upscaled pay-sand data shift toward higher v, the above cut-off criterion is still valid for reservoir delineation.
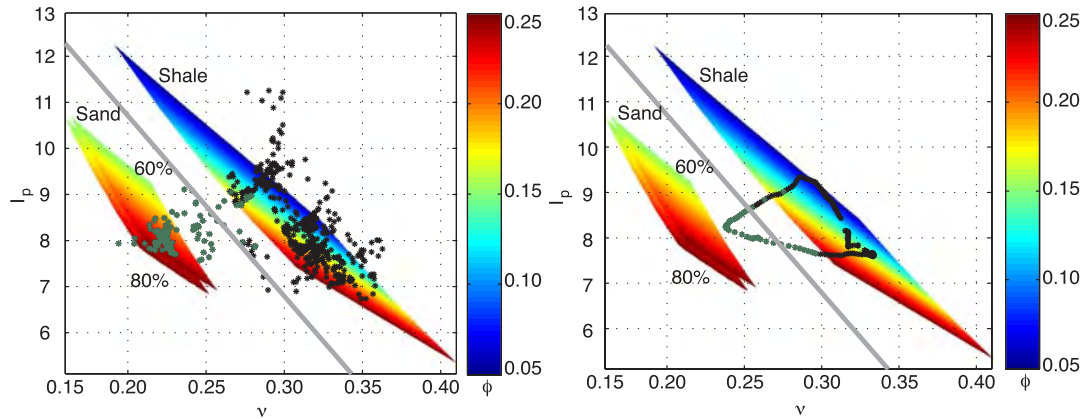
Figure 3.3. The P-wave impedance versus Poisson's ratio with sand and shale domains mapped according to the RHG-GC model. The color code is the total porosity. In the two sand domains, the oil saturation is 60% and 80%. The joint fluid- and lithology-discrimination cut-off line is shown in bold gray. The data points are shown for the log scale (left) and for the seismic scale (right). The pay-sand data points with water saturation below 50% are highlighted in both plots in green.

3.4.3 Relation between porosity and clay content

Let us assume now that pay sand can be detected from seismic data using a combination of seismically derived I_P and v, and concern ourselves with quantifying ϕ and C in the sand. Because the RHG equation requires both ϕ and C to calculate I_P, an

additional relation is required to derive ϕ and C from I_P. Such a relation may be a link between ϕ and C, which is not uncommon in shaley sands (Thomas and Stieber, 1975).

Figure 3.4 is a cross-plot of ϕ versus C. Arguably, a relationship exists between ϕ and C in the sand. In clean sand, ϕ is relatively large, but decreases as C is added to the rock. The turning point in this trend is at $C \approx 0.4$. At larger C the total ϕ tends to increase. This V-shaped pattern is characteristic of bimodal sand/clay mixtures (Marion, 1990; Yin, 1992) where the transition from sand to shale occurs by the small shale grains filling the pore space between the large sand grains that form the frame. This mode of deposition can be called the dispersed shale pattern and is common in a fluvial environment. Dvorkin and Gutierrez (2002) use two linear equations to describe this type of relation between C and ϕ. We follow that example and find two equations relevant to these data:

$$\begin{aligned} C < 0.40 &\;\Rightarrow\; \phi = 0.219 - 0.247C \quad, \\ C \geq 0.40 &\;\Rightarrow\; \phi = -0.130 + 0.400C \; . \end{aligned} \tag{3.7}$$
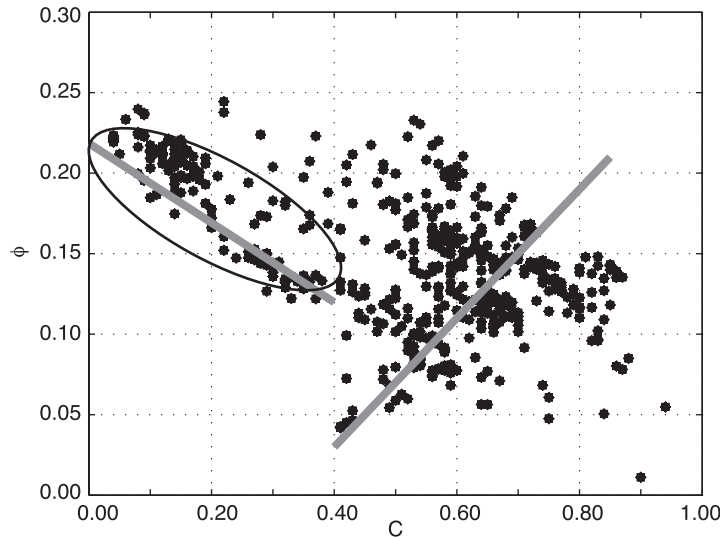
Figure 3.4. Porosity as a function of clay content. Gray lines are according to equation (3.7). The data in the reservoir and below are encircled.

These equations are plotted as gray lines in Figure 3.4. Clearly, this choice of linear $\phi - C$ trends is somewhat arbitrary, especially in the shale part of the plot. However, the only important part of this selection is in the reservoir sand, where the trend is clearly pronounced. We have tested a range of linear equations, similar to the first equation (3.7), to cover the spread of the data in Figure 3.4. The final results show only a weak dependence on this selection as long as the line complies with the trend present in the encircled data in Figure 3.4.

By using only two linear equations to describe the relation between C and ϕ, we effectively ignore the multiple coarsening-up sequences present in the interval. We describe the data by only two statistical trends, which does not account for all the data variability present in the cross-plot in Figure 3.4. At the log scale, these trends may be significant. However, as we show below, at the seismic scale, these trends are assumed to be too small to contribute significant error. The first linear trend in equations (3.7) can now be used together with the RHG equation to resolve I_P in terms of ϕ and C within the reservoir.

3.4.4 Inversion

The inversion procedure consists of five steps:

(1) Invert pre-stack or partial stack seismic data to obtain I_P and ν

(2) find a rock-physics model that relates ϕ to I_P, in this case RHG;

(3) delineate the reservoir by using equation (3.6);

(4) establish the ϕ - C link as in equation (3.7);

(5) use RHG and the ϕ - C link to resolve I_P in the reservoir for ϕ and C.

During this procedure we still have to assign a value to the water saturation (S_w) in the pay, which is needed to calculate the velocity in the pore-fluid phase (V_{pf}) in equation (3.1). For high-compressibility hydrocarbons, such as oil in this reservoir, and within a commercial saturation range, V_{pf} is not very sensitive to water saturation. Therefore, it is expected (as confirmed below) that the inversion for C and ϕ in a reservoir does not strongly depend on the assumed S_w even though ρ and I_P depend linearly on S_w.

3.5 Inversion results

3.5.1 Well-log scale

The inversion results using the originally sampled log-scale I_P and v accurately match the measurement in the reservoir (Figure 3.5). We conducted the inversion while varying S_w between 0.2 and 0.4 and discovered that the resulting C and ϕ are essentially insensitive to S_w variation. This conclusion is positive in the sense that the inverted C and ϕ are reasonably tolerant to the uncertainty in S_w, but it is negative in the sense that the volume of oil cannot be accurately estimated from the elastic properties.
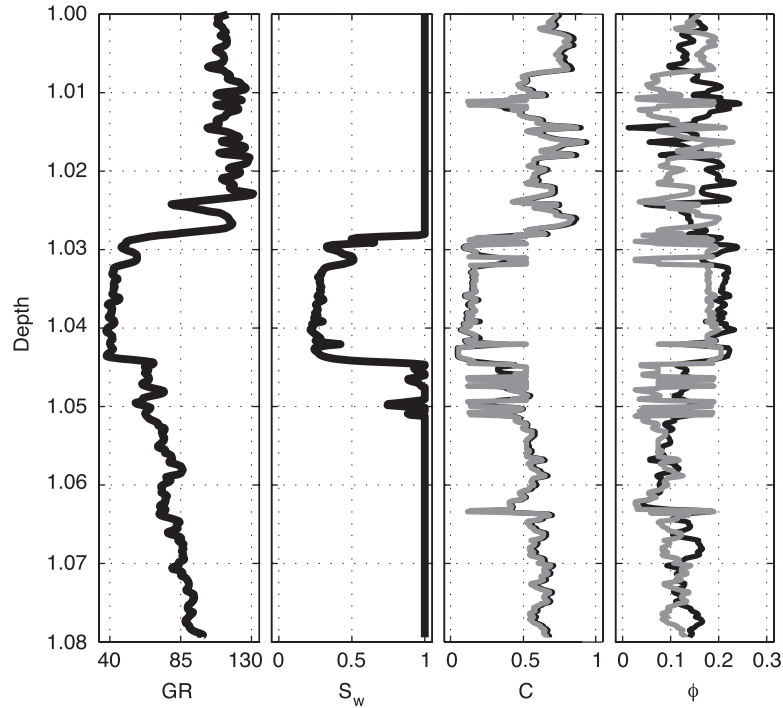
Figure 3.5. The original log-based clay content and total porosity and the predicted clay content and total porosity at the log scale. From left to right: (1) Gamma ray; (2) Water saturation; (3) The RGH-GC-based (black) and predicted (gray) clay content; and (4) The original (black) and predicted (gray) total porosity.

3.5.2 Seismic scale

We test the applicability of the proposed method at the seismic scale by using as inputs the Backus-upscaled I_P and v, which we consider as proxies for the elastic

properties estimated from seismic data. This procedure uses exactly the same equations as used in the log-scale inversion.

First, equation (3.6) allows us to delineate the reservoir at the seismic scale (Figure 3.6, second frame). Next, C and ϕ from this inversion appear to be close to the log-scale values as well as to the arithmetically upscaled C and ϕ curves (Figure 3.6, third and fourth frames). In the reservoir, C is slightly overestimated whereas ϕ is simultaneously underestimated. This is likely to be a result of using a deterministic, single-function C-to-ϕ transform as expressed by equation (3.7). The difference between the porosity predicted at the seismic scale and the measured porosity in the pay zone is ±0.03 porosity units, which amounts to ±14% relative error. We deem this error acceptable given that detecting this difference in seismic data is unlikely. The results presented in this section assure that the proposed inversion methodology is applicable at the seismic scale.
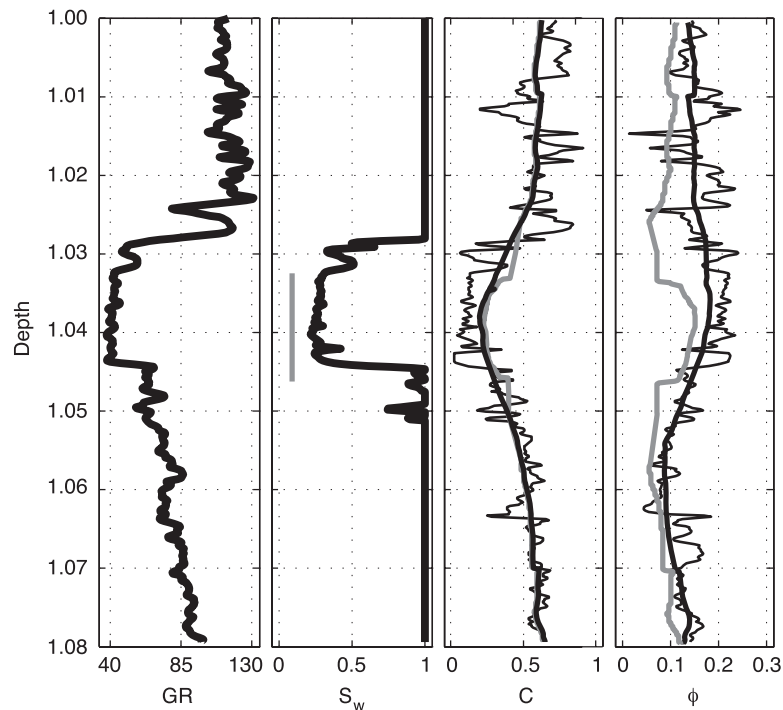
Figure 3.6. The measured clay content and total porosity and the predicted clay content and total porosity at the seismic scale. From left to right: (1) Gamma ray; (2) Water saturation; (3) The log-scale (thin black), arithmetically upscaled (bold black) and predicted (gray) clay content; and (4) The log-scale (thin black), arithmetically upscaled (bold black) and predicted (gray) total porosity. The vertical extent of the reservoir is indicated by the gray line in frame 2.

3.6 Discussion

Obtaining the porosity and mineralogy of reservoir sand from the elastic rock properties is relevant to several applications: (a) reconstructing missing log curves, such as the bulk density, from sonic and dipole data; (b) estimating formation properties from VSP data; (c) mapping formation properties from cross-well velocity data; and (d) mapping formation properties from seismic-impedance inversion data. In all these applications, the formation properties can be estimated correctly only if the relevant, site-specific petrophysical and rock-physics transforms are selected. We show how to select and calibrate a rock-physics model and petrophysical model based on well-log data and also how to establish whether this model can be used at the seismic scale.

The errors in the formation property estimates according to the methodology presented here may come from several sources. Among these are: (a) uncertainty in mineralogical composition; (b) uncertainty in the elastic moduli of the pure minerals, such as quartz and clay; (c) uncertainty in water saturation; (d) uncertainty in the link between porosity and clay content; and (e) uncertainty in the model itself. All these uncertainties can be handled within the selected rock-physics model by assigning a range to an input parameter and then calculating the output range according to the model.

The pay zone delineated at the seismic scale is slightly smaller than the actual pay zone (the second frame of Figure 3.6). The reason is that the upscaled Poisson's ratio curve has larger low-end values when compared to the original log-scale curve (Figure 3.3). Therefore, fewer data points in the $I_P - \nu$ domain satisfy the criterion. This artifact of seismic upscaling is likely to be present in real seismic data, and the interpreter must be aware of its existence. A different cut-off line based on the upscaled values could be implemented for seismic data, as long as it could be verified within the workflow.

3.7 Conclusions

The main intention of this work is to emphasize the importance of using deterministic rock-physics and petrophysical models for reservoir characterization from elastic data obtained at various scales. Such a model-based methodology enables us to (a) perturb the

geological inputs and consistently derive the sensitivity of seismic signatures to these inputs, and (b) understand sometimes complicated relationships present in the data, such as shown in Figures 3.2 and 3.4.

We show that once the underlying rock physics and petrophysics are understood and quantitatively described, it is possible to use them to derive the desired reservoir properties from the elastic input. Such inversion appears to be plausible at the log scale as well as the seismic scale. By no means are the equations used in this work universally applicable in every depositional environment. They are specific to the fluvial system examined. This rock-physics and petrophysics workflow should be considered only as an example.

3.8 ACKNOWLEDGEMENTS

Chapter 4
Probabilistic seismic inversion based on rock-physics models

"When you see something that is technically sweet, you go ahead and do it and you argue about what to do about it only after you have had your technical success. That is the way it was with the atomic bomb."

--J. Robert Oppenheimer

4.1 Abstract

A site-specific rock-physics transform between porosity, mineralogy, fluid, and the elastic-wave velocity is used to invert seismic amplitude data for clay content, total porosity, and saturation. The implementation is Bayesian and yields probabilistic values of the reservoir properties, given seismic measurements and well data. This method focuses on an exploration setting where minimal data exist. Two key assumptions reduce the problem and keep the prior assumptions as non-influential as possible. First, a prior interpretation of the seismic data is required that provides a geobody on which to perform the inversion. Second, the reservoir thickness is assumed to be constant, as are the rock properties within the reservoir. The prior distributions of the reservoir properties are uncorrelated and independent of each other, although this not an essential assumption.

Central to the inversion is the generation of a complete set of *a priori* earth models. A site-specific rock-physics model translates these properties (clay content, porosity, and saturation) into the elastic domain. A complete set of forward seismic models accompanies the earth models, and these seismic models are compared to the real data on a trace-by-trace basis. The reservoir properties corresponding to the seismic models that match the real data within predefined error bars are used to construct the full posterior distribution. This method was tested on well and seismic data from offshore western South Africa. Initial results at a calibration and test well indicate an over-prediction of porosity and uncertain predictions of clay content and saturation. This is a result of the constant-thickness assumption. However, a strong negative correlation between porosity and thickness is predicted, making this method useful.

4.2 Introduction

Quantitative interpretation of geophysical data for hydrocarbon reservoir characterization is a nonunique problem. A solution is to cast the inversion of seismic reflection data for rock properties in terms of probabilities (Tarantola, 1987). The philosophy adopted here is to combine a probabilistic approach with site-specific rock-physics relations between the rock properties and the elastic properties. In other words, uncertainty is draped on a deterministic model.

The approach taken here is empirical Bayesian, in which the goal is to obtain posterior distributions of reservoir properties from seismic measurements. Specifically, the joint conditional probability distribution function is estimated for clay content C, total porosity ϕ, and water saturation S_w from measured seismic responses and well-log information. This distribution is proportional to the product of prior distributions of these properties and a likelihood function. The prior distribution can be written as a product of prior marginal distributions, assuming independence between the variables.

Development of this method was based on exploration seismic data with limited well information, from which only the reservoir properties and their configurations are known at a single well. Defining the prior distributions as uniform distributions of independent

and uncorrelated reservoir properties insures the use of least-committal prior models (sometimes termed non-informative or "vague" priors). Assuming independent prior variables is not an essential assumption for the method. If existing data indicate any correlation, that correlation can be incorporated easily in the prior distribution. Results of interest are posterior joint and marginal distributions of the reservoir properties, which are subsequently calculated from the posterior conditional distribution. The most-likely values from the full joint distribution are selected and then mapped onto seismically identified geobodies. A geobody is defined as a geologic feature obtained from a prior interpretation of seismic data. The parameterization of the method in this chapter is for clastic environments; however, the method can be used in other environments, including carbonate reservoirs, if an appropriate rock-physics model is used.

The first of two main assumptions made in this inversion is that a prior interpretation must provide a geobody on which to perform the inversion. The second assumption is that reservoir thickness is constant at all locations. This assumption may limit the applicability of the inversion. To examine the effect of thickness variation in the inversion results, sensitivity analyses were performed, which indicate that a porosity-thickness relationship controls the seismic response. Full parameterization of incremental thickness modeling (i.e., Neff, 1990, 1993; Gastaldi et al., 1998) is included in the following chapters.

A critical component of the inversion is a complete set of earth models with synthetic seismic data for each model. Each earth model is effectively a three-layer model (overburden, reservoir, underlying shale), but the overburden and underlying shale are multilayered and heterogeneous. All of the earth models contain the same overburden and underlying shale. All properties for these two units are from calibration-well data. The reservoir layer is populated with all combinations of reservoir properties as defined by the prior distribution; this constitutes a regularized grid sampling of the reservoir properties within the reservoir unit. A site-specific rock-physics model translates the rock properties in the reservoir into elastic properties. Last, synthetic seismic data are calculated for each earth model.

Many examples exist of Bayesian inversion applied to geophysics problems. Recent studies have implemented Bayesian inversion to estimate distributions of elastic properties or reservoir properties. One example of estimating distributions of elastic properties is Buland and Omre (2003), who present a linearized AVO inversion to obtain distributions of elastic properties. A second example is by Riedel et al. (2003), who use Bayesian methods for AVO inversion to estimate viscoelastic parameters and associated uncertainties.

Loures and Moraes (2006) provide an example of estimating distributions of reservoir properties to obtain distributions of porosity and clay content from multiple data sets and rock-physics models. Joint estimates of porosity and saturation have been performed using stochastic rock-physics modeling (Bachrach, 2006) and Bayesian statistics (Sengupta and Bachrach, 2007). Gallop (2006) defines lithofacies probabilities from mixtures of Gaussian distributions. Larsen et al. (2006) predict lithology and fluid from prestack seismic data in a Bayesian framework as an extension of the AVO inversion of Buland and Omre (2003).

A study similar to ours is that of Bosch (2004), who solves an optimization problem to jointly estimate elastic properties and lithology, combined with a rock-physics model to obtain porosity. Another similar study is that of Gunning and Glinsky (2004), who use Bayesian inversion in a layer-based technique to obtain distributions of reservoir properties. They include Gaussian prior distributions to describe all of the model parameters and then implement Markov-chain Monte-Carlo sampling of the posterior distributions. Chen et al. (2007) offer a layer-based Bayesian approach combining amplitude-variation-with-angle (AVA) seismic data and controlled-source electromagnetic data to obtain estimates of gas saturation.

This study differs from previous work in that it relies on a prior interpretation to obtain a seismically identified geobody that defines a potential reservoir unit. Within that potential reservoir unit, a regularized grid sampling of the rock-model parameters is performed. The posterior distributions of best-fitting models are obtained through acceptance or rejection in a full-grid search. Note that while some of the works

mentioned above operate on an entire data volume, the parameterization here reduces the dimensionality of the problem and allows the posterior distribution to be computed from the Bayesian formula.

The requirement for a previous seismic interpretation on which to perform the inversion reduces the problem, which allows the posterior distribution to be computed. This requirement could limit the applicability of the inversion method. However, a suitable interpretation can usually be obtained from conventional methods. For exploration seismic data, stratigraphic or structural interpretation is standard procedure. Similarly, AVO analysis or seismic-attribute analysis could provide horizons or surfaces on which to apply the inversion. In addition, more advanced geostatistical techniques (e.g., Bosch et al., 2005; González, 2006) could provide the needed interpretation.

Regardless of the method of interpretation, it will always include some associated uncertainty. There are at least three ways in which this uncertainty could be quantified and included in the inversion. The first is to include a metric of the phase of the seismic data in an envelope around the reservoir. A benchmark could be set based on the trace at the well location. If the data were processed to zero phase, then the metric would be the deviation of zero phase along the horizon of interest. Uncertainty would be lower for a window that was closer to zero phase. Second, without using a well, a single seismic attribute could be used to map the horizon of interest. Then, the parameters of the search algorithm could be varied and the attribute could be used again to map the horizon. Superposition of the multiple interpretations would provide the estimate of uncertainty. Third, multiple independent attributes could be used to map the horizon. Uncertainty would again be quantified through superposition of the multiple interpretations.

For all three cases, a spatial probability would be obtained that could be combined with the posterior distributions obtained from the inversion method presented here. The two geostatistical techniques mentioned (Bosch et al., 2005; González, 2006) inherently provide ways to quantify this uncertainty.

4.3 Bayesian formulation

The Bayesian formulation states that the posterior conditional distribution is proportional to the product of the prior distributions and the likelihood function (e.g. Carlin and Louis, 2000). In the case here, the posterior distribution is the conditional probability of modeled reservoir parameters $m = [C, \phi, S_w]$ given the data $d = [A_N, A_F]$:

$$P(C, \phi, S_w \mid A_N, A_F) = \frac{P(C, \phi, S_w) P(A_N, A_F \mid C, \phi, S_w)}{P(A_N, A_F)} \tag{4.1}$$

where

$$P(A_N, A_F) = \iiint P(C, \phi, S_w) P(A_N, A_F \mid C, \phi, S_w) dC d\phi dS_w \tag{4.2}$$

The data are the observed seismic amplitudes from a near-angle A_N and a far-angle stacked trace A_F. Within this formulation, the posterior conditional distribution and any marginalized posterior distributions are distributions of continuous variables.

4.3.1 Prior distributions

As in any Bayesian formulation of a problem, the *a priori* assumptions are very important. Although formal rules exist for selecting prior distributions (see Kass and Wasserman, 1996), priors can be based on preconceived knowledge, which is assumed to be minimal. Accordingly, the assumptions are made to be as non-committal as possible. Non-informative priors (Carlin and Louis, 2000) are chosen, in this case uniform distributions, to represent C, ϕ, and S_w. Furthermore, the prior distributions are assumed to be independent and uncorrelated, which allows the following assumption:

$$P(C, \phi, S_w) = P(C) P(\phi) P(S_w). \tag{4.3}$$

In this method, band-limited seismic data are used to predict broadband reservoir properties. The band-limited nature of the seismic data is reconciled by using the statistical formulation to obtain the reservoir properties. In addition, the independent treatment of the reservoir properties may not be valid. However, away from the well the

correlation structure is unknown. In an exploration setting, this correlation will remain unknown. If the geologic environment is known, then a correlation structure could be included. If this method were applied in a production setting, then any correlation observed between reservoir properties in multiple wells certainly should be included. Development of this method focused on an exploration setting, so independent priors were chosen. Therefore, if any correlation structure does exist away form the well, the inversion of the data should identify and capture that correlation.

Even though these distributions are selected to be as non-informative as possible, they are limited by physically realizable situations, not by computational demands or challenges of high dimensionality (Malinverno and Parker, 2006; Scales and Tenorio, 2001). For example, because this inversion is performed on a seismically identified geobody, the seismic reflection occurs because of impedance contrast between shale and underlying sand. If C within the reservoir becomes too large, the impedance contrast changes, and then the waveform of the modeled reflection will be substantially different than the measured waveform. This provides a straightforward physical limitation to the C prior distribution. Similarly, rarely is $S_w < 20\%$, in reservoir rock, which is a physically based and observational lower bound for this reservoir. Other sources of prior information include the rock-physics model, the parameters in that model, the reservoir-unit thickness, and the elastic values of the overlying and underlying shales. This additional prior knowledge further constrains the problem, although it is not explicitly included in the prior probability functions. Finally, some combinations of the reservoir properties may result in unrealistic seismic traces. However, the algorithm is designed to reject those traces, along with the unrealistic combinations of reservoir properties.

4.3.2 Likelihood function

Evaluating the likelihood function, $P(A_N, A_F \mid C, \phi, S_w)$, requires two steps: forward modeling and data comparison. Forward modeling consists of regularized grid sampling of the modeled parameters. Computational power allows for this type of simulation to be used within a likelihood function (Carlin and Louis, 2000). To perform this exhaustive

simulation, each combination of reservoir properties is input into an appropriate rock-physics model; the model translates each combination into elastic properties within the reservoir unit. Using elastic-property values from the overlying and underlying shales, synthetic seismic data are calculated using a ray-tracing algorithm where the wavelet was derived from the seismic data. The shale elastic properties used in the forward modeling are those in the calibration well; only the properties within the reservoir unit. The fixed thickness of the reservoir unit is below seismic resolution. The forward-modeling operation to generate the complete set of earth and seismic models is performed one time.

The second part of the likelihood function involves a full grid search, comparing all synthetic traces to each real seismic trace. The goal is to accept a user-defined minimum number of matching traces while maximizing the correlation between the matching synthetic traces and the real trace. Windows from all synthetic traces are cross-correlated with a window from each applicable real trace, where "applicable" indicates that a geobody exists at that trace. Cross-correlation is used in the search algorithm to obtain the proper polarity of the seismic traces. The window length, found experimentally, is approximately one wavelength, with the center of the window corresponding to the mapped time of the geobody for each relevant trace. Because the seismic data have a vertical resolution of approximately one-fourth of a wavelength, a window length of one wavelength was chosen to allow the full waveform around the reservoir to be included in the real and synthetic traces. This is important because the waveform in some modeled traces may be substantially longer than the waveform in the real data, particularly in the far-offset synthetic traces.

After all cross correlations are computed for both the near- and far-angle traces at a given location, the global maximum near-angle and far-angle cross-correlation coefficients are found. Then the acceptance/rejection criterion is defined to find a specific proportion of the total forward-modeled traces that have a local maximum (both near- and far-angle) correlation coefficient that is a specified fraction of the global maximum cross-correlation coefficient. If both near- and far-angle synthetic traces have local maxima greater than or equal to the specified fraction (correlation threshold) of the global

maximum, those synthetic traces are accepted. All others are rejected. If less than the specified proportion is accepted, the correlation threshold is iteratively decreased until the proportion is accepted. Conversely, if more than the specified proportion is accepted, the correlation threshold is increased iteratively until the desired proportion is accepted. This acceptance/rejection step produces a pool of realizations representing samples from the best-fitting part of the complete posterior distribution. If the global maximum correlation is too small, then all traces fall below the threshold and none are accepted.

Each accepted synthetic near- and far-angle trace combination corresponds to a particular earth model. However, there is still ambiguity in the seismic response, because different combinations of the rock properties may result in single values of the elastic properties. The likelihood function determines which seismic signatures are the most likely to occur, along with the corresponding rock properties. By using a full grid search, no uncertainty from sampling the prior remains. The remaining uncertainty in the likelihood function comes from the rock-physics model, the seismic modeling, the real seismic data, and fixed parameters such as thickness and shale elastic properties.

The probability of the seismic data (equation 4.2) also can be estimated after the likelihood function is calculated. This probability can be expressed as a combination of observed and theoretical (A_N^{th}, A_F^{th}) seismic amplitudes:

$$P(A_N, A_F) = P(A_N, A_F \mid A_N^{th}, A_F^{th}) P(A_N^{th}, A_F^{th} \mid C, \phi, S_w). \tag{4.4}$$

Calculating this probability requires an assumption that the misfit between the observed and theoretical seismic amplitudes is Gaussian. Both amplitude values are obtained by calculating the L_2-norm amplitude over the cross-correlation window. This amplitude is chosen to be consistent with the Gaussian assumption. These probabilities are then defined as functions of s, r, and the real data traces:

$$P(A_N, A_F) = \frac{1}{2\pi \det(B^{-1})} e^{-[r-s]^T B^{-1} [r-s]}. \tag{4.5}$$

The matrix B is the covariance matrix of the real near- and far-data traces, r is the two-element vector of real near and far L_2-norm amplitudes, and s is the two-element vector of L_2-norm amplitudes of matching synthetic traces. This joint probability of seismic amplitudes attempts to account for imperfect data, as well as correlation between the near- and far-angle responses and natural variation corresponding to the prior model.

4.3.3 Posterior distributions

Once the posterior distribution (equation 4.1) has been calculated, it can be used to calculate other distributions. Marginalization of equation 4.1 is achieved by integrating the conditional posterior distribution over the other model variables:

$$P_{post}(m_i \mid A_N, A_F) = \int_{m_{-i}} P(m \mid A_N, A_F) dm_{-i} \qquad (4.6)$$

Here, m_i represents any of the three reservoir properties, and m_{-i} is m with element m_i excluded.

4.4 Data application

The method was applied as a probabilistic reservoir characterization tool using a single well and angle-stack seismic data from the Ibhubesi field offshore western South Africa. Two angle stacks were used jointly as the seismic input, with angle ranges of $0°$–$10°$ for the near stack and $11°$–$20°$ for the far stack (Figures 4.1a and b). The geobodies, constructed using attribute analysis to map potential gas sands, indicate traces on which the inversion was performed (Figure 4.1c).
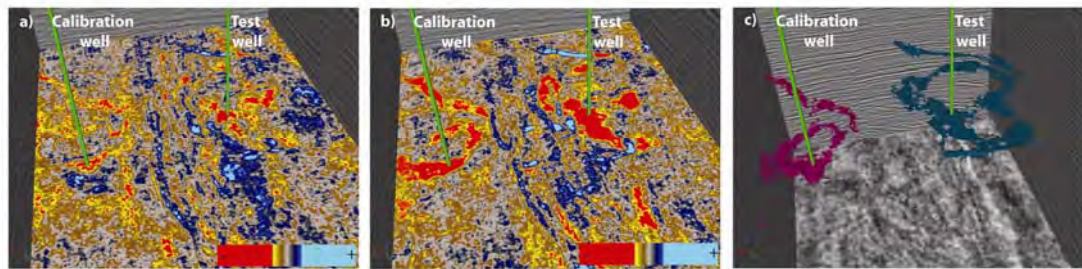
Figure 4.1. a) Near-angle and b) far-angle stacked volumes, showing the class III AVO reflections that delineate the reservoirs in red, and c) reflections mapped as geobodies in magenta and blue. The color scales for a) and b) indicate amplitude of the seismic data. Locations of the calibration and test wells are also shown.

Data from the calibration well are displayed in Figure 4.2. The rock-physics model selected to convert the reservoir properties to elastic properties was the stiff-sand model (Gal et al., 1998). This model was selected based on its visible fit to the data and because the depth and age (Jurassic) of the reservoirs suggest the rocks should be well consolidated. This model includes parameters for pressure, critical porosity, coordination number, and shear-stiffness reduction. The values used for these parameters were 30 MPa, 0.4, 7, and 1, respectively. Similar models intended for use with soft or cemented sands could have been used if the well data suggested their implementation. Furthermore, simpler models could also have been used here, such as the Raymer et al. (1980) or Wyllie et al. (1956) equations, combined with a shear-wave velocity prediction.
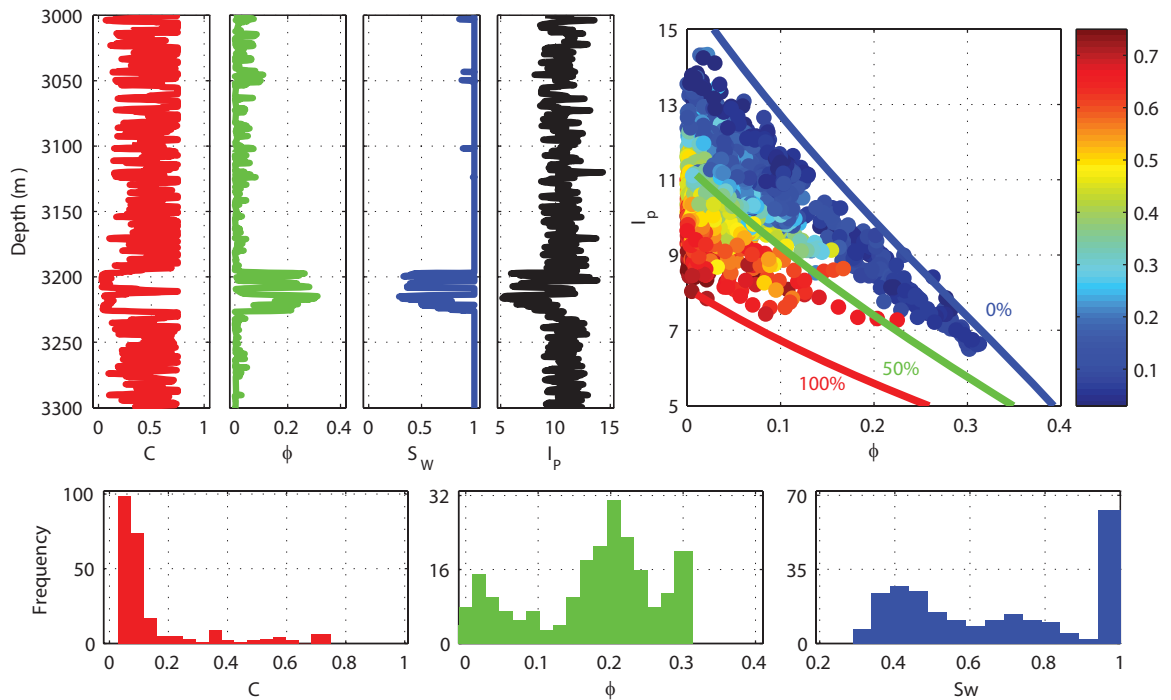
Figure 4.2. (a) Clay content C, total porosity ϕ, water saturation S_w, and P-impedance I_P around the reservoir interval (3195–3225 m) of the calibration well. (b) The calibration-well data fluid-substituted to 100% brine saturation, overlain with model lines calculated using the rock-physics model for clay contents of 0%, 50%, and 100%. The color scale for data points indicates clay content. (c) Reservoir properties within the reservoir zone.

The prior distributions were defined as uniform distributions with ranges $C = [0, 0.2]$, $\phi = [0.18, 0.32]$, and $S_w = [0.2, 1.0]$. For the numerical algorithm to operate, the uniform

distributions were discretized at increments of 0.01 for C and ϕ, and 0.10 for S_w. Reservoir thickness was determined from well data and held constant at 30 m. For every realization, each reservoir property was constant vertically within the reservoir unit. After defining the prior distributions, regularized grid sampling was performed to generate the complete set of earth models.

Figure 4.3 displays crossplots of the reservoir properties and the correlation coefficients for each pair. The correlation coefficient is –0.659 for $C - \phi$, –0.847 for $\phi - S_w$, and 0.524 for $C - S_w$. Although the second correlation value is quite high, the other two justify the independent treatment of the priors.
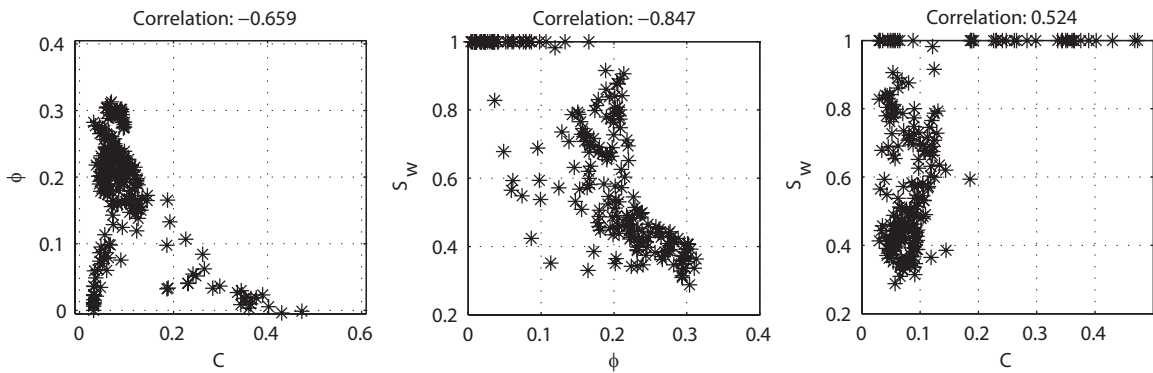
Figure 4.3. Crossplots and correlation coefficients of reservoir properties within the reservoir zone of the calibration well.

Seismic modeling was performed using an isotropic P–P ray tracer. The wavelet used was extracted from the real data at the calibration well location. The entire depth range of the well data was used in the ray tracing, where the shale elastic properties were taken from the calibration-well data, and only the properties in the reservoir unit were varied. Angle gathers were calculated from 0° to 20°, and stacked traces were calculated over the same angle ranges as the angle stacks.

Use of constant reservoir properties vertically may represent simplistic reservoir configurations. Two factors predicate this assumption. First, seismic resolution and the depth of the reservoir are sufficient to illuminate the reservoir but not to define any internal structure. Second, the internal configuration is unknown away from the well. To

invoke some constraints on this structure would introduce significant uncertainty, particularly in an exploration setting. Thus, to be as noncommittal as possible, the constant properties are used.

The trace-based data comparison of the likelihood function calculation was then performed. Three parameters were determined experimentally by testing the algorithm using the real data trace at the calibration well: the length of the cross-correlation window, the proportion of matching traces to accept, and the correlation threshold. The values obtained for these three parameters were 120 ms (about one period), 20%, and 70%, respectively.

4.5 Results

Calibration of the inversion parameters was performed first at the calibration well using the real seismic data. Results shown (Figure 4.4) are posterior marginal and bivariate joint distributions and an isosurface for the 90th percentile value from the posterior joint distribution determined at one point on the geobody. Each marginal distribution is superimposed on its prior uniform distribution. The marginal distributions for C and S_w are broad, whereas the ϕ marginal distribution is relatively narrow. This indicates that C and S_w weakly affect the seismic response. Conversely, the narrow range of ϕ means that ϕ has a dominant influence on the seismic response. The bivariate posterior distributions reiterate what is observed in the marginal distributions; for a given value of ϕ, broad ranges of C and S_w are possible.
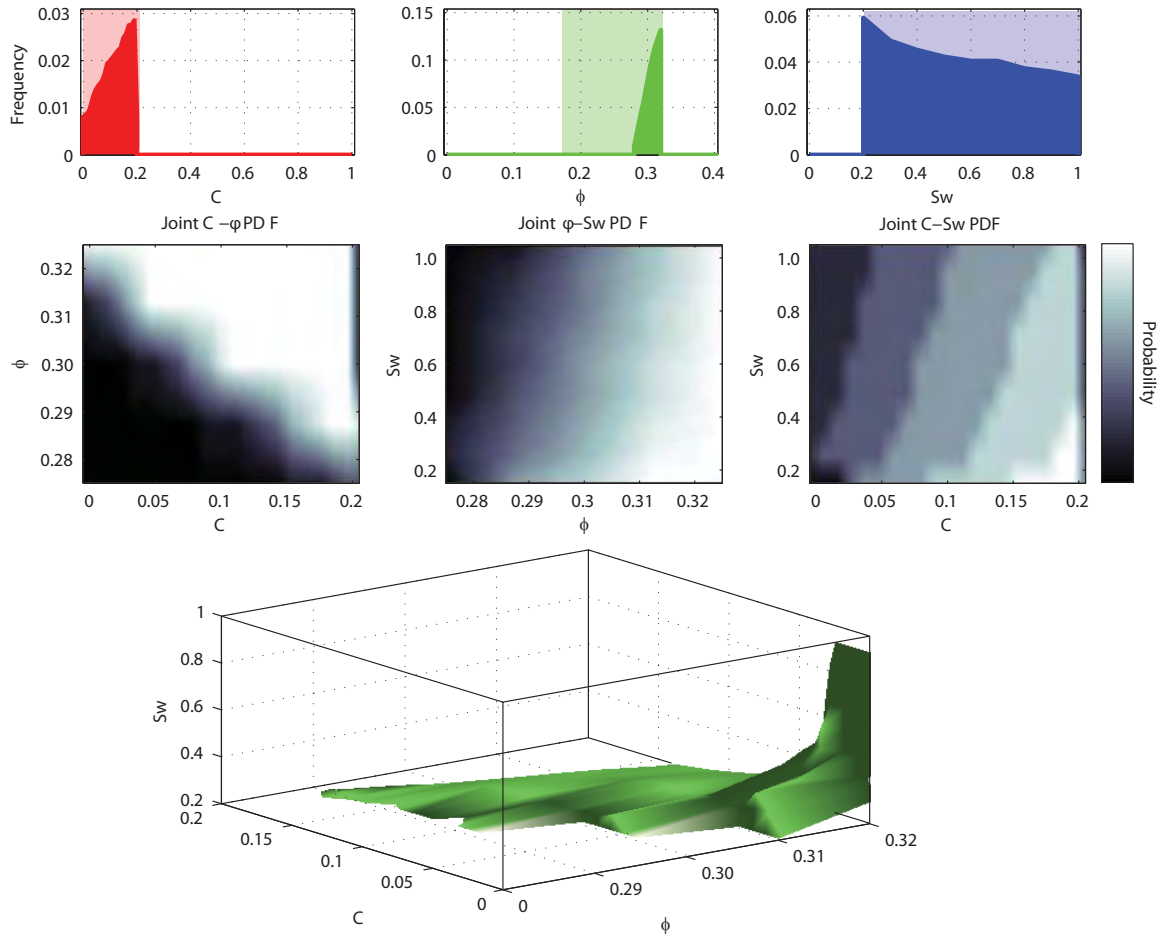
Figure 4.4. Posterior marginal (top panels) and bivariate (middle panels) joint distributions calculated at the calibration well using real seismic data at the well location. Each marginal distribution is superimposed on its prior uniform distribution. The bottom panel is an isosurface for the 90th percentile value from the posterior joint distribution.

The isosurface of the 90th percentile value (Figure 4.4) shows the values of the reservoir properties that, taken together, are likely to occur. The isosurface passes through a relatively limited number of combinations of the reservoir properties compared to the prior distribution. Selecting a most-likely combination of the reservoir properties from this isosurface would result in a predicted ϕ value with relatively low uncertainty. Predicted values of C and S_w from the joint distribution would be more uncertain. However, for all three parameters, the predicted values fall within the histograms of the reservoir properties in the reservoir (Figure 4.2). The overprediction of ϕ is evident in all posterior distributions, with more uncertain predictions of C and S_w.

Figure 4.5 allows comparison of real seismograms at the calibration well and the test well with synthetic traces for different combinations of modeled reservoir properties. The synthetic traces were accepted in the inversion routine when it was applied to the real data at the calibration. Figure 4.5 demonstrates the differences between the real and accepted synthetic traces from the inversion. Most noticeably, the traces with higher modeled ϕ (28%–32%) have apparent frequency content more similar to the real data than do the synthetic traces with lower modeled ϕ (18%–22%). The inversion rejected all traces with 18%–22% ϕ.
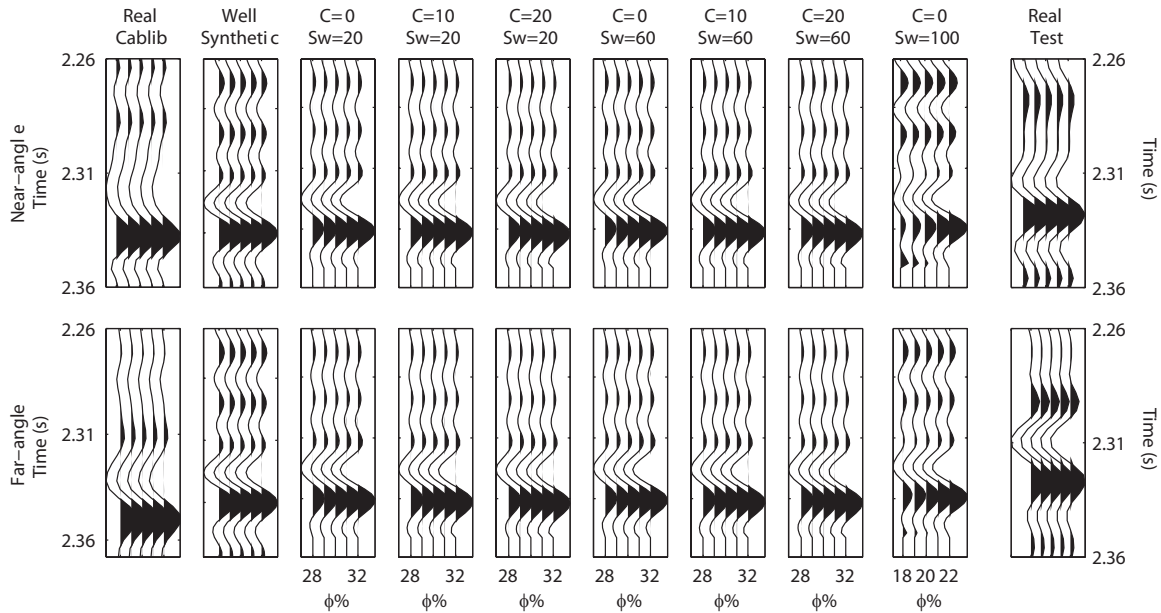
Figure 4.5. Comparison of real and synthetic traces for the calibration well and a subset of synthetic traces from the complete set of modeled traces. The subset of modeled traces includes some of those that best matched the real data. The real data from the test well location are also shown and match the synthetic traces well.

Next, a synthetic seismogram was computed that was derived from the real well data. This seismogram was used as a proxy for the real data when performing the inversion. This was done to test how the noise in the real data affected the probabilities of the reservoir properties. The posterior distributions obtained in this test (Figure 4.6) are very similar to those obtained using real seismic data at the well location (Figure 4.4), showing that noise in the real data did not affect the inversion results. These data also show that porosity is the dominant factor in the elastic response of the reservoir unit in this case.

This is explained by the rock-physics model (see Figure 4.2): for the range of relatively high ϕ, the elastic properties are weakly dependent on C and S_w, as illustrated by their broad distributions. The isosurface through the 90th percentile for the synthetic data (Figure 4.6) differs from that of the real seismic data (Figure 4.4) for predicted values of S_w, but similar ranges of ϕ and C are predicted. Overall, the overprediction of ϕ is the most evident result.
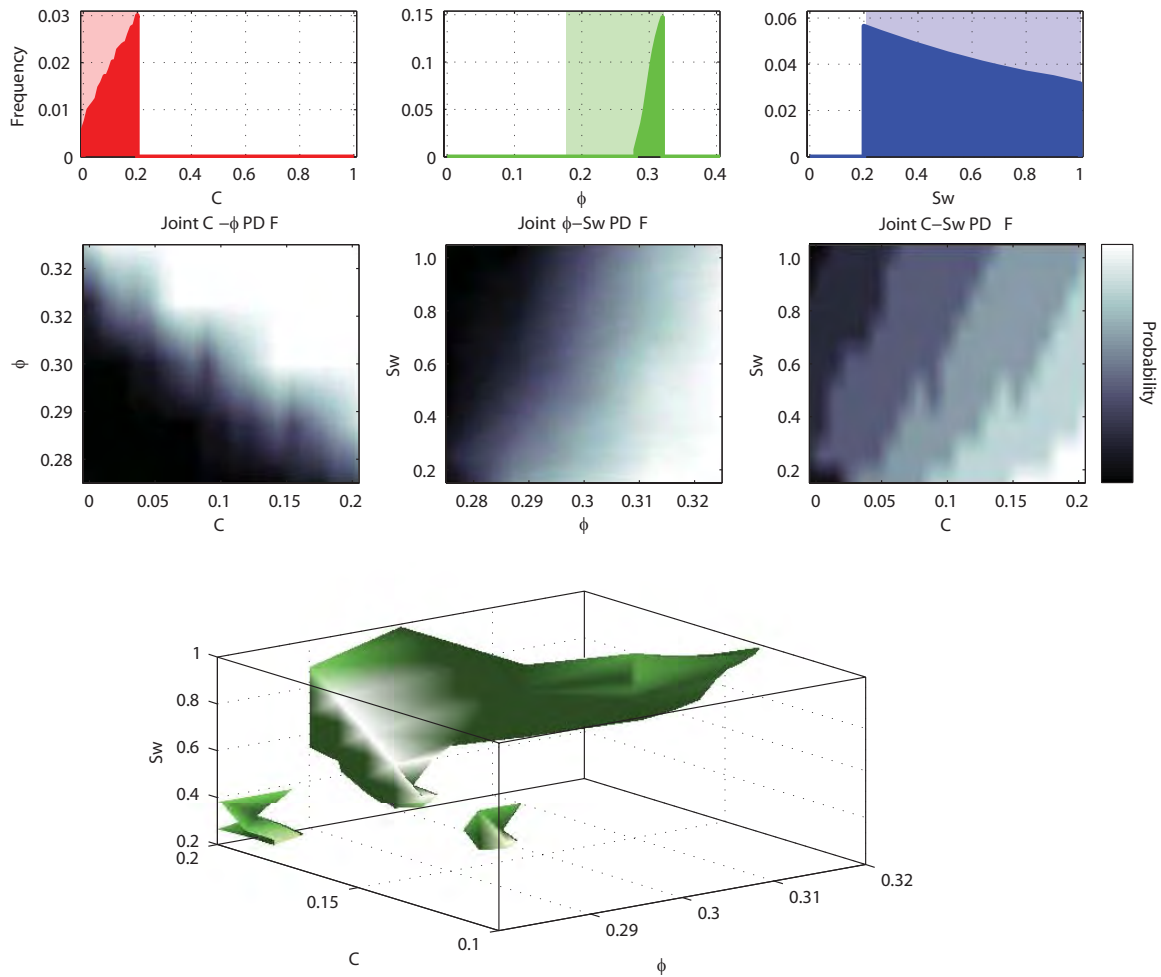
Figure 4.6. The noise test. Posterior marginal (top panels) and bivariate (middle panels) joint distributions for a synthetic seismogram generated at the calibration well. Each marginal distribution is superimposed on its prior uniform distribution. The bottom panel is an isosurface for the 90th percentile value from the full posterior joint distribution.

The inversion was then applied to the real data trace at the test well; this provides a blind test of the method. Data for this well are displayed in Figure 4.7, along with

histograms of the three reservoir properties within the reservoir unit. The well-data impedance is plotted versus porosity for a brine-substituted scenario to demonstrate that the same rock-physics model describes this well data. The gas reservoir in this well is approximately half the thickness of the reservoir in the calibration well. In addition, the ϕ range in this well differs from the range in the calibration well. The prior interpreted geobody is mapped in the near- and far-angle stacked sections corresponding to this reservoir unit (Figure 4.1). Real seismic data at this location are shown in Figure 4.5.
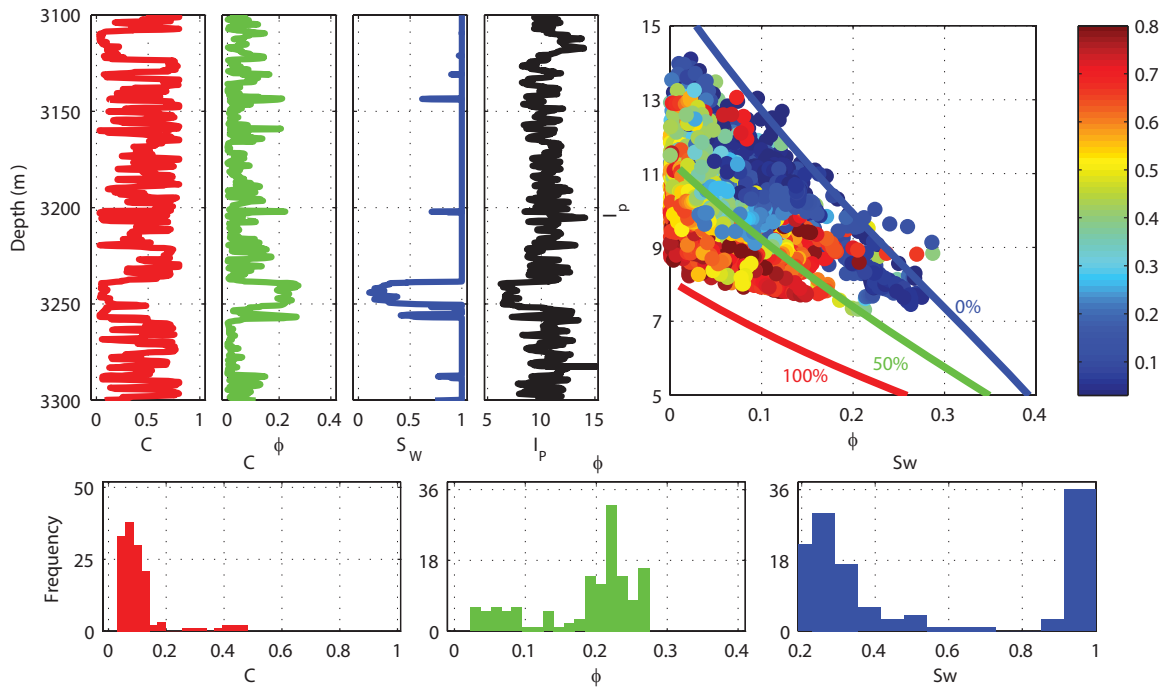
Figure 4.7. The blind test. (a) Clay content C, total porosity ϕ, water saturation S_w, and P-impedance I_P from real data at the reservoir interval of the test well. The reservoir unit in the test well is approximately half the thickness of that of the calibration well. (b) The test well data fluid-substituted to 100% brine saturation, overlain with model lines calculated using the rock-physics model for clay contents of 0%, 50%, and 100%. The color scale for data points indicates clay content. (c) Reservoir properties within the reservoir zone.

Inversion results at the test well location are shown in Figure 4.8. Most notably, ϕ is overpredicted. As in the result at the calibration well, ϕ exerts the most control, whereas C and S_w do not affect the elastic response as much. The posterior distributions most resemble those from the inversion of real data from the calibration well (Figure 4.4). As shown in Figure 4.8, the probability distributions of C and S_w are again broad, whereas

that for ϕ is localized around 0.3. The isosurfaces for the inversion of the real data at the calibration well (Figure 4.4) and for the test-well data (Figure 4.8) are similar. Predicted values of the reservoir properties and their probabilities from the joint posterior distribution at the test-well location are very similar to those obtained at the calibration well (Figure 4.4).
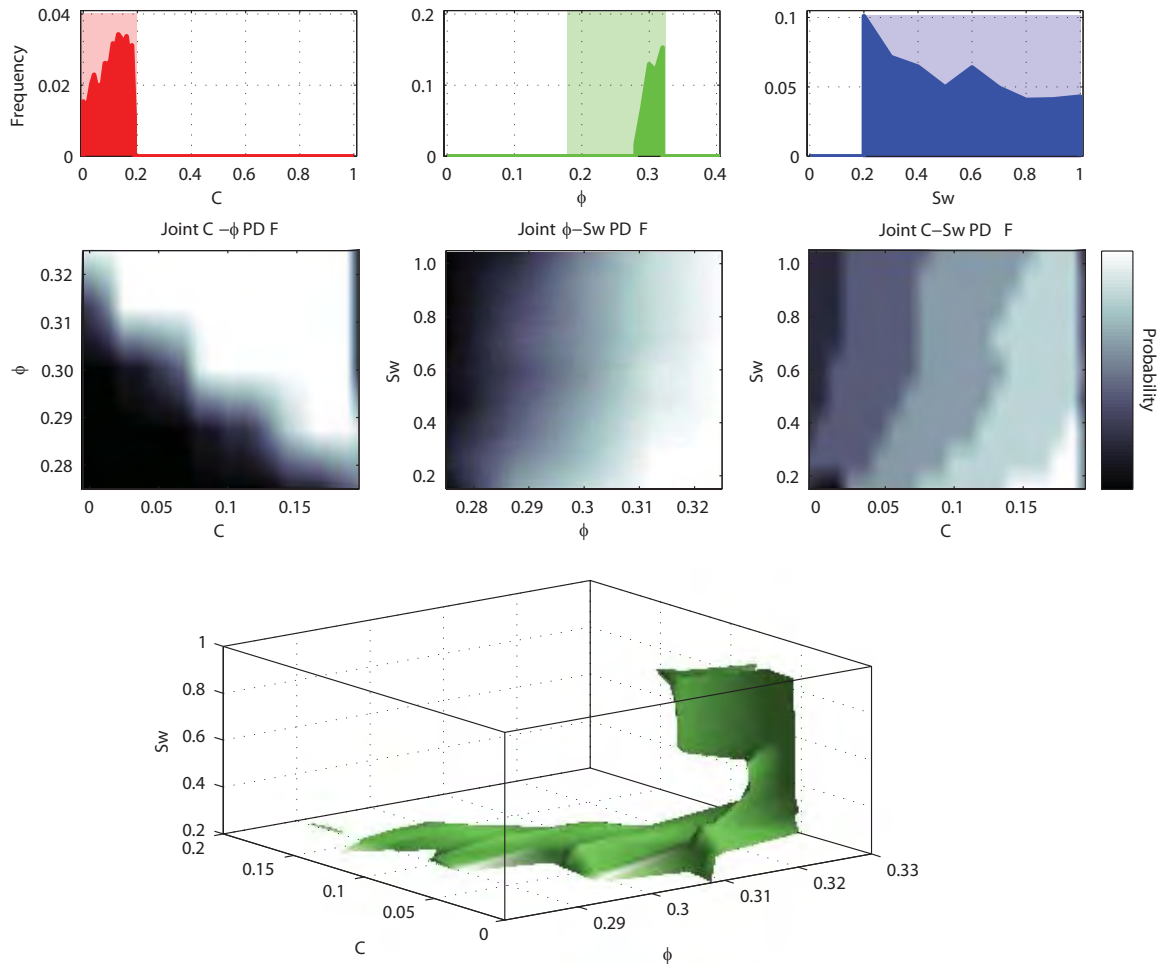
Figure 4.8. The blind test. Posterior marginal (top panels) and bivariate (middle panels) joint distributions for real data at the test well. Each marginal distribution is superimposed on its prior uniform distribution. The bottom panel is an isosurface for the 90th percentile value from the full posterior joint distribution.

Figure 4.9 illustrates the results of the inversion when applied to the 3D seismic data. At each applicable trace location where the inversion operated, posterior distributions were calculated as in Figures 4.4, 4.6, 4.8. The most likely values of the reservoir

properties were selected from the joint posterior distributions. Figure 4.9 displays the most likely values of C, ϕ, and S_w, mapped onto the geobodies. By-products of the reservoir-property inversion are most likely values of elastic properties. The values of the reservoir properties displayed in Figure 4.9 are combined into the rock-physics model, and the elastic properties are output. Figure 4.9 also shows maps of P-impedance, S-impedance, and Poisson's ratio.
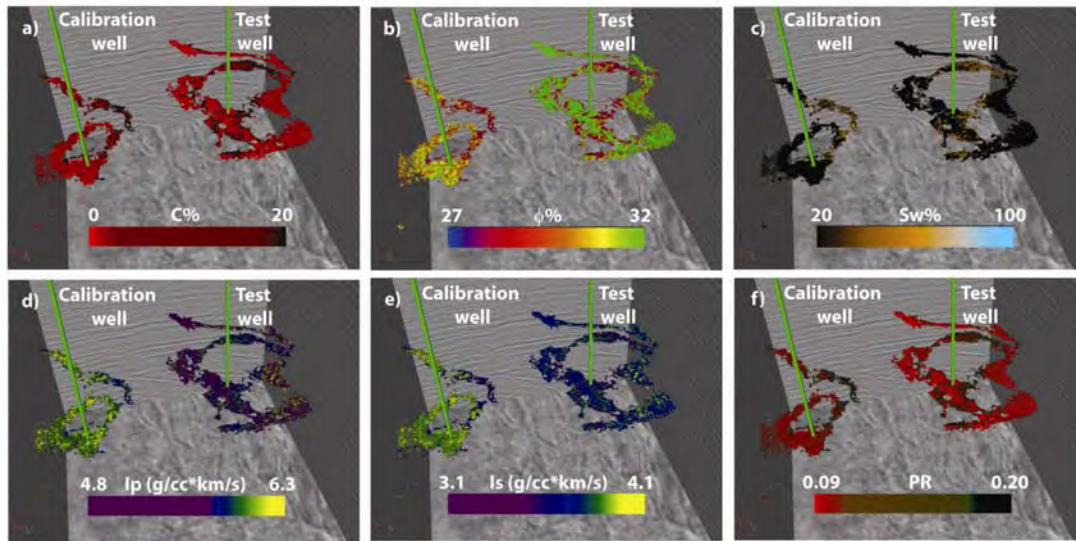
Figure 4.9. Images in three dimensions of the geobodies shown in Figure 4.1 with (a) clay content, (b) porosity, and (c) water saturation mapped onto them. The values displayed are the most likely values present in the posterior distribution at each trace location. By-products of the inversion are values of the elastic properties: (d) P-impedance, (e) S-impedance, and (f) Poisson's ratio correspond to the most likely reservoir properties (a-c).

4.6 Discussion

The results of the inversion indicated that ϕ was primarily responsible for the seismic response. For this particular well-consolidated reservoir rock, C and S_w weakly affected the response, so their posterior distributions were relatively broad. In addition, the claim was made that a combination of porosity and thickness dominates the seismic response. A sensitivity analysis of thickness and porosity supports this claim. This analysis was performed by varying the thickness from half (15 m) to twice (60 m) the thickness in the calibration well for different values of ϕ, while keeping C and S_w constant at 0.05 and 0.3, respectively. The values of ϕ ranged from 0.18 to 0.39 at a 0.01 increment. Using

the real data at the calibration well, the inversion was performed for each individual value of ϕ.

Figure 4.10 displays the combination of all the posterior thickness-porosity bivariate distributions obtained from each inversion. This distribution indicates that for lower modeled ϕ values, a larger thickness is needed to match the seismic response. Conversely, higher ϕ values correspond to smaller thicknesses. These relationships support the claim that the controlling factor of the seismic response for these data is a highly negative correlation between thickness and ϕ. Such a combination is, in essence, the goal of reservoir characterization during exploration because it provides the needed volumetrics.
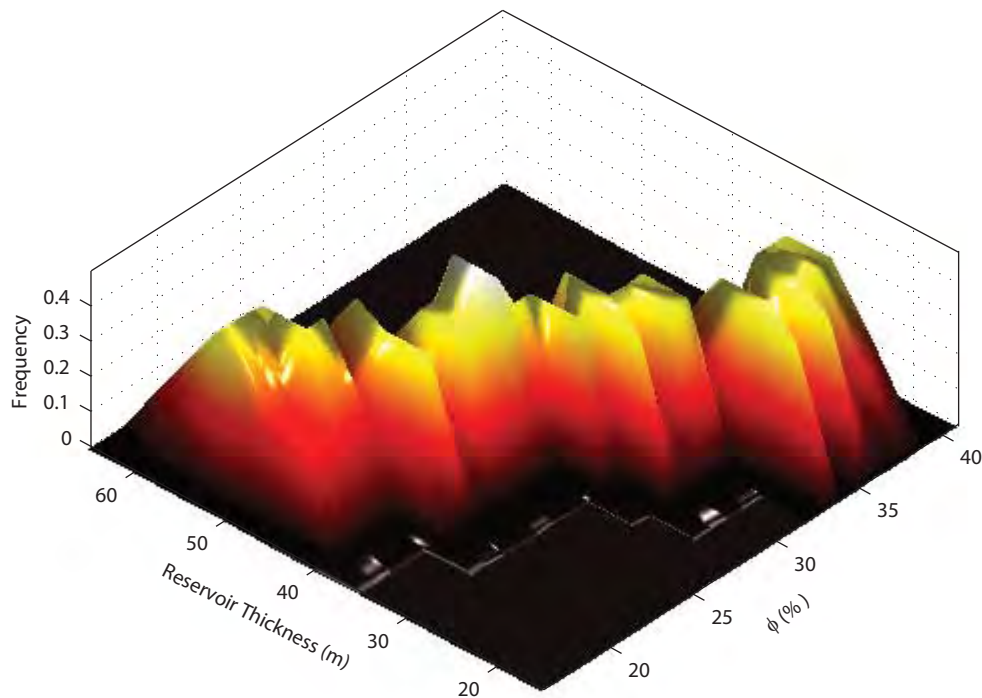
Figure 4.10. Results of sensitivity analyses carried out by inverting real data from the calibration well for variable thickness and porosity, while keeping clay content and water saturation constant. The z-axis and color represent probability; warmer colors indicate higher probability.

An additional cause of the overprediction of ϕ in both wells may be the values of the elastic properties of the overlying and underlying shale. The values used in the modeling came directly from the calibration well; only the elastic properties inside the reservoir were varied. If the elastic properties of the shale in the calibration well were significantly different from those in the test well, then this might help to explain the overprediction of ϕ. However, Figures 4.2, 4.7 show that the impedance values in the two wells are similar, so the effect of the shale properties is not the likely cause.

The display of real seismic traces and a selection of synthetic seismic traces (Figure 4.5) indicates a likely reason for this overprediction that acts in conjunction with the porosity-thickness effect. Synthetic traces generated directly from the well data (Figure 4.5) are slightly higher in frequency content than the real traces. This might be explained by the frequency of the wavelet, which was extracted from the seismic data. The other displayed synthetic traces correspond to ϕ greater than that in the well; their apparent frequency content is similar to the real data. Higher modeled ϕ values in the reservoir translate to slower velocity, which results in an apparent frequency drop. As a result, the traces that correspond to higher modeled ϕ more closely match the real data, and this is the primary cause for the overprediction of ϕ from the inversion.

Although the forward-modeling parameters were chosen carefully to match the real data as well as possible, the modeling was not perfect. This imperfection caused the overprediction of ϕ in conjunction with the porosity-thickness relationship. To avoid this situation, the frequency of the wavelet could be reduced. Alternatively, a calibration of the wavelet at the well using the observed ϕ might help to improve the method.

The posterior distributions that contain information about C and S_w in general show broad ranges of these parameters. This is expected, given their weak influence on the seismic response. One constraint the data imposed on the inversion result was its limited angular range, so the full capability of the inversion using far-offset information unfortunately was not demonstrated. However, if data from wider angles had been included, the expected results would likely have narrowed the posterior distributions, particularly those that included the C parameter.

A related aspect deals with the stiffness of the reservoir rock. The elastic properties of the reservoir rock, described by the stiff-sand model, are not changed greatly by variations in fluid. Therefore, data from wider angles would provide improved lithology prediction, but the saturation prediction would likely remain broad for this data set.

The ranges and discretization increments of the prior distributions define the size of the model space and thus control the overall speed of both the forward and inverse problems. However, how can the ranges and increments be determined? First, the parameters that most affect the seismic response must be determined. These parameters should be discretized finely over a suitable range for the data at hand. The other parameters that do not significantly affect the seismic data can be discretized on a much coarser grid. For example, in the data set used in this study, the ϕ increment needed to be fine. However, the S_w increment likely did not need to be 0.10; rather, two values, a low and high fraction, may have been sufficient. The increment for C was also possibly unnecessarily fine, given its weak effect on the seismic response. Lastly, if the real seismic data are significantly noisy, then the prior parameters need not be discretized as finely, because the variations in the synthetic data will be too small relative to the noise-induced variations in the real data.

Although these guidelines may provide constraints for the ranges and increments, no black-box method will provide satisfactory results for all data sets. The user will have to determine these parameters through numerical experiments to determine the sensitivity of each of the parameters and the noise level of the real data.

4.7 Conclusions

This study demonstrated a rock-physics motivated Bayesian formulation to invert seismic amplitude and well data for reservoir properties. Several key assumptions were made, because development of the methodology was focused on use in an exploration setting. Those assumptions included a prior interpretation of the seismic data and constant reservoir thickness. Independence of the prior reservoir-property distributions was also assumed, although this is not essential for all implementations. The prior

distributions were sampled regularly to form a complete set of earth models. Then, a full grid search of the corresponding complete set of seismic models was performed. This parameterization, including the prior seismic interpretation, allowed optimal realizations from the posterior distribution to be obtained.

Inversion results included trace-by-trace marginal and joint posterior distributions of the simulated reservoir properties for the reservoir unit under examination. In general, the stiff character of the rock prevented a low-uncertainty prediction of S_w. Furthermore, the posterior distributions containing the C parameter were broad. This was likely because the narrow angle of incidence (maximum 20°) of the seismic data did not provide the angle-dependent information necessary to provide robust predictions of C from the posterior distribution. Porosity was overpredicted in most cases, but those results, coupled with additional sensitivity analyses of variable thickness, showed that a porosity-thickness relationship could be predicted reasonably well for this data set. Therefore, the inversion was successful in characterizing these reservoir properties. The strong negative porosity-thickness correlation revealed here arises because the reservoir becomes stiffer with reduced porosity and has a smaller negative contrast with the surrounding shale. This result is site specific. It may change as the impedance-porosity relationship varies.

Overall, the inversion method provided the potential to map probabilistic geologic heterogeneity within a potential reservoir unit from seismic data. Although the potential of the technique was demonstrated when the variable thickness parameter was not included, this geometric parameter should be included as a full prior parameter. The remaining chapters include a full prior parameterization of thickness. There are other limitations, including the use of homogeneous internal reservoir architecture. Assessment of these effects can also be included within the framework presented. Further, the uncertainty in the prior seismic interpretation can also be included, possibly through one or more of the suggested methods discussed in the Introduction.

The utility of this method is that probabilistic reservoir properties and associated uncertainties can be obtained directly from seismic data, even if well data are not available. The method is applicable for any geologic setting if an appropriate rock-

physics model is used. Selection of a geologically relevant rock-physics transform is the key to solving the problem. The uncertainty of a prediction will naturally be higher in the absence of well data. The probabilistic reservoir-property maps produced using the method described here can provide useful information for geologists and engineers to use in producing geologic maps and developing fluid-flow models.

4.8 Acknowledgments

Chapter 5
Uncertainty analysis of seismic-inversion scenarios

"In science the credit goes to the man who convinces the
world, not the man to whom the idea first occurs."
--Sir Francis Darwin

5.1 Abstract

We examine the change in accuracy and uncertainty of model-based seismic inversion results when inverting for different combinations of thickness, clay content, porosity, and saturation. The Bayesian-based algorithm operates on a seismically identified geobody and utilizes a full-grid search to obtain the posterior conditional probability distribution function. The reservoir rocks under examinations are stiff and consolidated, which makes fluid detection difficult. Furthermore, the dataset excludes far-angle amplitude data, which inhibits accurate lithology predictions. First we invert the seismic data for thickness and porosity, the two properties that most influence the seismic response. Next, clay content is combined with the two dominant properties. Third, we invert for thickness, porosity, and saturation. Last, we invert for all four properties simultaneously. Results for the thickness-porosity inversion substantiate a

trade off between thickness and porosity that controls the seismic response. This result occurs at three gas wells, but an opposite trend appears at a wet well. Including clay content in the inversion substantially increases the uncertainty in all predictions. In conclusion, the inversion is able to assign probabilities to potential gas sands and to higher-porosity brine sands, despite the stiffness of the reservoir rocks. Inversion scenarios that included clay content showed that mineralogy is the most uncertain parameter, primarily because of the narrow angle ranges present in the seismic data.

5.2 Introduction

Seismic data often provide the only information to characterize large areas of the subsurface for hydrocarbon exploration. Well data may be present near the area where seismic data are available, but they augment the seismic data at limited locations. Therefore, characterizing potential reservoir units from seismic data involves reducing an under-determined problem by including assumptions or other known or estimated geologic information. Even with physically based assumptions, the seismic data may not easily lend itself to the detection of reservoir properties. Nonetheless, a priority in an exploration setting is to translate this data into meaningful maps or volumes describing the *in situ* geologic conditions. This must be done despite the inherent deficiencies of the seismic data.

One of these deficiencies is the non-uniqueness of the seismograms, which prevents one-to-one mappings of the seismic amplitudes to reservoir properties. This non-uniqueness requires the use of statistical techniques to reduce the set of solutions to a manageable and describable form. Many authors have chosen the Bayesian method because of its ability to integrate different types of data. This method can be used to invert seismic data directly for rock properties as described in Buland and Omre (2003), Gunning and Glinsky (2007), Acevedo and Pennington (2003), Coleu et al. (2005). In all these instances, a rock-physics model converts rock properties to elastic properties or vice versa (see Avseth et al., 2005 for a current synopsis). However, rock-physics models are valid at the well-log scale, not the seismic scale. Model-based inversion approaches

provide the opportunity to model reservoir properties directly at the scale appropriate for rock-physics models. Then the rock-physics model converts these properties to the elastic domain, from which a synthetic seismic data set is generated. These seismic data, along with prior information, can then be used to generate posterior distributions of modeled reservoir properties. Uncertainty in these posterior distributions arises from various sources, including noise in the seismic data and errors in rock-physics and seismic modeling. It also results from uncertainty in the prior distributions and the combinations of the parameters in the prior model. This source of uncertainty is the focus of this paper. Specifically, we examine how different combinations of the reservoir properties in the prior model affect the posterior results.

To examine these effects, we use a Bayesian model-based inversion algorithm capable of inverting seismic data directly for reservoir properties (chapter 4). The version presented in that paper inverted seismic data for clay content (C) (e.g. lithology), porosity (ϕ), and saturation (S_w). We extend it here to include thickness (H). This inversion method operates on a seismically identified geobody, or potential reservoir interval, and it requires an appropriate rock-physics model calibrated to input well data. The algorithm implements a full grid search to accept a specified number of synthetic traces that correlate with a real trace within a specified threshold. Although it is not required by the method, we define the prior distributions as uniform.

Examining uncertainty is important for several reasons. It reveals which properties can be predicted from seismic data along with the associated uncertainty. Second, the reservoir properties combine in different ways to produce a variety of seismic responses. This testing shows which properties combine and how they combine to produce a given seismic response. In addition, it helps to identify which, if any, parameters can be omitted to reduce uncertainty and computational demands. Lastly, this uncertainty analysis indicates to what extent the seismic data can be used to provide reliable solutions to the inherently under-determined problem.

We know that in many instances, a trade-off exists between H and ϕ on the seismic signature of a reservoir. When the reservoir thickness lies below seismic resolution, the

corresponding seismic reflection may arise from the product of H and ϕ. In this situation, high ϕ and small H may be seismically equivalent to a lower ϕ with a larger H. Furthermore, these two properties, or the combination of them, may dominate the seismic response relative to the contributions of other reservoir properties such as lithology and saturation.

We use *P-P* reflection seismic data with limited offset information. Even in the case of inverting for only two parameters, H and ϕ, we are dealing with a non-unique problem in which the available seismic data does not measure enough parameters. In addition, the thicknesses of the potential reservoir units fall below the resolution limit, and the stiffness of the consolidated reservoir rocks inhibits fluid discrimination. We begin the uncertainty analysis by first inverting the seismic data for only H and ϕ. Then we include C simultaneously with H and ϕ. Third, S_w is included with H and ϕ. Last, we invert the seismic data for all four parameters simultaneously.

Results indicate that H and ϕ dominate the seismic response, meaning that predicting them or the combination of them is the most certain outcome from the inversion. Additional results also indicate that in some cases, H, ϕ, and S_w combine in ways to allow for a prediction of S_w. However, the limited offset information in the seismic data prevents an accurate prediction of C. These results as a whole demonstrate how including additional parameters increases uncertainty in the joint prediction of the reservoir properties. They also imply that inverting for lithology may not be necessary for the dataset used here. Excluding this parameter may reduce the computational requirements by an order of magnitude.

5.3 Method

The Bayesian inversion equation provides a platform on which to link any known information (the prior model) with a calculated probability of the data occurring given the model parameters (the likelihood function), yielding the probability of the model parameters given the data (the posterior distribution). More specifically, the posterior distribution is the conditional probability distribution function (PDF) of the modeled

reservoir parameters m given the data d (Equation 5.1). Model reservoir parameters are any combination of H, C, ϕ, and S_w; data include near-angle (A_N) and far-angle (A_F) stacked amplitude seismic data.

$$P(m \mid d) = \frac{P(m)P(d \mid m)}{P(d)} \tag{5.1}$$

where

$$P(d) = \int P(m)P(d \mid m)dm. \tag{5.2}$$

We examine how the posterior distributions of the modeled reservoir properties change when $m = [H, \phi]$; $m = [H, C, \phi]$; $m = [H, \phi, Sw]$; and $m = [H, C, \phi, Sw]$. Thickness and porosity are used for the two-parameter inversion and for all subsequent scenarios, because previous results indicate that these two properties have the most significant effect on the elastic and seismic responses (Spikes et al., 2007). In each case, an undetermined problem exists, and we examine how the uncertainty in the posterior PDF changes with the addition of more reservoir properties.

For each inversion scenario, three user-specified parameters must be defined. First, the number of synthetic traces to accept must be specified. Accompanying that is an initial correlation threshold, below which poor matches exist between real and synthetic data. Third of these is the length of a window in the real and synthetic seismic data over which the cross-correlation operation is performed. We empirically determine these parameters at the calibration-well location.

Prior information consists of uniform distributions of the model reservoir parameters with specific numerical ranges and increments. The reservoir interval is defined in the input well and in the form of a geobody in seismic data. An appropriate rock-physics model is calibrated to the input well data. The forward problem involves exhaustive modeling of all combinations of reservoir properties within the reservoir interval, which results in a complete set of three-layer earth models. Shale properties above and below

the reservoir interval are copied from the input well data. The chosen rock-physics model converts each earth model to an elastic-property model. Synthetic seismic data are calculated from each elastic-property model.

The inverse problem consists of cross-correlating windows of all modeled traces with a window from a real trace. Then the user-specified percentage of the synthetic traces, within the correlation threshold, is accepted, and all others are rejected. The modeled reservoir parameters corresponding to the accepted traces form the likelihood function. The number of accepted synthetic traces in a correlation threshold defines the width and shape of the likelihood function in the absence of a formal objective function. When the likelihood function is multiplied by the prior distribution and normalized by the probability of the data, then the full conditional posterior distribution is obtained (Equation 5.1). We estimate the probability of the data using a normal distribution (Equation 5.3). The matrix B is the covariance matrix of the real near- and far-data traces, r is the two-element vector of real near and far trace energies, and s is the two-element vector of energies of matching synthetic traces.

$$P(d) = \frac{1}{2\pi \det(B^{-1})} e^{-[r-s]^T B^{-1} [r-s]} \tag{5.3}$$

This model-based inversion algorithm operates on a trace-by-trace basis using a geobody defined by an interpretation of seismic data. That interpretation guides the location of the cross-correlation window of a real trace. This can be considered a drawback, but it speeds the inversion algorithm by removing the window-based searching of an individual real trace for a reflection. Although the uncertainties of these surfaces are not included in the probabilistic calculations, an estimate of the uncertainty of the data itself is included in the Bayesian formulation (Equation 5.3). An additional assumption is that the model reservoir parameters in each earth model are homogeneous. Although this does not represent all reservoirs, it is necessary to limit the number of forward models.

One purpose of using a Bayesian formulation is to include any known information in the calculation of the posterior PDF. By including this information, uncertainty in the

posterior PDF should decrease. In the case here, the prior information is anything known about the reservoir properties and any relationships among them. At a well, the values for these four properties are known with minimal uncertainty. Those values can be used to guide the definition of the prior distributions, as well as uncertainty about those values. However, how does one determine this uncertainty away from a well? In each scenario, uniform distributions are used in the prior model. This assigns equal probabilities to all values in the defined range of the parameter in question. This may be suitable for H when the reservoir interval in question is below seismic resolution, so many values of H have a chance of occurring. In terms of ϕ, this means that $\phi=0.10$ will have the same chance as $\phi=0.25$ or $\phi=0.33$. Although equal probabilities are assigned to disparate reservoir-property values, the use of uniform prior PDFs allows us to be as noncommittal as possible. This is advantageous, because potentially incorrect correlation structures are not imposed away from well control. The disadvantage is that the known information at the calibration-well location is not included.

5.4 Data

Seismic and well data used are from offshore Africa. Seismic data include near- and far-angle stacked data with angle ranges of 0°–10° and 11°–20°, respectively (Figure 5.1). Attribute analysis provided the interpretation of the geobodies that guide the window-based selection of the real traces. Data from a gas-producing well are used to calibrate the rock-physics model and the inversion parameters used to calculate the likelihood function (e.g., the percentage of traces to accept and the correlation threshold). Two other gas wells and a wet well provide test cases for each inversion scenario. Red markers indicate the well locations (Figure 5.1, bottom).
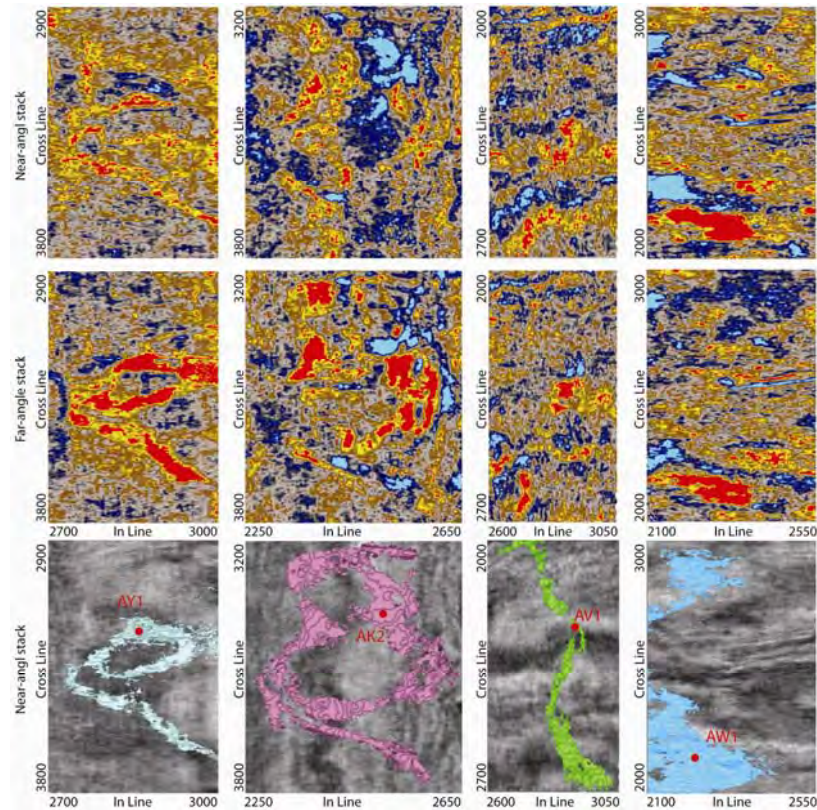
Figure 5.1. Seismic amplitude maps for near-angle (top) and far-angle (middle) data. The near-angle data represents incidence angles of 0 to 10 degrees and the bottom from 11 to 20 degrees. Red corresponds to negative amplitude and blue to positive. A class III amplitude variation with offset (AVO) effect enhances the far-angle negative amplitude reflections relative to the near-angle amplitude. An interpretation of the seismic data provides the geobodies necessary for the inversion (bottom). A well intersects each geobody, as indicated by the red markers. The AY1 well, a gas producer, is the calibration well. The AK2, AV1, and AW1 wells serve as test wells, of which the first two are gas producers and AW1 is wet.

Data from the calibration well (the AY1 well) are displayed in Figure 5.2. The rock-physics model selected to convert the reservoir properties to elastic properties was the stiff-sand model (Gal et al., 1998). This model was selected based on its visible fit to the data and because the depth and Jurassic age of the reservoirs imply the rocks are well consolidated. This model includes parameters for pressure, critical porosity, coordination number, and shear-stiffness reduction. The values used for these parameters were 30 MPa, 0.4, 7, and 1, respectively.
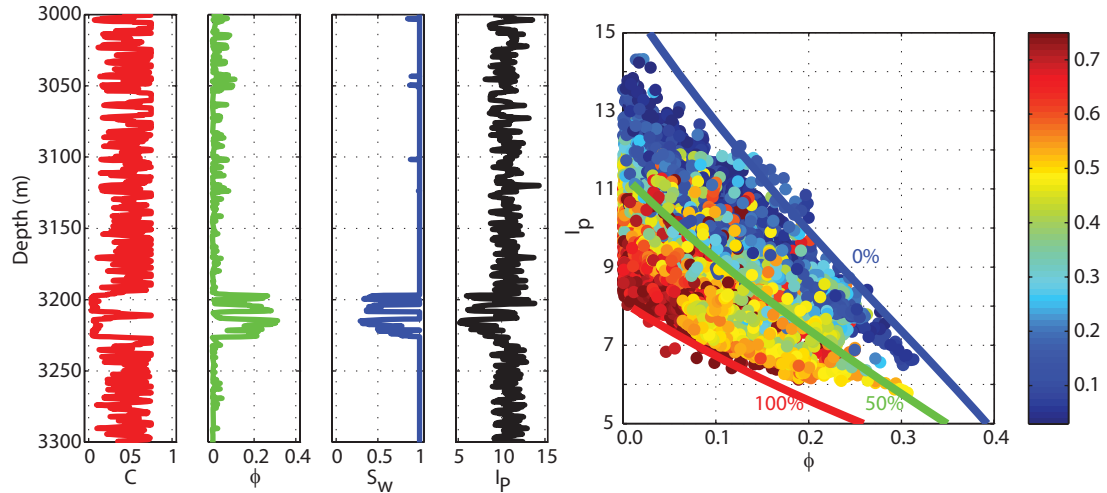
Figure 5.2. Clay content C, total porosity, ϕ, water saturation, S_w, and P-impedance I_P from the reservoir interval (3195–2335 m) of the calibration well (four-left hand panels). The right panel shows the calibration-well data fluid-substituted to 100% brine saturation, overlain with model lines calculated using the stiff sand rock-physics model for clay contents 0%, 50%, and 100%. The color scale for data points indicates well-log values of clay content.

5.5 Results

Results for each inversion scenario are the conditional posterior distribution and any marginalized versions of it for the potential reservoir unit. For the two-parameter inversion, a bivariate distribution exists between H and ϕ along with their individual marginal distributions. In the inversion scenarios with three parameters, one trivariate, three bivariates, and three marginal PDFs are output. The four-parameter inversion produces a 4-D posterior conditional, three trivariate, six bivariate, and four marginal PDFs. For each inversion scenario, the respective set of PDFs exists at each real seismic trace where a geobody exists.

We display the inversion results at all four well locations. More specifically, at the reservoir interval, most likely values of the individual reservoir properties and most likely seismic traces are superimposed on the measured well and seismic data. The PDFs from which the most likely values are drawn are the highest-dimensional posterior PDF available for that particular inversion operation. Where possible, those PDFs and the lower-dimensional ones are displayed. In addition, maps and histograms of most likely

values of the reservoir properties are constructed and presented to illustrate how the inversion results change away from the well locations.

5.5.1 Thickness-porosity joint inversion

Input parameters for the Bayesian equation in this sense are $m = [H, \phi]$ given the data $d = [A_N, A_F]$ and constant values of C and S_w. The model parameters can be viewed also as $m = [H, \phi \,|\, C = 0.10, S_w = 0.3]$. These values of C and S_w are used because they approximate the values observed in the calibration well. The prior range of H is 15 to 60 m with a 5-m increment. Porosity ranges from 0.15 to 0.35 with an increment of 0.01. Inversion parameters include an initial correlation of 90% with an acceptance of 6.5% of the total number of synthetic traces. Duration of the cross-correlation window is 160 ms, which is approximately two seismic periods.

The first set of results corresponds to the calibration well (Figure 5.3). In the leftmost panel are the measured (gray) and predicted (black) porosity logs. Next to it are the real seismic traces and those that correspond to the most likely combination of H and ϕ. On the right are the posterior bivariate and posterior marginal PDFs. The predicted log contains the most likely combination of H (30 m) and ϕ (0.22) values taken from the bivariate PDF. Measured and predicted thicknesses match, and the mean ϕ in the well is 0.24, with a predicted value of 0.22. The bivariate PDF predicted the expected relationship between H and ϕ, with small H and large ϕ trending to large H and small ϕ along with the associated uncertainty. Each marginal PDF displays an integrated version of he bivariate PDF along constant values of the given parameter.
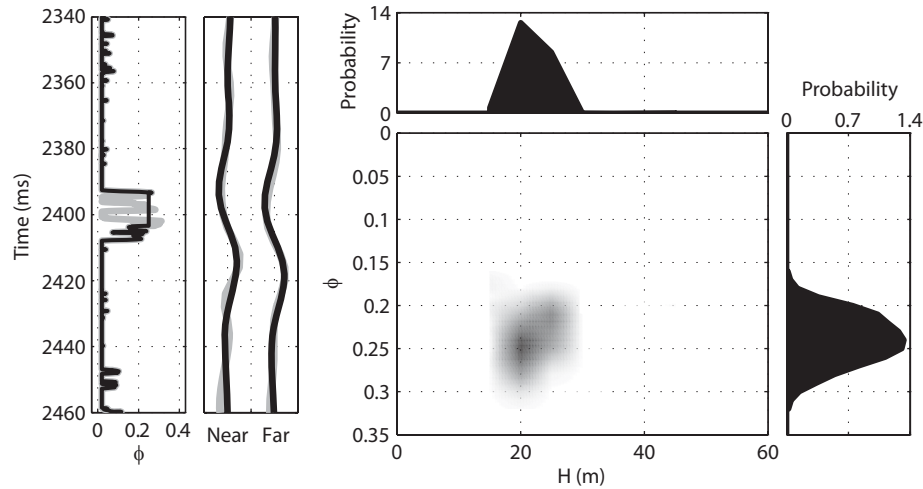
Figure 5.3. Real and predicted well data, real and predicted seismic data, and the posterior bivariate and marginal PDFs for the calibration well. Measured curves are gray, and predicted ones are black. The measured and predicted values of thickness and porosity match quite well, as do the real and best-match synthetic seismic traces. Log curves are plotted versus two-way traveltime to coincide with the seismic traces. On the right is the posterior bivariate PDF between thickness and porosity and the marginal PDFs for each property. The bivariate PDF demonstrates a trend between thickness and porosity, with high porosity and low thickness trending to low porosity and larger thickness.

The next results are the measured and predicted porosity curves and seismic traces for the three test wells and the corresponding PDFs, again taking fixed $C = 0.1$ and $S_w = 0.3$ (Figure 5.4). The color of the curves is the equivalent to that in Figure 5.3, in which the predicted curves are superimposed on the measured ones. The most likely values within the reservoir intervals are drawn from the respective posterior bivariate distributions. In each of the three wells, the inversion predicts ϕ quite accurately. However, it substantially over predicts H in the AK2 well. The real thickness of the reservoir is 18 m, but the predicted value is 40 m. The relationship between H and ϕ in this well shows the expected trend but larger-than-expected thicknesses. The corresponding best-match synthetic seismograms noticeably stray from the measured response at this well, and follow the predicted thickness curve. In the AV1 well, the inversion predicts H within 8 m, with measured and predicted values of 18 and 25 m, respectively. Mean ϕ in the reservoir is 0.21 and the predicted value is 0.24. Lastly, predicted H in the AW1 well is quite accurate, with a prediction (20 m) quite close to the measured thickness (21.5 m). Porosity, however, is under predicted at 0.16 with a mean measured value of 0.21.

Although the fluid in the well is brine, the inversion parameters do not include it ($S_w =$ 0.3). Nonetheless, accurate predictions result in the wet well. This suggests that either fluid saturation does not significantly affect the seismic response or fluid predictions depend on joint inversions with the other properties.
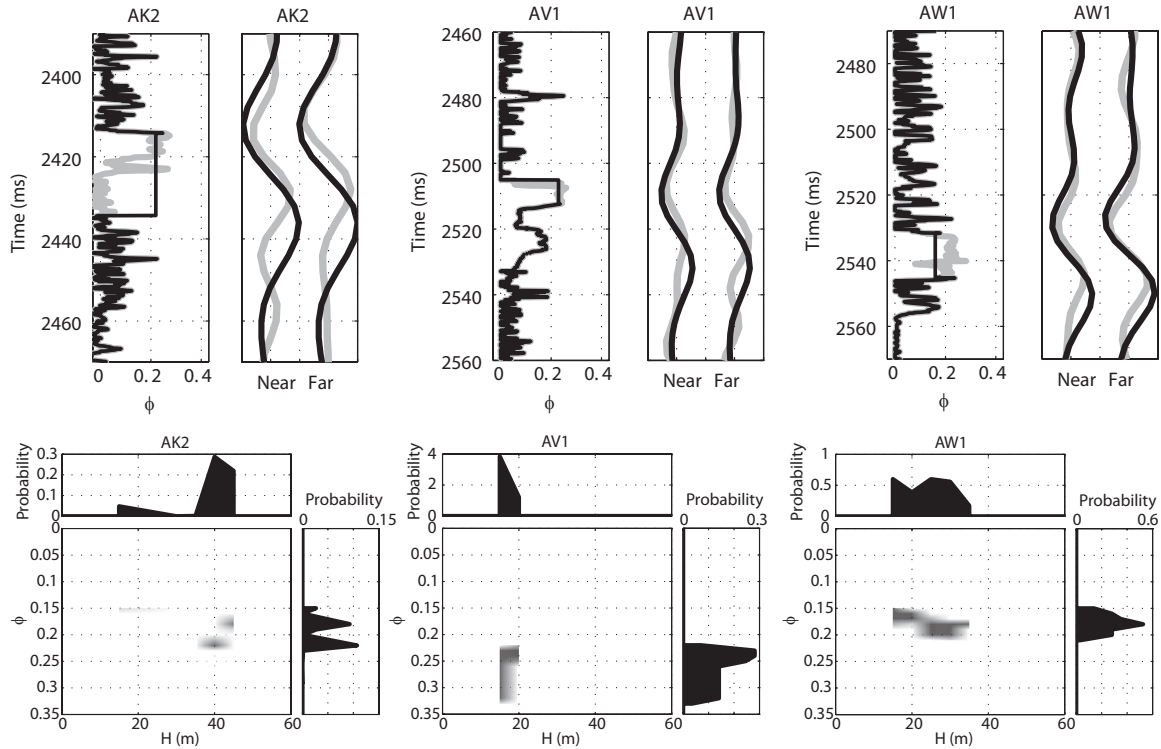
Figure 5.4. Real and predicted well data and seismic for the AK2, AV1, and AW1 wells (top, left to right). Thickness is overpredicted at the AK2 well location, but porosity is accurately estimated. The inversion predicts both properties very accurately in the AV1 well. For the AW1 well, thickness is estimated very well with a slight underprediction of porosity. On the bottom row are posterior PDFs for the three wells. The AK2 and AW1 wells (left and right, respectively) display bimodal distributions. The AV1 well (center) shows a very localized population of thickness and porosity values.

The posterior joint PDFs at the three well locations show noticeably different results. The AK2 location (left) shows a bimodal distribution of ϕ along with a slightly skewed H distribution. The AV1 posterior bivariate (center) displays a very limited relationship between thickness and porosity. Conversely, the AW1 posterior bivariate (right) displays a bimodal distribution as a result of the H contribution.

The inversion produced posterior PDFs as seen in Figure 5.4 at every trace included in the geobody (see Figure 5.1). Accordingly, the most likely values can be drawn from any PDF at any trace location to produce maps for a given reservoir property. Figure 5.5 contains maps for (top row to bottom row) H, ϕ, and their product for the four geobodies. At each location, the most likely combination of H and ϕ were drawn from the local posterior bivariate PDF. Therefore, H and ϕ values are not independent as they were in the prior model. The product of H and ϕ varies little from geobody to geobody.
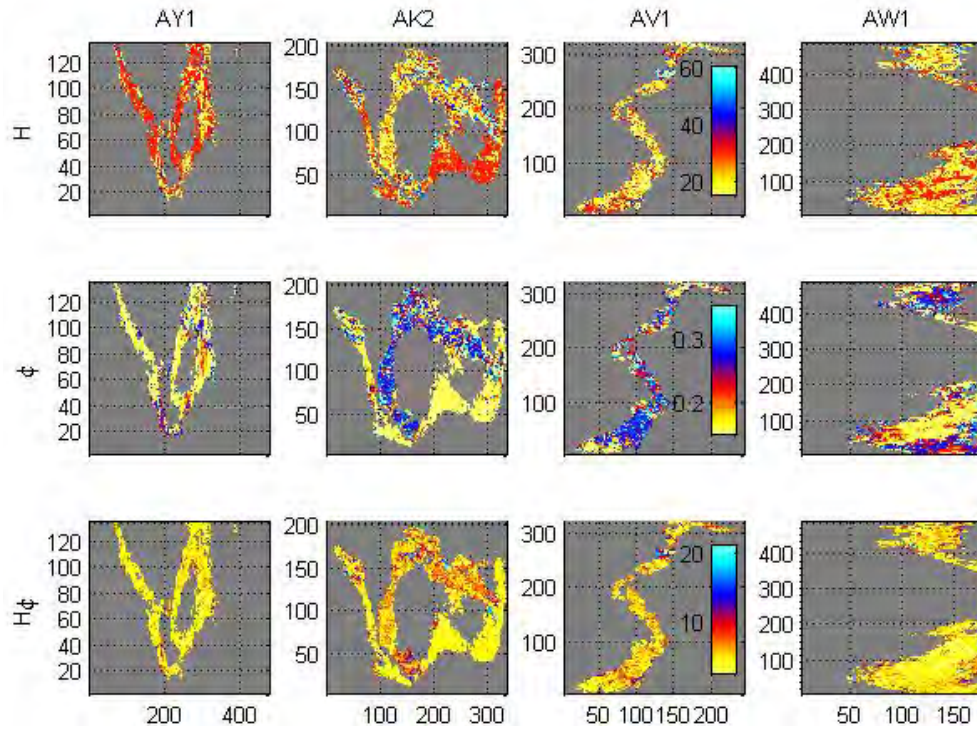
Figure 5.5. Maps of the most likely values of thickness (top), porosity (middle), and the product of the two (bottom), plotted onto the geobodies shown in Figure 5.1.

Accompanying the maps are the histograms for each geobody for each property (Figure 5.6). In all four geobodies, the H values between 15 and 35 m dominate the maps, although values greater that 50 m appear. In terms of ϕ, 0.15 is the dominant value in each geobody, with varying counts of greater values. Finally, the histograms of the product of H and ϕ indicate that the dominant value of 4.4 porosity-m is clearly the

most common value. This suggests that the inversion estimates a nearly constant volumetric quantity for each geobody, the same value predicted in the wells.
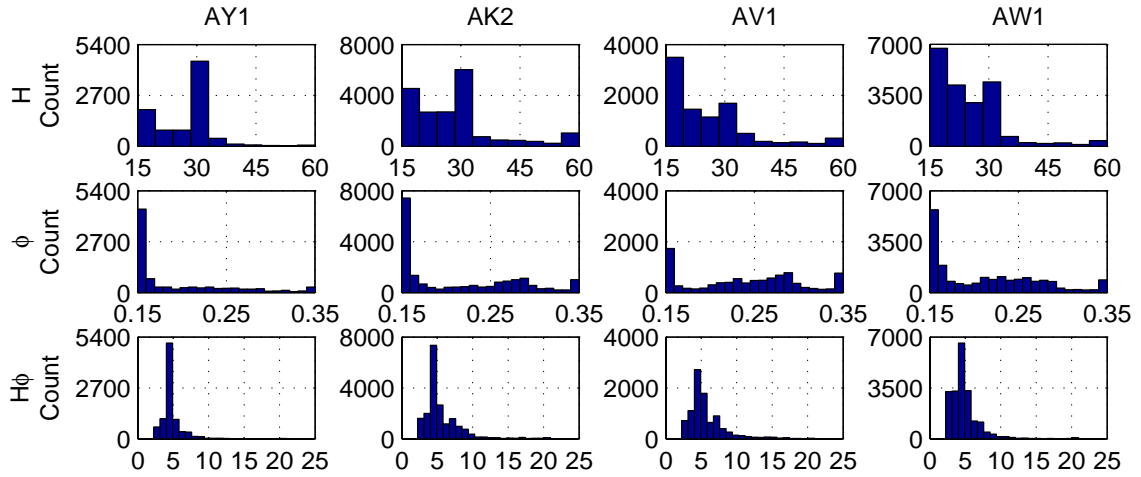
Figure 5.6. Histograms of each individual property for each geobody. The thickness values predominantly range from 15 to 30 m. Porosity is primarily skewed to the lower end. A value of 4.5 porosity-m is the most common in the thickness-porosity histograms.

5.5.2 Thickness-clay content-porosity inversion

The next set of results comes from the simultaneous inversion of H, C, and ϕ for a constant S_w. For this scenario, the modeled parameters are $m = [H, C, \phi \mid S_w = 0.3]$ with data $d = [A_N, A_F]$. The H prior distribution is assigned a range of 15 to 60 m with a 50m increment. Clay content ranges from 0 to 0.2, and ϕ ranges from 0.15 to 0.35, both in 0.01 increments. The percentage of traces to accept and the correlation threshold were reestablished for this scenario. The inversion parameters used were to accept 15% of the total traces with an initial 80% threshold.

Figure 5.7 displays the inversion results at the calibration well. Log curves include the C and ϕ logs, along with the seismic traces at the well. Predicted values of H, C, and ϕ (black curves) correspond to the selected most likely combination of the three properties from the trivariate PDF (right). An iso-probability surface traces the combinations of H, C, and ϕ mapped at the 90th percentile of the posterior trivariate PDF. Multiple combinations of these three properties lie on this surface. A single combination is chosen randomly from the set. In this instance, the selected combination

consisted of values of $H = 15$ m, $C = 0.18$, and $\phi = 0.15$. If this selection process were repeated, a different combination would likely result each time. Although this combination was selected randomly, the iso-probability surface indicates that the inversion included the measured values in the results. Because of the many combinations of the reservoir properties occurring on the surface, the uncertainty of any one prediction increases.

The posterior bivariate and marginal PDFs are displayed in Figure 5.7 (bottom). On the left are H - C PDFs; the middle contains the H - ϕ PDFs; and the C - ϕ PDFs are on right. The bivariate PDFs that include a C term appear quite broad, meaning that for any value of H or ϕ, all possible values of C have a non-zero probability. The H - ϕ bivariate shows a trend similar to that seen in the inversion for just H and ϕ, but with more uncertainty, because the C component adds uncertainty. In addition, including the C parameter does not appear to improve the fit to the data.
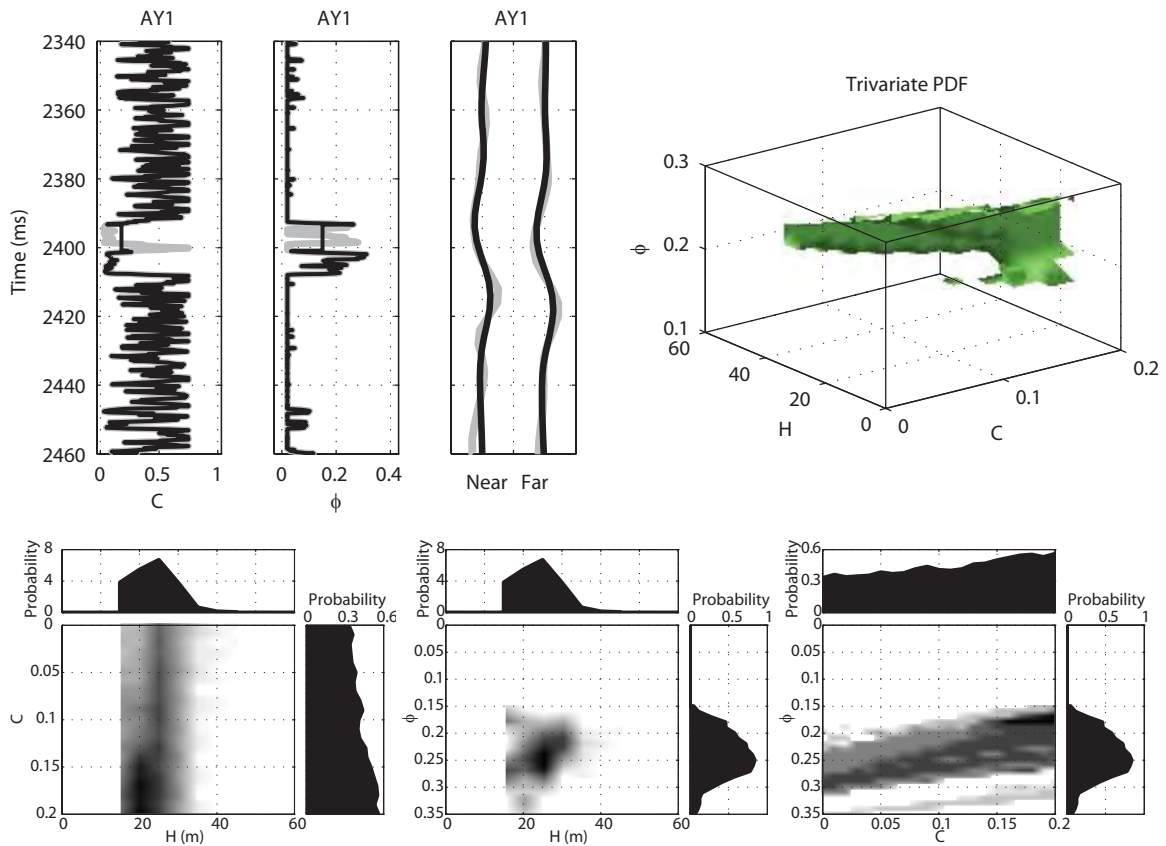
Figure 5.7. Measured and predicted log curves and posterior PDFs for thickness, clay content, and porosity at the AY1 well location. Even though the most likely values in the reservoir interval are inaccurate, the posterior PDFs show the relationship between thickness and porosity; however, the clay-content component does not provide any refinement of this relationship. It increases the uncertainty of the trend.

Next we show the measured and predicted values (top) at the three test-well locations and their respective trivariate PDFs (Figure 5.8). As in the predicted logs in Figure 5.7, the most likely H - C - ϕ combinations come from their individual trivariate PDFs. At the AK2 well, the inversion-based thickness was 35 m, approximately double the measured value of 18 m. In terms of rock properties, the inversion predicted C relatively well at 0%, with an underprediction of $\phi = 0.15$. Similar results are visible for the other two test wells. Iso-probability surfaces through 90th percentile of the trivariate PDFs for each case are noticeably different from one another. For the AK2 well, a trend is visible that shows a relationship for the three parameters similar to the one observed in Figure 5.7. For the AV1 well, a trend is also visible but for different ranges of H and ϕ. Lastly, the surface

for the AW1 well shows a broad range of H for low C, with a narrow range of H for high C.
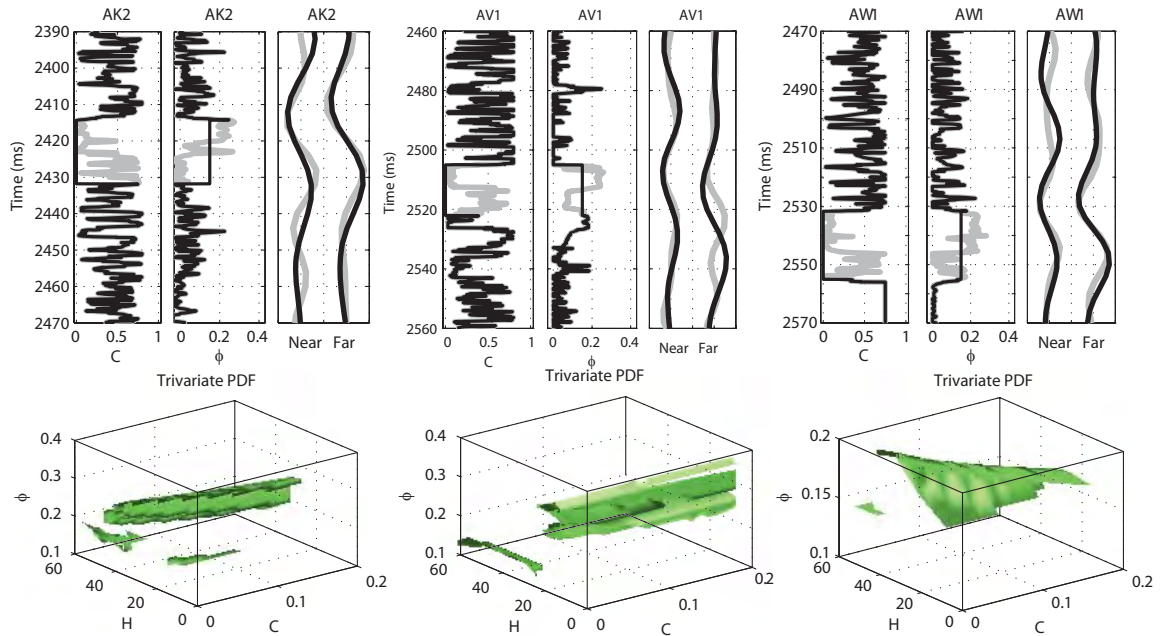
Figure 5.8. Log curves and posterior trivariate PDFs for the three test wells. In the AK2 well, the combination of most likely values lies close to the measured values. For the other two wells, the predictions are not as accurate.

Bivariate and marginal PDFs for three test wells are displayed in Figure 5.9. The top row shows the PDFs for H and C for each of the wells. The bivariates for all three wells indicate a relatively narrow range of H occurring for all values of C. In the middle row are the H and ϕ PDFs. The expected trend is visible for the AK2 and AV1 wells, although it is less distinct in the AV1 well. For the AV1 well (middle), the H marginal PDF is skewed to low values of H, indicating the prior range could be extended to smaller values. As in the previous inversion scenario, the H-ϕ trend is opposite in the AW1 well relative to the expected relationships. Last, on the bottom row are the C and ϕ PDFs. For the AK2 well, a distinct peak is present at low C and low ϕ, but many other values of the two properties could also occur. High ϕ values dominate the AV1 bivariate for all values of C. In the AW1 well, a nearly linear trend between C and ϕ is present. The trend shows that as porosity decreases, C gradually increases. The net result is a lowering of the impedance.
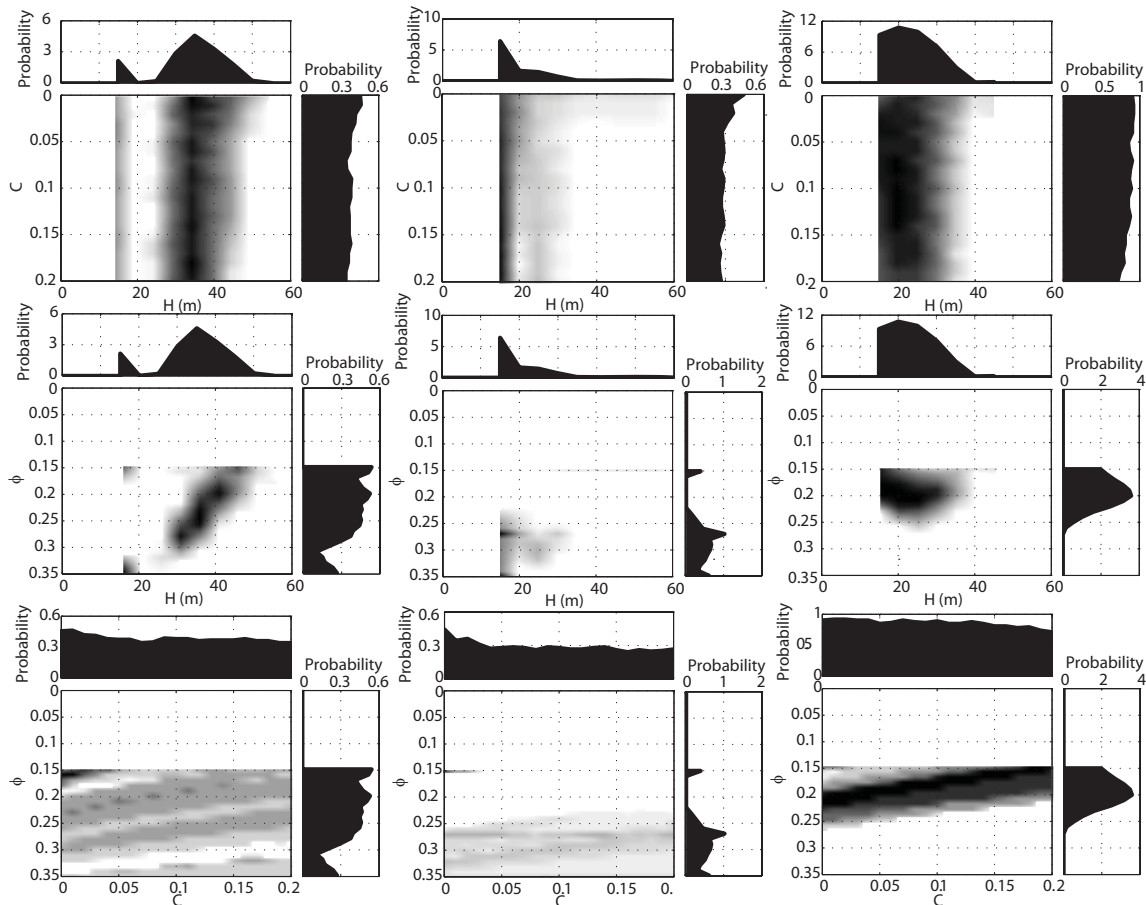
Figure 5.9. Posterior bivariate and marginal PDFs for the test wells. On the top row are the thickness and clay content PDFs; in the middle row are the thickness and porosity PDFs; clay content and porosity PDFs are in the bottom row. The expected thickness-porosity trend appears in the AK2 well, but it is not prevalent in the other two. The broad nature of the clay parameter indicates its weak influence on the seismic response.

The results at the four well locations demonstrated that the posterior PDFs were more uncertain when C was included with H and ϕ. To see how different the results can be throughout the data volume, maps of most likely values were generated. Figure 5.10 contains those maps for H, C, ϕ, and $H\phi$. The maps of H and ϕ differ noticeably from the maps generated in the two-parameter inversion. However, the $H\phi$ product map does not change much. This indicates that although including C increases uncertainty, the relationship between H and ϕ remains nearly constant.
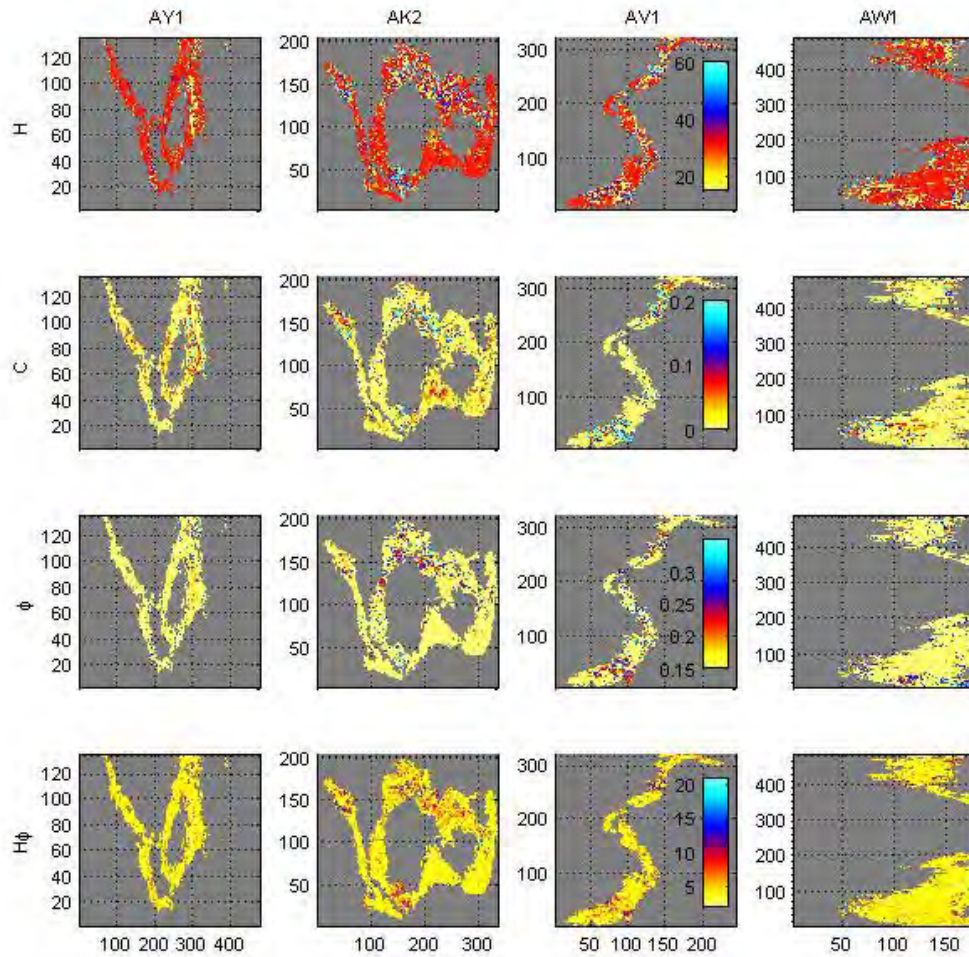
Figure 5.10. Maps of most likely reservoir properties. Combinations of the reservoir properties are drawn from the posterior trivariate PDFs at each trace location. The maps of thickness are noticeably different from those in Figure 5.5, but the porosity and thickness-porosity product maps are only slightly different.

The histograms of the reservoir properties for each geobody indicate more clearly the differences in results between the two- and three-parameter inversions (Figure 5.11). In all four geobodies, a thickness of 30 m is by far the most common. In Figure 5.6, this was the case for the AY1 and AK2 geobodies, but not for AV1 and AW1. In each geobody, the predominant C value is 0, whereas the most frequent ϕ value is 0.15. Thus, the prediction of ϕ and H times ϕ did not change significantly. This nearly constant value of the product of H and ϕ controls the seismic response because the reservoir thickness is below seismic resolution. However, this result will not occur in all instances.
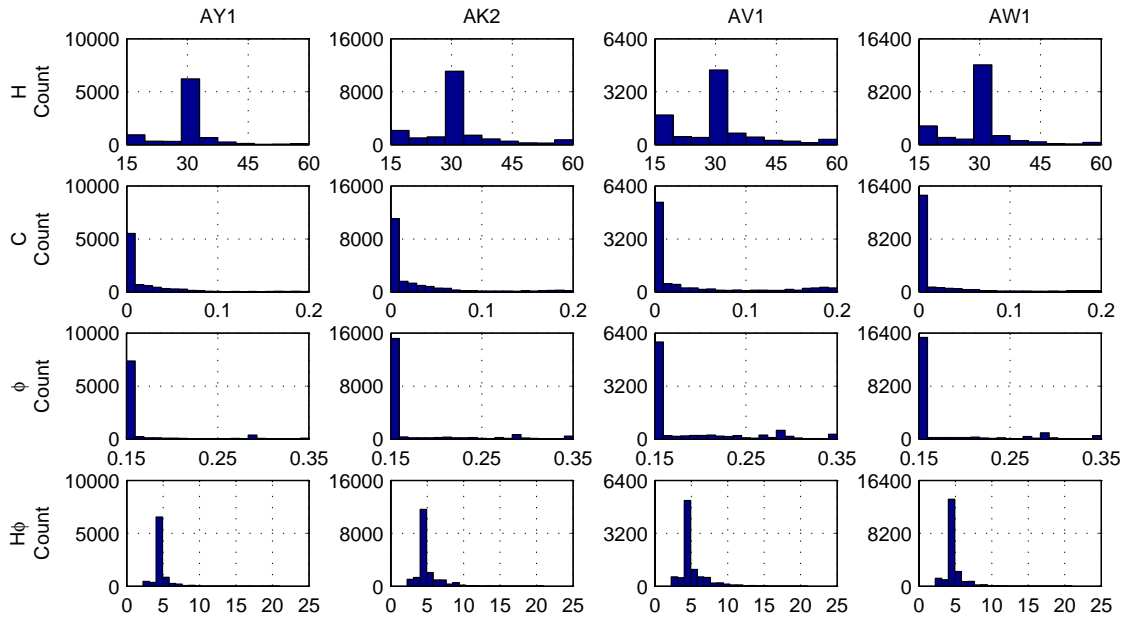
Figure 5.11. Histograms of the reservoir properties from the maps in Figure 5.10. These histograms illustrate the difference between the two- and three-parameter inversion scenarios.

5.5.3 Thickness-porosity-saturation inversion

This inversion scenario involves the simultaneous predictions of H, ϕ, and S_w with a constant C, written formally as $m = [H, \phi, S_w \,|\, C = 0.1]$, again with data $d = [A_N, A_F]$. For these inversion results, H was parameterized as 15 to 60 m with 5-m increment, ϕ from 0.15 to 0.35 with 0.01 increment, and S_w from 0.2 to 1.0 with 0.4 increment. The relatively large increment of 0.4 for S_w tests the inversion's ability to distinguish significantly different fluid conditions. The correlation threshold was set initially at 90% with an acceptance of 10% of the synthetic traces.

Figure 5.12 shows the predicted well-log results and posterior PDFs from the inversion at the calibration well. The mostly-likely H and ϕ values lie very close to the measured values, but predicted S_w equals 1. Despite the inaccurate saturation prediction, the measured and predicted seismic traces have a high correlation. The iso-probability surface of the trivariate PDF indicates that just a few values of H and ϕ are likely to occur, but any value of S_w is possible. Thus, drawing the most likely combination of these three properties includes accurate values of H and ϕ, with significant uncertainty for S_w.

The bivariate and marginal PDFs display more clearly the relationships in the trivariate PDF. The H and ϕ parameters have noticeable most likely values in nearly normally distributed forms. All values of S_w, however, occur with nearly equal probability in the H - S_w and ϕ - S_w bivariate PDFs, as well as in the S_w marginal PDF. Examining in more detail the H - ϕ bivariate, the expected trend is present. In addition, a second domain of non-zero probability exists at $\phi > 0.30$ for $H = 20$ m. This domain corresponds to the accepted synthetic traces with a high enough ϕ that when the pore fluid is brine, the corresponding seismic response is equivalent to that with lower ϕ in a gas-filled situation. Therefore, the inversion was able to discriminate between these two scenarios.
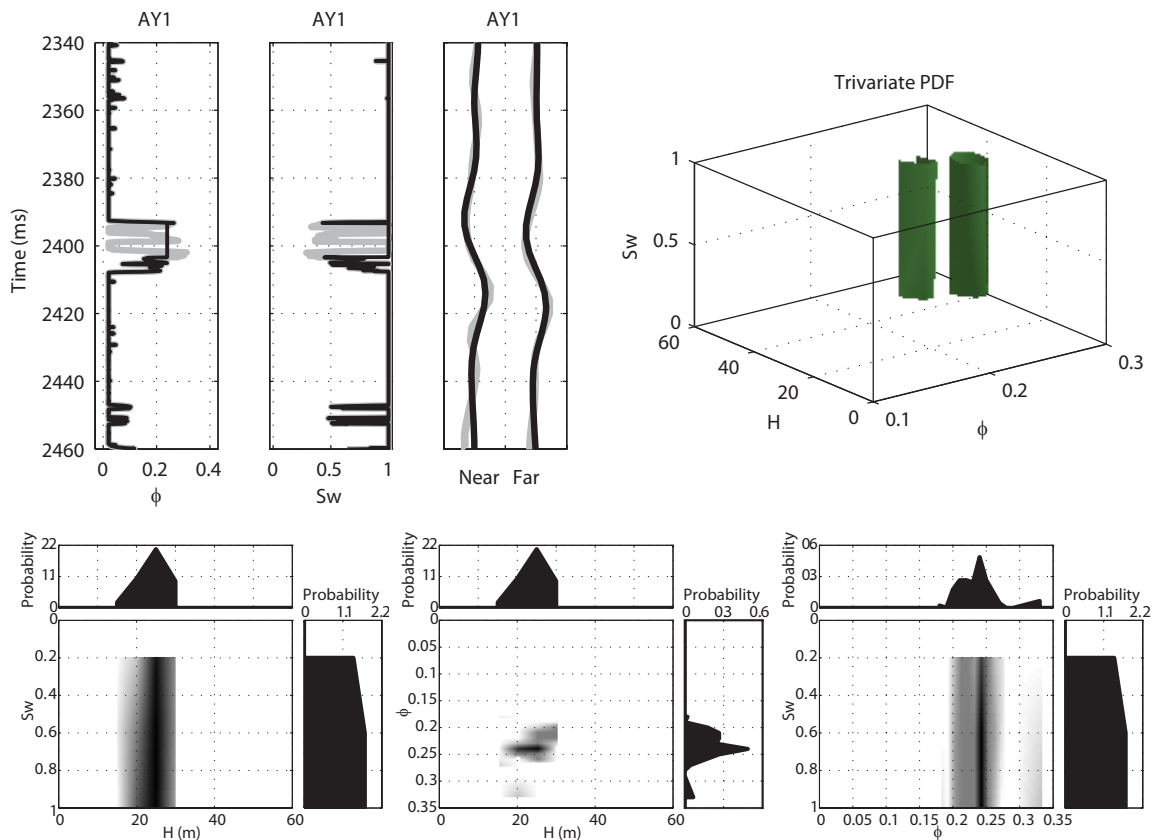
Figure 5.12. Predicted and measured well and seismic data and the posterior PDFs from the joint inversion of thickness, porosity, and saturation at the AY1 well. Predicted values of thickness and porosity are relatively accurate, but the saturation prediction is uncertain. However, the inversion separated high-porosity and high-saturation from slightly lower values of the two parameters.

Next we show the measured and predicted values at the three test-well locations and the trivariate PDFs from which the most likely combinations of H-ϕ-S_w were drawn (Figure 5.13). At the AK2 well location, H is significantly over-predicted, but both ϕ and S_w are quite accurate. The mismatch in the seismic is an indication of the poor match of thickness. The inversion predicts H and ϕ very accurately in the AV1 well, but like in the calibration well, it does not provide an accurate prediction of S_w. Regarding the AW1 well, both H and ϕ are accurately predicted by the inversion, but S_w is incorrect. Iso-probability surfaces through the 90th percentile of the trivariate PDFs for each well indicate relatively few values of H and ϕ have a high probability of occurring. However, in all three cases, the vertical orientation of the surfaces indicates that all values of S_w have a nearly equal probability of occurring. Therefore, the uncertainty for a particular S_w value is relatively high.
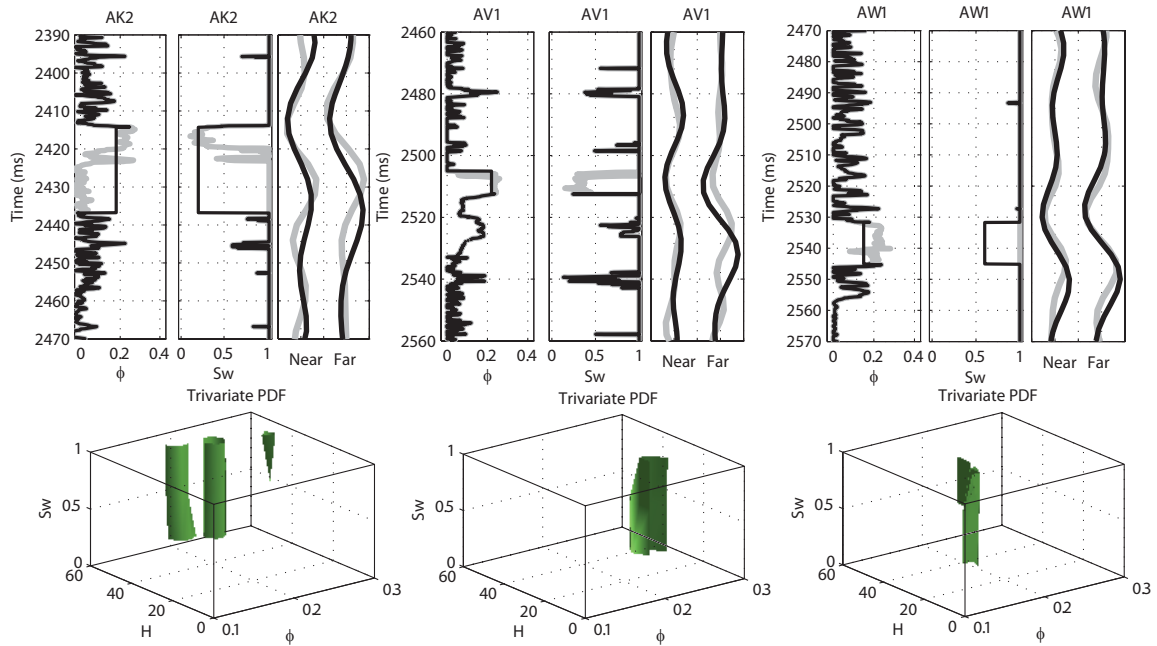
Figure 5.13. Results at the three test-well locations from the joint inversion of thickness, porosity, and saturation. Although porosity predictions are relatively accurate in each case, thickness is incorrect in the AK2 well, and saturation is incorrect in the AW1 well. The iso-probability surfaces are all oriented vertically, which indicates a weak dependence on saturation.

All the bivariate and marginal posterior PDFs for these three wells illustrate that narrow ranges of H occur for all values of S_w. (Figure 5.14, top row). However, for all

three wells, H predicted with ϕ results in a narrow range of combinations, although the form of the distributions varies from one well to another (middle row). Because results in all three wells show narrow ranges of H and ϕ occurring with high probability, this reaffirms that the combination of these two parameters is the dominant factor determining the seismic response. Varying saturation does not significantly change the seismic response. However, this inversion scenario includes the first variation of S_w. Without including this, we should not anticipate an accurate prediction of the data in the AW1 well. Furthermore, the ϕ-S_w bivariate PDFs for the AK2 and AV1 wells are multi-modal, where the higher-porosity regions correspond to $S_w = 1$ conditions. This multi-modality does not occur in the ϕ-S_w bivariate for the AW1 well.
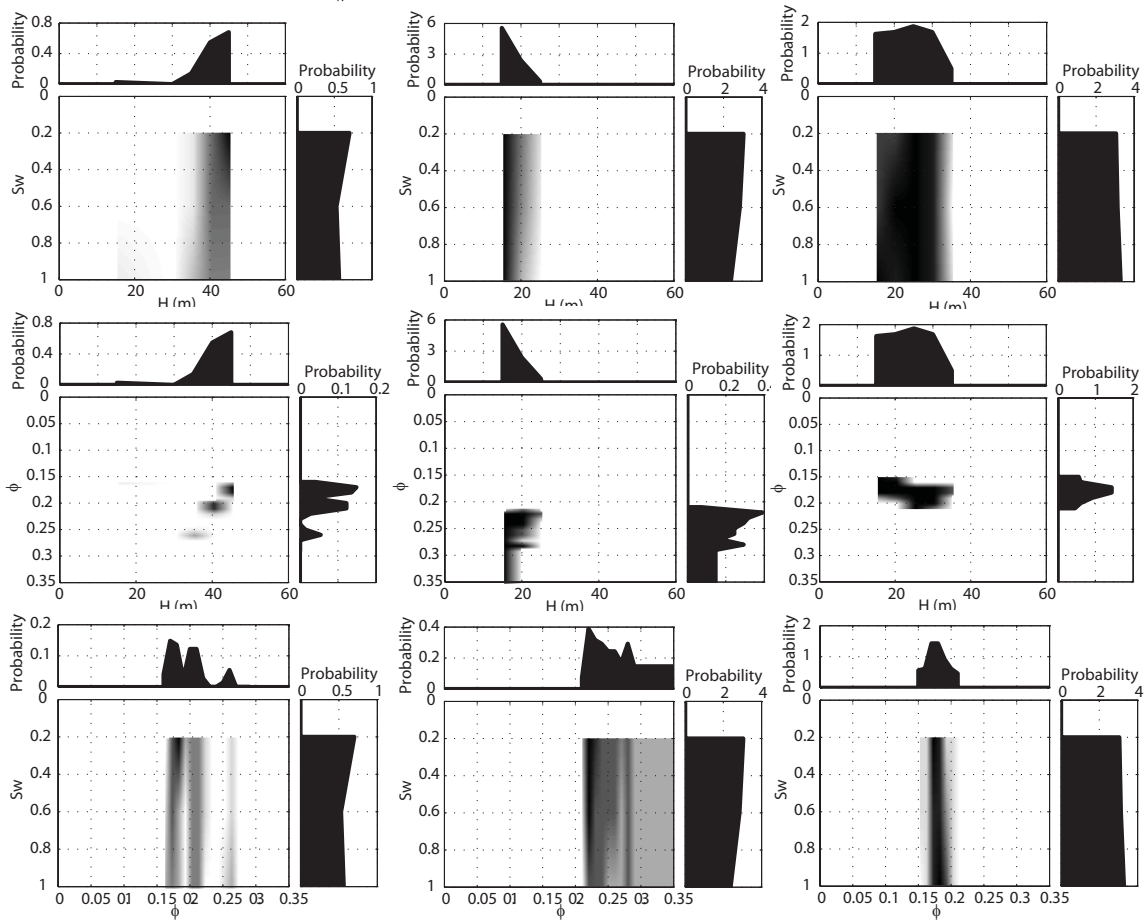
Figure 5.14. Bivariate and marginal PDFs for the test wells. The left column corresponds to the AK2 well; the middle to the AV1; and the right to the AW1 well. The saturation components force the bivariate PDFs that contain this component to be broad and uncertain. In all three cases, narrow ranges of thickness and porosity are compounded by the saturation term.

By including S_w in the inversion, we introduce more synthetic traces into the comparison step that are quite similar to each other, given that S_w does not significantly alter the seismic response. Accordingly, the maps of H and ϕ should change because of increased uncertainty (Figure 5.15). The predictions of H and ϕ indeed change relative to the set of maps from H - C - ϕ the inversion (Figure 5.10), but the product of them does not change significantly. In comparison to the maps from the H - ϕ inversion, all sets of maps are quite similar. Histograms of the reservoir-property maps display this information more clearly than do the maps (Figure 5.16).
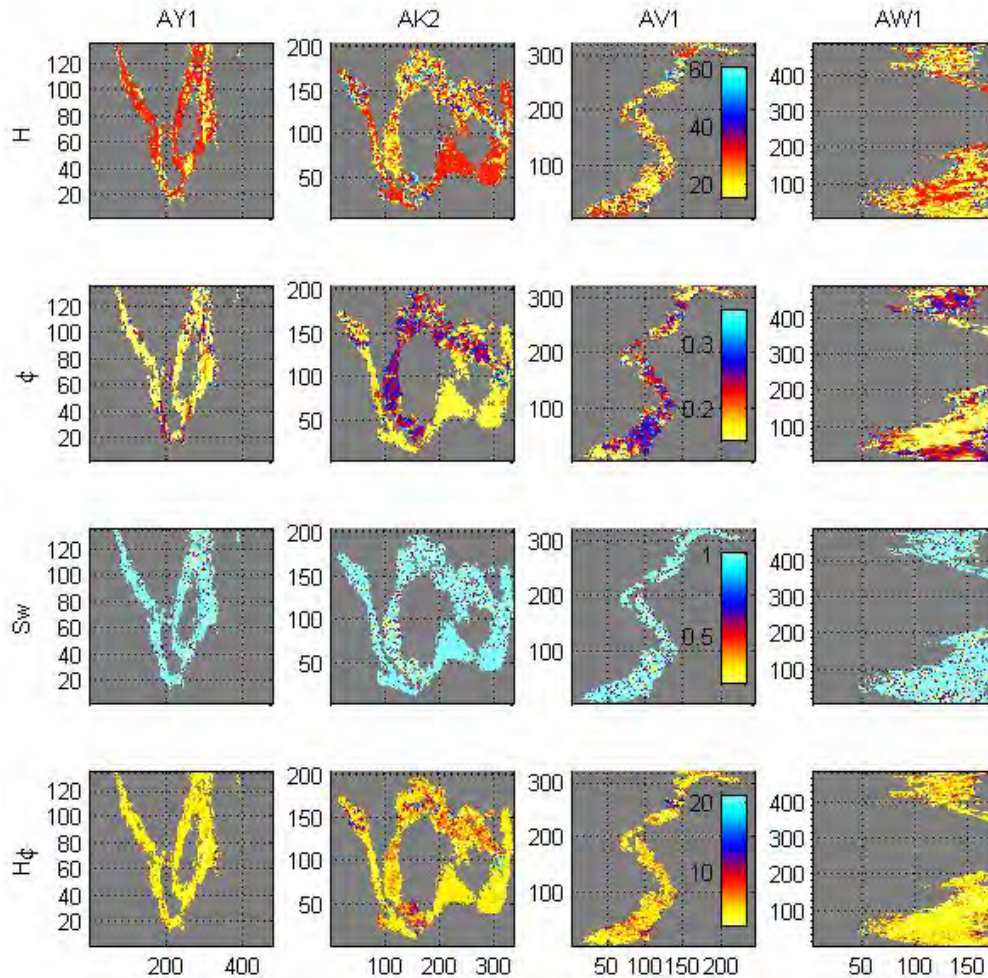
Figure 5.15. Maps of most likely values of thickness (top), porosity (second row), saturation (third), and the product of thickness and porosity (bottom). The relationship between thickness and porosity becomes quite evident, particularly in the AK2 and AV1 geobodies. Saturation appears to be predicted incorrectly in the three geobodies on the left, which suggests that the inversion is insensitive to fluid saturations.
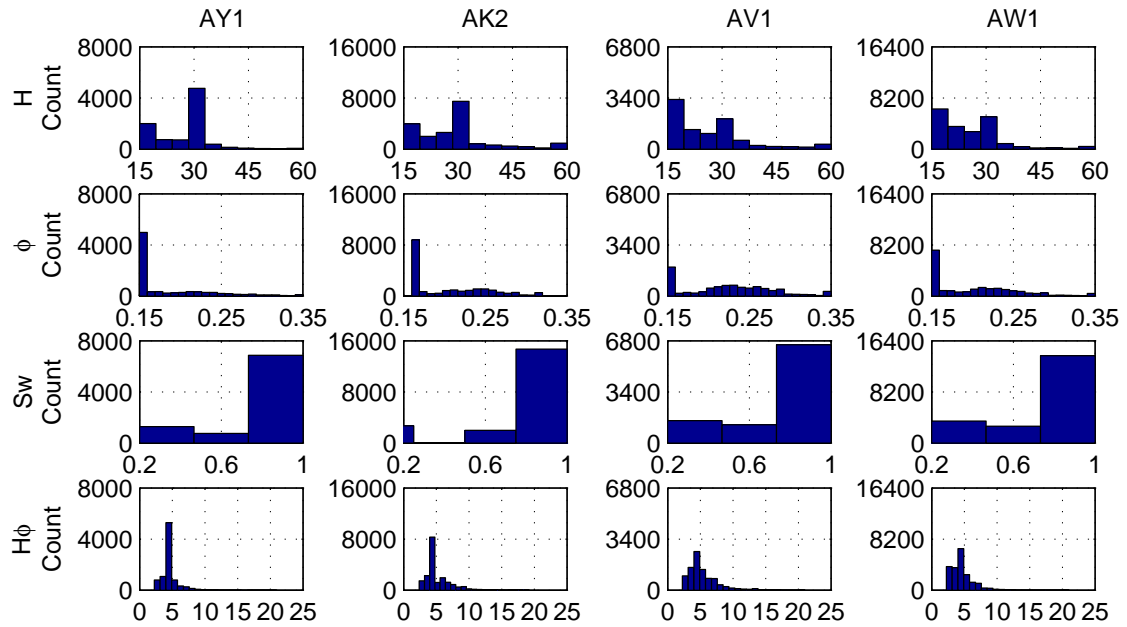
Figure 5.16. Histograms for the geobodies in Figure 5.15. The thickness is predicted to be 30 m in the AY1 and AK2 wells, with some smaller values. In the AV1 and AW1 wells, the dominant thickness is 1 m. In each case, the most common value of porosity is 0.15. Saturation, clearly seen in the map view, is mostly at full-brine saturation. In all four geobodies, at value of 4.4 porosity-m is the most common value.

5.5.4 Thickness-clay content-porosity-saturation

The final set of results comes from the inversion of the seismic data for all four reservoir parameters. In this case, the modeled parameters are $m = [H, C, \phi, S_w]$ with data $d = [A_N, A_F]$. Ranges used for the parameters were 15-60 m for H, 0-0.20 for C, 0.15-0.35 for ϕ, and 0.2-1.0 for S_w. Increments used were 5 m for H, 0.01 for C and ϕ, and 0.1 for S_w. These prior distributions resulted in 39690 earth and seismic models. The inversion parameters, calibrated at the AY1 well, were to accept 10% of the total traces with an initial 70% threshold.

Results at the AY1 well are displayed in Figure 5.17. Included are the measured logs and seismic data along with the best-match synthetic data. The reservoir property values were drawn from the full 4-D conditional posterior distribution, which is not displayed because of its dimensionality. On the right are the four 90th perecentile iso-probability surfaces from the respective posterior trivariate PDFs. The H - C - ϕ trivariate resembles

that obtained in the inversion for just H, C, and ϕ (Figure 5.7). The other trivariate PDF that contains useful statistical information is the H-ϕ-S_w trivariate PDF. Although all the surface contains all values of S_w, at $S_w = 1$, the H-ϕ combination is pushed to higher ϕ relative to where $S_w < 1$. The H-C-ϕ surface traces out all values of C and S_w for a relatively narrow H range. Similarly, all values of C and S_w lie on the C-ϕ-S_w surface for a narrow range of ϕ.
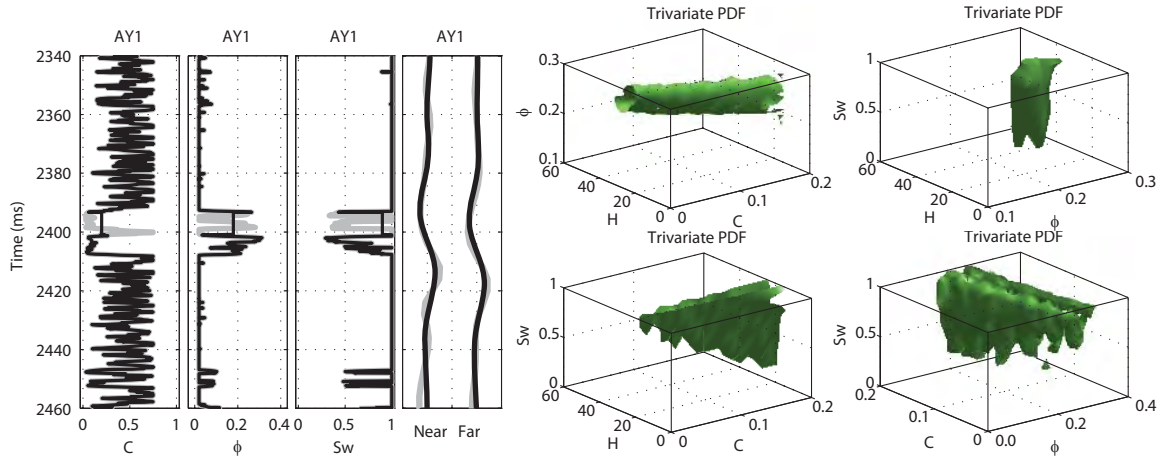
Figure 5.17. Well and seismic and iso-probability surfaces from the four trivariate PDFs at the AY1 well location. The surfaces indicate that the combination of thickness, porosity, and saturation provides valuable information in terms of predicting reservoir properties.

Although the isosurfaces through the trivariate PDFs do not explicitly show how the four reservoir parameters combine in the full 4-D conditional posterior distribution they do indicate some of the behavior of 4-D conditional PDF. In particular, H and ϕ have narrow ranges of high-probability values, whereas, C and S_w have very wide ranges of likely values. When the most likely combination of the four parameters is selected, multiple combinations can be chosen as the most likely to occur. This is evident in the appearances of any of the posterior PDFs that contain a C or S_w term. The predicted values of the reservoir properties in Figure 5.17 were selected from the 4-D conditional posterior distribution. As such, the uncertainty of this prediction is greater than the uncertainty present if just H and ϕ were considered, because the posterior values of C and S_w span their entire prior ranges.

The six posterior bivariate and four marginal distributions are displayed in Figure 5.18. The combinations of two properties taken two at a time are H-C, H-ϕ, H-S_w, C-ϕ, ϕ-S_w, and C-S_w. The top row consists of the three bivariates that include H. The H-C bivariate shows a relatively narrow range of H, also evident in its marginal PDF, but C varies across its whole prior range. H and ϕ combine in a narrow range around the measured values. This demonstrates the expected relationship between them. The bivariate PDF with H and S_w resembles that of H and C. A nearly linear relationship exists between C and ϕ (bottom left), in which the highest probability occurs where higher C makes the modeled reservoir less stiff. The bivariate between ϕ and S_w is interesting in that two different domains exist. The overall range of ϕ values in the marginal defines all possible ϕ values. S_w separates that range into two domains. The first occurs for S_w between 0.2 and 0.9 for a range of ϕ between 0.16 and 0.26. The other domain is for a $S_w = 1$ with a corresponding ϕ range of 0.22 to 0.35. The two domains, however, have a similar probability of occurring. Lastly, the bivariate between C and S_w indicates that all combinations have a non-zero probability, with the most likely occurring at $C = 0.2$ and $S_w = 0.9$.
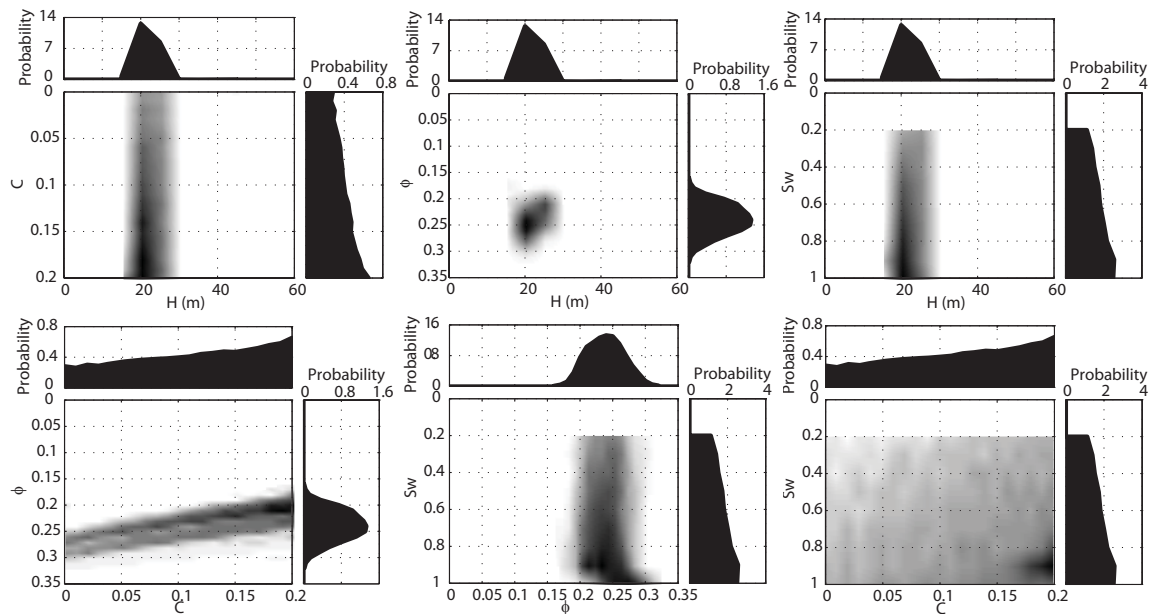
Figure 5.18. Posterior bivariate and marginal PDFs at the AY1 well location. Thickness and porosity are accurately predicted. Porosity and saturation combine in a way that can distinguish brine sands from gas sands, depending on their porosities.

Figure 5.19 exhibits the inversion results at the AK2 well location. In this instance, the predicted H, C, and ϕ values fall quite close to the measured values, but the S_w prediction is not accurate. The iso-probability surfaces from the posterior trivariate indicate relatively narrow ranges for H and ϕ, but broad ranges of C and S_w. Each surface resembles its counterpart from the AY1 well. Limited combinations of H and ϕ are integrated over the C and S_w parameters. Moreover, the full 4-D conditional PDF inherently contains this uncertainty that the four trivariate PDFs illustrate. Although the predicted values taken from the 4-D posterior PDF are accurate, their uncertainty is quite high. Thus the random selection of a combination of reservoir properties was relatively fortuitous.
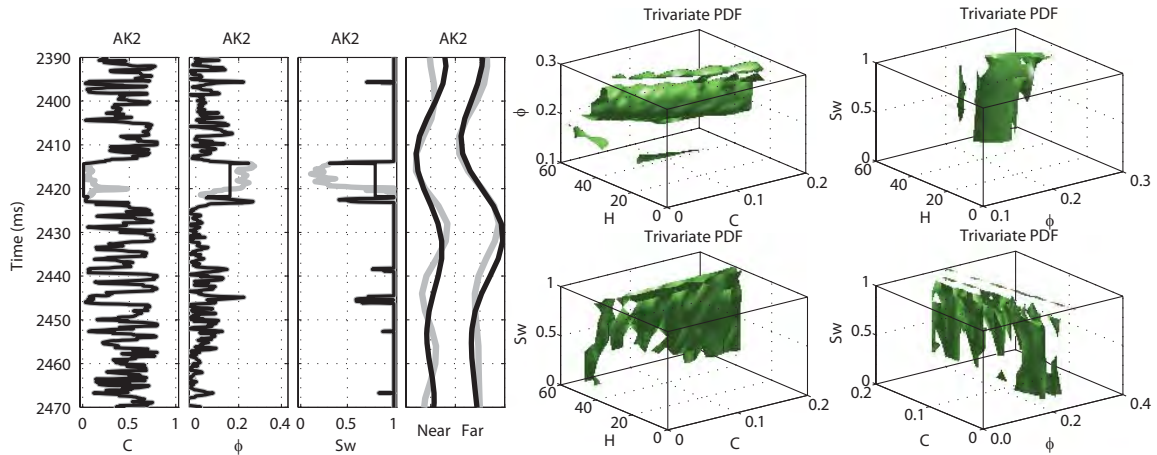
Figure 5.19. Predictions for the AK2 are quite accurate except for saturation. The clay content and saturation components increase the uncertainty of the predictions due to their posterior values spanning their respective prior ranges.

The six bivariate PDFs at the AK2 well are displayed in Figure 5.20. As in the AY1 well, the H-C and H-S_w bivariate PDFs show a relatively narrow range of H, but C and S_w span their prior ranges. The joint PDF between H and ϕ demonstrates the commonly observed trend between these parameters. A nearly linear relationship exists between C and ϕ (bottom left), with the peak skewed to low C and low ϕ. In the ϕ-S_w bivariate PDF, the distinction between high ϕ and high S_w and lower ϕ with low S_w is apparent. Last, the C and S_w parameters combine to give nearly uniform results.
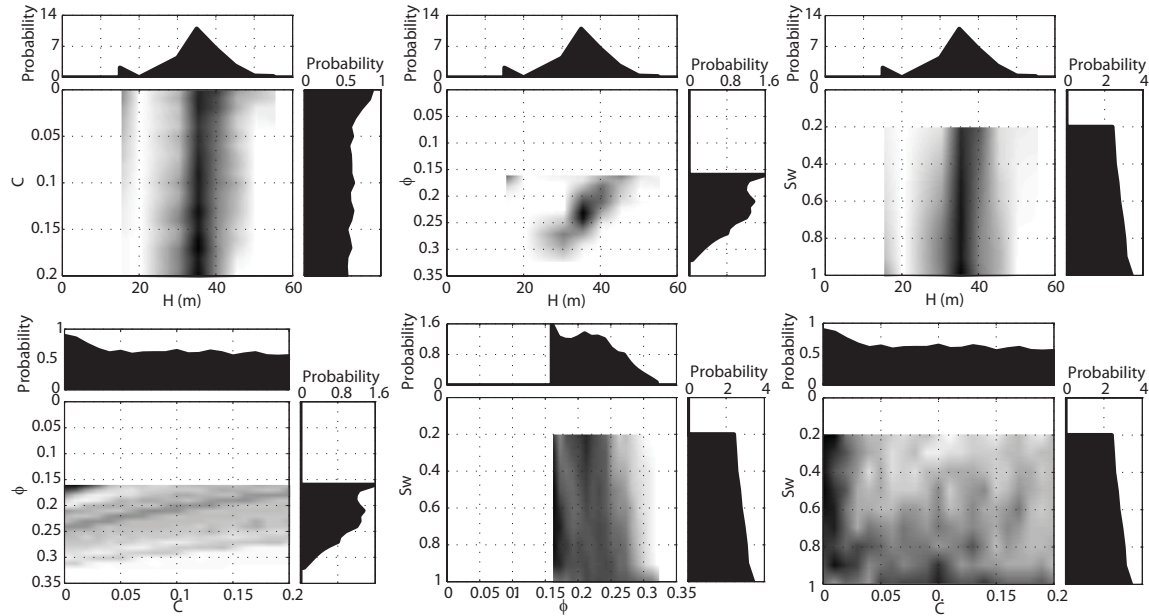
Figure 5.20. The posterior bivariate and marginal PDFs at the AK2 well show results similar to those at the AY1 well. However, larger thicknesses and smaller porosities are predicted along with the wide ranges of clay content and saturation.

Predicted and measured log curves for the AV1 well and the iso-probability surfaces from the posterior trivariate PDFs are displayed in Figure 5.21. The predicted log curves show an overprediction of H by a factor of more than 2, a fairly accurate C prediction, an underestimate of ϕ, and an incorrect S_w. The surfaces through the trivariate PDFs indicate the degree of uncertainty that accompanies these predictions. This degree is similar to that observed in the AY1 and AK2 wells.
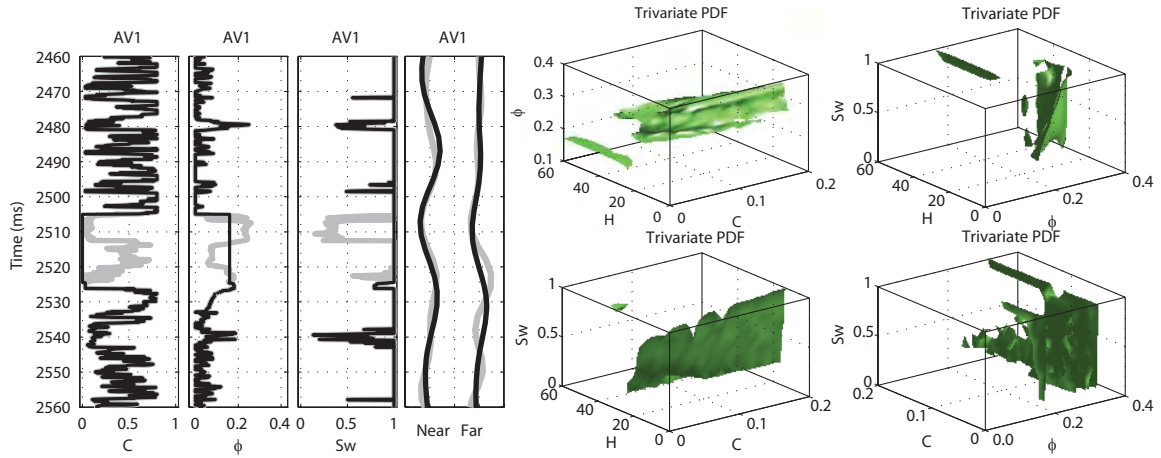
Figure 5.21. Reservoir-property predictions at the AV1 well include an over-estimate of thickness by a factor of two, an under-estimate of porosity, and a prediction of full brine saturation. The iso-probability surfaces resemble those observed in the AY1 and AK2 wells.

Posterior bivariate and marginal PDFs at the AV1 well location are displayed in Figure 5.22. In general these PDFs show that a small H and relatively high ϕ ranges are present and accompanied by broad ranges of C and S_w. The commonly observed trend between H and ϕ is present, but the uncertainty around it is quite high.
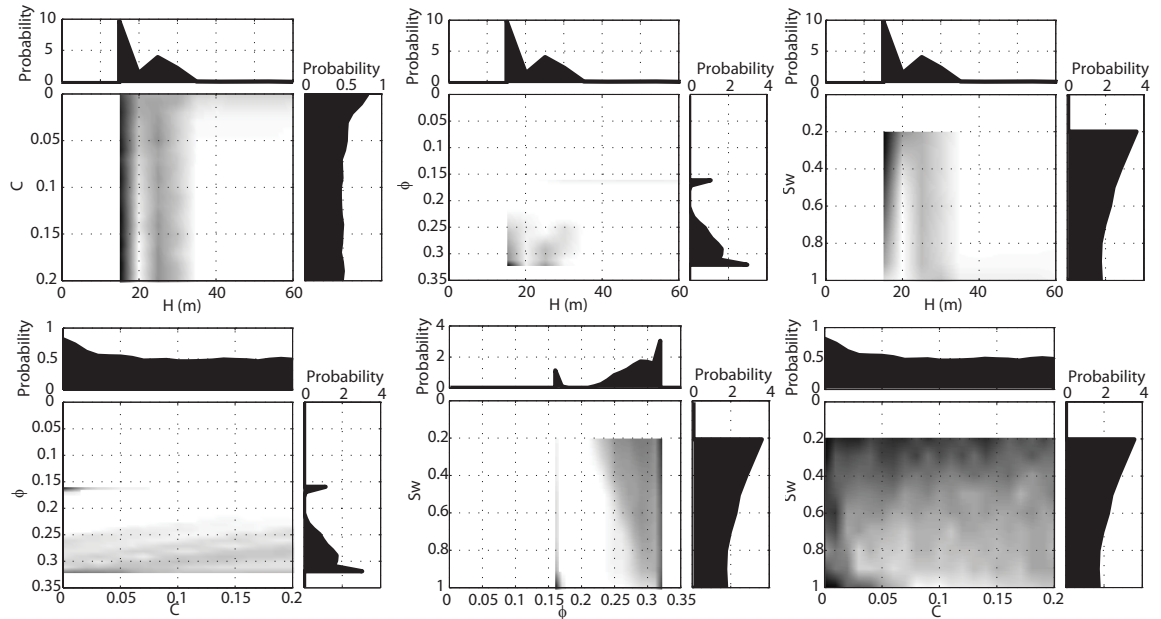
Figure 5.22. Posterior bivariate and marginal PDFs at the AV1 well location. Narrow ranges of thickness and porosity occur with broad ranges of clay content and saturation.

The final set of results at an individual well location is for the AW1 well (Figure 5.23). The display of the log curves and iso-probabilty surfaces is the same as those for the previous three wells. The predicted value of H is greater than the measured value; C is predicted accurately; ϕ is slightly under predicted; and S_w is predicted correctly. In the H - C - ϕ surface, the continuity of the H - ϕ relationship along the C axis is evident. In H - C - S_w space, this continuity occurs in both the C and S_w directions. Two domains are present in the H - ϕ - S_w trivariate PDF, where for S_w to equal 1, H and ϕ must combine in a way that makes the reservoir sand look less stiff to the seismic wave. In the C - ϕ - S_w space, the C term increases the range of highly probable combinations.
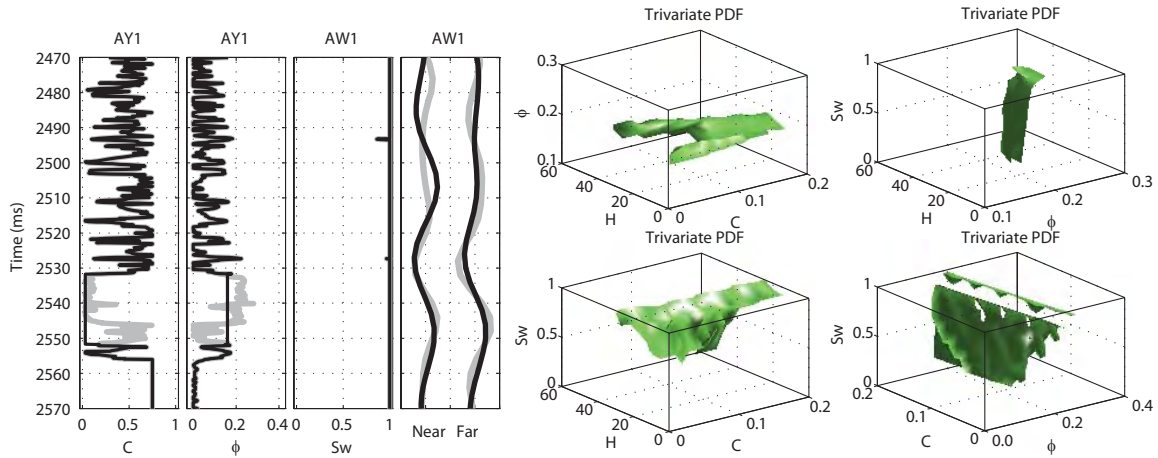
Figure 5.23. Well and seismic data and iso-probability surfaces from the posterior trivariate PDFs at the AW1 well. The well curves show fairly accurate results for the reservoir properties. A distinction can be made between gas and brine sands depending thickness and porosity combinations.

Examining the six posterior bivariate PDFs reveals similarities between them and those in the AY1 wells (Figure 5.24). The narrow ranges of H and ϕ are made uncertain by the wide ranges of C and S_w. However, the H - ϕ bivariate shows the limited number of combinations of these two parameters that have a non-zero probability. For C and ϕ, a nearly linear trend exists, so a C value with high probability could be determined for a given ϕ value. As in the AY1 well, two domains exist in the ϕ - S_w bivariate PDF, which was also the case in the H - ϕ - S_w trivariate isosurface. One is for S_w <1 for ϕ between

0.18 and 0.22. The other is for $S_w = 1$ and ϕ between 0.22 and 0.32. The $C\text{-}S_w$ bivariate PDF appears nearly uniform except for the peak at $S_w = 1$.
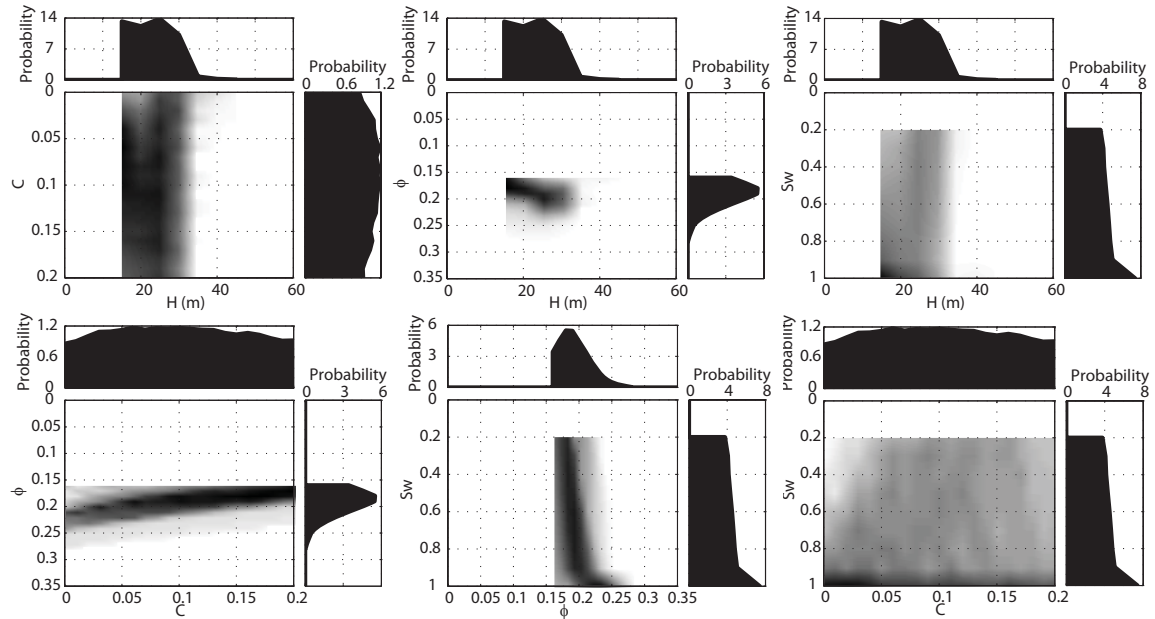
Figure 5.24. Posterior bivariate and marginal PDFs at the AW1 well location. The most distinct relationships occur between thickness and porosity and porosity and saturation.

In Figure 5.25, we show the map views of the four reservoir properties and product of H and ϕ mapped onto the geobodies. Maps of H, ϕ, and $H\text{-}\phi$ resemble most closely those from the $H\text{-}C\text{-}\phi$ inversion. This was expected because of the common C component. The histograms indicate that the prediction of C is more evenly distributed in the four-parameter inversion than in the $H\text{-}C\text{-}\phi$ inversion.
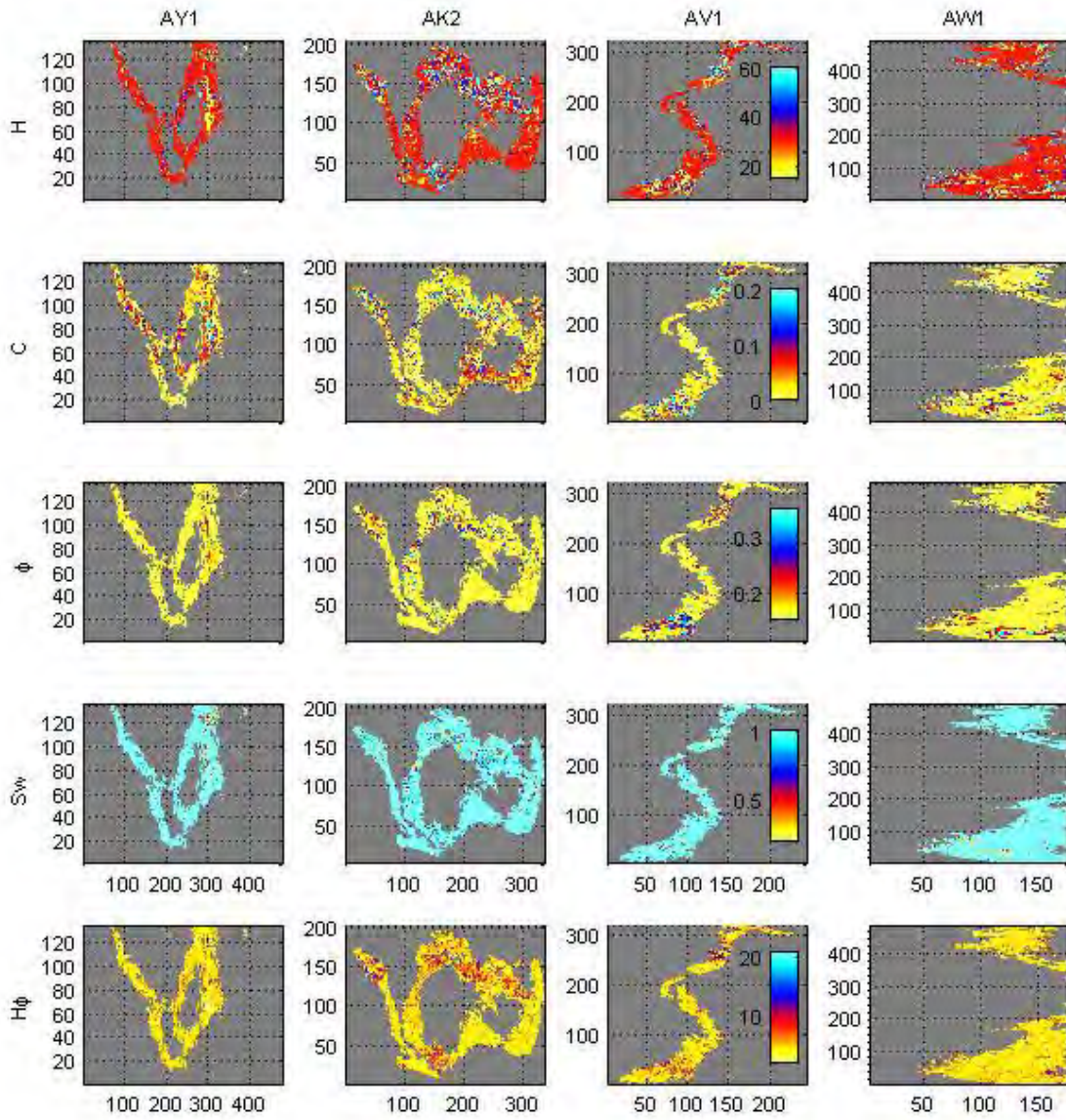
Figure 5.25. Maps of the most likely reservoir properties resulting from the simultaneous inversion of thickness, clay content, porosity, and saturation. The maps resemble those from the inversion of thickness, clay content, and porosity.
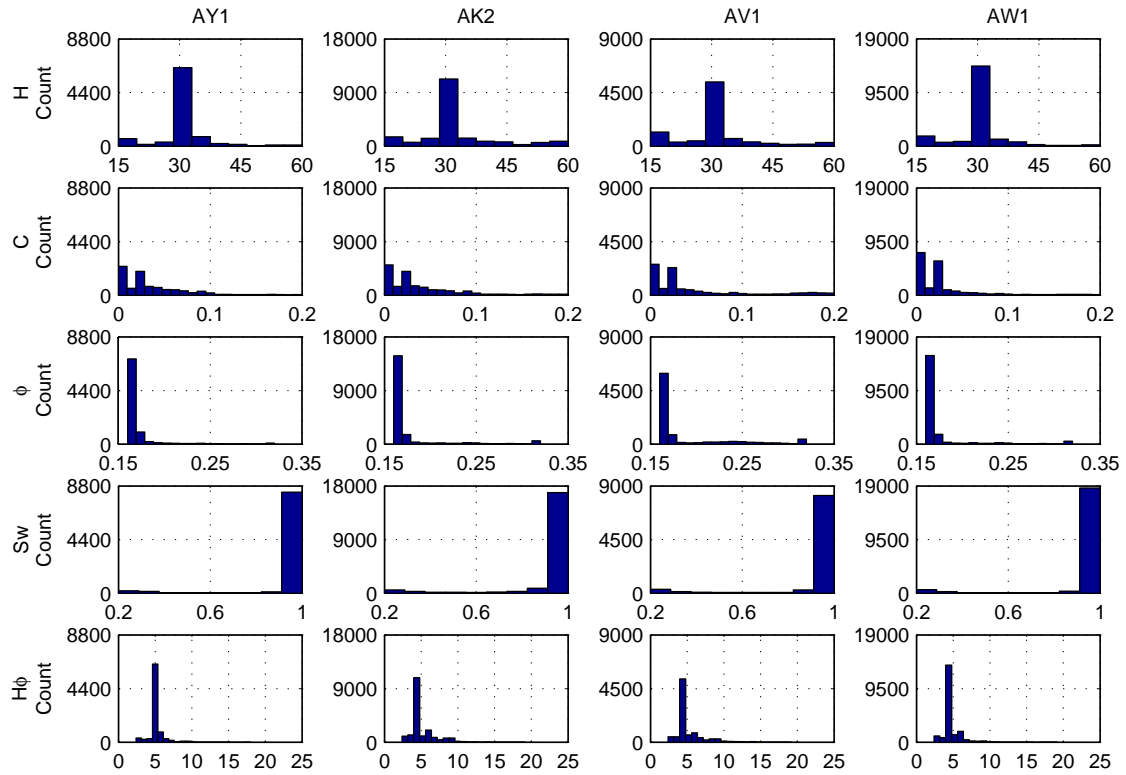
Figure 5.26. Histograms of the reservoir properties show that a dominant thickness of 30 m exists in all the geobodies. Clay content is evenly distributed across its prior range. Porosity, saturation, and thickness-porosity values all resemble those obtained from the inversion of thickness, porosity, and saturation.

5.6 Discussion

The purpose of varying the model parameters from two to three to four was to examine how the accuracy and uncertainty of the inversion results change as the problem becomes increasingly under-determined. By inverting for only H and ϕ in the first scenario, we explored how the inversion operates when only the two most significant reservoir properties are included. The success of the predictions at the different well locations varied somewhat. As expected, the most likely values of H and ϕ in the AY1 well matched the real data very well (Figure 5.3). In the other three wells, the most likely values of H overestimated the measured value, whereas ϕ was quite accurate or slightly underestimated (Figure 5.4).

In reference to the posterior bivariate PDFs (Figures 5.3 and 5.4), the trade-off exists between H and ϕ in the AY1, AK2, and AV1 wells. Among these three wells, this

relationship was most correct at the AY1 well, given the inversion was calibrated using its data. At the AK2 well, the relationship holds, but it occurs at greater H values and slightly lower ϕ values than in the AY1 well. As for the AV1 well, the H values are about the same as in the AY1 well, but the predicted ϕ values are noticeably higher than in the calibration well. A somewhat different result occurs in AW1, in which a trend is present, but with the opposite orientation of those observed in the three other wells. This was the only wet well, so it is interesting that a difference between H and ϕ appears from the inversion. However, it should be noted that assigned saturation value was 0.3. Therefore, we did not include in the inversion the in-situ conditions at this well. Based on this, we cannot definitively say that this different relationship indicates saturation differences. In all the cases, the inversion is capable of predicting the combination of H and ϕ but not of finding reliable independent predictions of the two properties.

In terms of the maps and histograms of the most likely values, we surmise that the selection of the most likely combination of H and ϕ at every location on the AY1 geobody contains approximately the same degree of uncertainty the bivariate PDF at the well location (Figures 5.5 and 5.6). We claim this, although we did not visually examine the posterior for each trace. These statements hold true for the other three geobodies, in which the degree of uncertainty at each trace is likely very similar to the uncertainty observed at the nearest well location. Overall, the degree of uncertainty did not vary significantly from well to well, but the accuracy of predictions may be in question, particularly for the geobodies corresponding to the AK2 well.

When we include C in the inversion parameters with H and ϕ, the uncertainty in all predictions increases significantly. In the AY1 calibration well, where the inversion should produce accurate results, we see that none of the most likely values correspond to the measured values of H, C, or ϕ (Figure 5.7). The continuity of the trivariate PDF in the direction of the C component explains this. The bivariate PDF between H and ϕ contains the expected relationship between them (Figure 5.8), but the C parameter introduces a very significant amount of uncertainty into this trend. As a result, the most likely values are inaccurate and uncertain. However, if the inversion were performed

again, the most likely values would change due to the random selection of a different most likely combination.

In the other wells, the C parameter again forces the uncertainty upwards in terms of the predictions of any of the three properties. Although predicted values in the AK2 well appear accurate, they are indeed uncertain (Figure 5.8). For the AV1 and AW1 wells, significant over-predictions of H couple with low estimates of ϕ. The trend between the two properties, therefore, appears to work in the AV1 well, but the opposite trend in the AW1 well suggests that the result is highly uncertain. The bivariate posterior PDFs for three test wells resemble those obtained in the H-ϕ inversion, albeit with the C parameter inducing uncertainty (Figure 5.9).

Arguably the most interesting result that came from this study is the separation of the saturation values depending on H-ϕ relationships. This was seen in both the H-ϕ-S_w and H-C-ϕ-S_w inversion results. From a rock-physics standpoint, this result is expected. As porosity increases, even in a stiff rock, a stiffer pore fluid can enter the pore space to give the same same elastic and/or seismic response as a stiffer frame with a less-stiff fluid. This concept is understood, predictable, and has been observed many times in previous studies, particularly at the well-log scale. However, the algorithm used in this study provided the ability to calculate probabilities corresponding to the two different saturations. Although the results showed that equal probabilities occurred for the two domains, obtaining this relationship was unexpected given the stiff nature of the reservoir rocks under examination. The separation of the domains does not appear clearly at all the well locations. Nonetheless, the ability to detect these two domains in some locations indicates that at least three parameters (H, ϕ, and S_w) should be included in the inversion.

The H-C-ϕ inversion results demonstrated that C was the most uncertain parameter. However, we could still obtain the H-ϕ-S_w effect from the four-parameter inversion. This result is quite encouraging in that the extremely uncertain C component does not overwhelm this relationship. Although the H-ϕ trend did not always predict the

values extremely accurately in the AK2 and AV1 well locations, the trend was still present, and the S_w component could be obtained from the posterior results.

5.7 Conclusions

Several conclusions can be drawn from this study. First, lithology cannot be accurately predicted from this seismic dataset, largely because of the lack of wide-incidence-angle seismic data. Additional information would have to be included to obtain a lithology estimate. The rock physics also helps to explain this. For high ϕ, C has little effect on the impedance. Therefore, it could have been eliminated from the inversion to reduce computational demands.

Second, a reliable H-ϕ relationship can be detected at the gas-well locations. Even though the posterior PDFs were not visually examined at all trace locations, the results at the wet well suggest that if an oppositely oriented H-ϕ relationship exists, then the corresponding potential reservoir unit may contain brine. All the results showed how uncertain an S_w prediction can be, even at a location where brine is known to exist. As a result, we may not be able to predict S_w accurately or separate commercial from non-commercial gas pay, but we can examine the probabilities associated with H-ϕ-S_w combinations that may contribute to the measured seismic response. Importantly, we could not have observed a saturation effect without including both H and ϕ. A joint ϕ-S_w inversion may have pointed out this relationship, but without the geometric parameter, it would have been incomplete. In addition, without ϕ, a H-S_w inversion would not have been informative. Thus, we conclude that H and ϕ must be included in the inversion of this dataset. Only with those two parameters included in the inversion can S_w saturation effects be analyzed.

From a commercial standpoint, it should be pointed out that all wells in the seismic volume were drilled based on the class III AVO anomalies. Although we cannot say that use of this inversion method for evaluation purposes would have successfully predicted water in the AW1 successfully, examining the posterior probabilities would certainly have quantified the possibility and presence of water in this well.

More generally, the goal of this work was to examine how the uncertainty changes as we attempt to calculate more unknown quantities from a limited number of inputs. This inversion algorithm provided the ability to do that. However, if uncertainty in the results becomes too significant, then discriminating between statistical noise and reservoir heterogeneity becomes quite difficult, if not impossible. Furthermore, no matter how good the data processing is for a given seismic dataset, uncertainty still remains in the translation from elastic to reservoir properties. Within the assumptions of the inversion algorithm, we can quantify the probabilities of combinations of reservoir properties that may underlie the measured seismic response

5.7 ACKNOWLEDGEMENTS

Chapter 6
From seismic traces to reservoir properties: Physics-driven inversion

"Always listen to experts. They'll tell you what can't be done, and why. Then do it."

--Robert A. Heinlein

6.1 Introduction

Forward modeling and inversion are commonly used tools to translate seismic traces into elastic earth properties. Comparisons of real and multiple iterations of synthetic seismic data, the latter computed from initial and perturbed models of elastic properties, provide this translation. The final earth model, the one corresponding to the best match between the real and synthetic seismic data, represents a possible spatial distribution of independent elastic constants such as P-wave impedance (I_p) and Poisson's ratio (ν). Although these maps of elastic properties are meaningful to geophysicists, they fail to supply necessary information to engineers who require lithology, fluid, and porosity, i.e., bulk property maps and *in situ* conditions.

Rock physics provides transforms that link the elastic properties to these bulk properties and conditions. However, scaling differences between the rock-physics domain and the seismic domain prevent accurate applications of these transforms. The reason is

that rock-physics transforms operate on a point-by-point basis at the centimeter scale, assuming spatial stationarity of rock properties. Seismic radiation, on the other hand, functions on a scale of tens or hundreds of meters. Therefore, applying these transforms at the seismic scale often violates the stationarity assumption.

This multi-scale problem is not only difficult to solve but also difficult to pose. For example, what is the relationship between porosity and impedance? Is the correct porosity the spatially averaged porosity of sandy shale, the "smeared" porosity of the sand, or the integral of the sand porosity with respect to depth, inline, and cross-line distance (e.g., the product of porosity and thickness)? To avoid these questions, one may consider "model-driven" inversion, termed here "physics-driven" inversion. Instead of constructing an elastic earth model, we construct a multiple lithology/fluid/porosity model at the natural scale of a rock-physics transform (e.g., the well-log scale). This transform converts these lithology/fluid/porosity models at each point in space into elastic models. Then synthetic traces generated from the elastic models can be compared with real data until a match is found. The result is a map of the bulk properties and conditions.

This type of physics-driven inversion naturally eliminates physically unrealistic elastic-constant combinations. However, its disadvantage is its inherent non-uniqueness, in which a function of more than one combination of rock properties produces the same seismic amplitude. This feature exists in any inversion because seismic reflections depend on the contrast of elastic properties rather than their absolute values. A probabilistic framework is a natural formal structure to address this non-uniqueness and account for the associated uncertainty (see Buland and Omre, 2003; Bosch, 2004; Gunning and Glinsky, 2004; Connolly and Kemper, 2007; and Sengupta and Bachrach, 2007).

To illustrate a practical implementation of this concept, we apply the physics-driven probabilistic seismic inversion developed in chapter 4 to two datasets to demonstrate how different combinations of reservoir properties can produce a given seismic response. The approach is Bayesian and implements geologic knowledge and an appropriate rock-

physics model to link modeled reservoir properties (thickness, clay content, porosity, and saturation) to the elastic domain. A complete set of forward modeled, three-layer earth and seismic models, generated from a full-grid sampling of the prior distributions, provides the comparative synthetic data to use in the inversion.

Two data sets are used in this chapter. The first data set from offshore Africa includes well and full-stack amplitude data. In previous chapters, this data set was exhaustively explored. To contrast the first data set, well and angle-stack amplitude data from the North Sea comprise the second. The inversion was applied on the seismic data at the well locations. Results from the first data set included a distinct correlation between thickness and porosity with associated uncertainty. For the second data set, the inversion produced independent predictions of thickness and porosity. In both cases, predictions of clay content and saturation were uncertain. The results provided an insight into how accurately reservoir properties can be predicted given the seismic data.

The probabilistic technique allows geologic knowledge to be included in the prior information. It confirms that even for a seismic reflection corresponding to a known reservoir interval, uncertainty surrounds the combination of reservoir properties that underlie the seismic signature. Finally, we show that this probabilistic technique is most successful when based on an appropriate deterministic rock-physics transform that translates the reservoir properties into the elastic domain.

6.2 Methodology

Inversion of seismic data for elastic or rock properties inherently includes non-uniqueness. Consequently, what combinations of rock properties cause a reflection registered from a reservoir? Our physics-driven approach consists of a series of steps that allows us to invoke geologic understanding and rock-physics. Although the full description is presented in chapter 4, it is summarized here. The steps are to construct multiple three-layer models of rock properties; convert them to elastic properties; calculate synthetic seismograms for each model; and, through comparisons between synthetic and real data, invert the latter for rock properties with the associated

uncertainty. By incorporating geology and rock-physics within this method rather than using only elastic properties, we better constrain the ranges of rock properties and their elastic values.

We use a Bayesian scheme to invert the seismic data for reservoir properties. Specifically, we find the probability of modeled values of thickness (H), clay content (C), total porosity (ϕ), and water saturation (S_w) given the measured seismic response (see details of the statistical formulation in Spikes et al., 2007, for the prior distribution, likelihood function, and posterior distributions). The two main assumptions are that (1) a prior interpretation of the seismic data provides a geobody on which to perform the inversion and (2) the shale properties above and below the reservoir are the same. This routine allows us to concentrate on inverting for the rock properties within a reservoir interval and the associated uncertainty within the framework of the assumptions made. Probabilities of the combinations of rock properties account for the uncertainty and natural variability in rock properties.

An example that we use here comes from a geologically mature fluvial environment where the elastic properties are linked to sediment properties by the rock-physics models of Raymer et al. (1980) and Greenberg and Castagna (1992). We also find that ϕ and C are linked by an approximately linear petrophysical transform that reflects the dispersed-shale depositional mode. In this mode, the reduction of ϕ is due to small shale particles filling the pore space of the sand-grain frame. Rock physics and petrophysics are used together to identify the reservoir and then to resolve the values of I_P extracted from the log data within the reservoir for ϕ and C. As expected, we arrive at the correct ϕ and C values.

This methodology consists of six steps. First, identification of the reservoir in both the well and seismic data allows for the construction of a geobody along the seismic event of interest. Second, the well data provides the information to establish a rock-physics transform between porosity, lithology, and fluid and the elastic properties (rock-physics diagnostics). Third, we set bounds and discrete increments for H, C, ϕ, and S_w. Expected spatial variability of the reservoir properties, based on geologic reasoning,

guides the definition of the bounds. Sensitivity of the elastic properties to this variability controls the increments. In other words, if a small change in a rock property results in a significant change in the elastic and/or seismic response, then a small increment is assigned for that property; conversely, if very little change occurs in the elastic and/or seismic response due to a small change in a rock property, then a large increment is used. Fourth, we construct three-layer models for each combination of reservoir properties, while holding constant the properties of the over- and underlying shale, as determined from the input well data. Fifth, for each three-layer model, the rock-physics model translates the reservoir-layer properties into the elastic properties; synthetic seismic traces are calculated for each three-layer model using a P-to-P ray-tracing algorithm. Sixth, an acceptance/rejection rule finds a specified number of synthetic traces that match the real data within a specified correlation threshold. The modeled reservoir properties corresponding to the accepted synthetic traces comprise the calculation of the likelihood function and thus the posterior probability distribution functions (PDFs).

6.3 Two examples

We demonstrate this technique in two different settings. One is a gas reservoir from offshore Africa, where only full-stack seismic data are available. The other is a North Sea gas reservoir with angle stacks available. Each case requires a different rock-physics model to describe the well-log data as well as case-specific ranges and increments of the prior distributions. Stacked synthetic data for each case correspond to the available stacked real data.

6.3.1 Offshore Africa

The Jurassic-aged gas reservoir sits at 3200-3230 m (Figure 6.1). Figure 6.2 displays a cross-plot of I_p (calculated as the product of sonic velocity and bulk density as given by the log curves) versus ϕ, color-coded by C. Superimposed on the cross-plot are I_p versus ϕ curves for varying C, according to the stiff-sand model (the modified upper Hashin-Shtrikman bound of Gal et al., 1998). These model lines establish the relevance of this rock-physics transform to the data under examination. This transform also

converts the rock-property combinations into the corresponding elastic properties for all three-layer variants generated for this application.
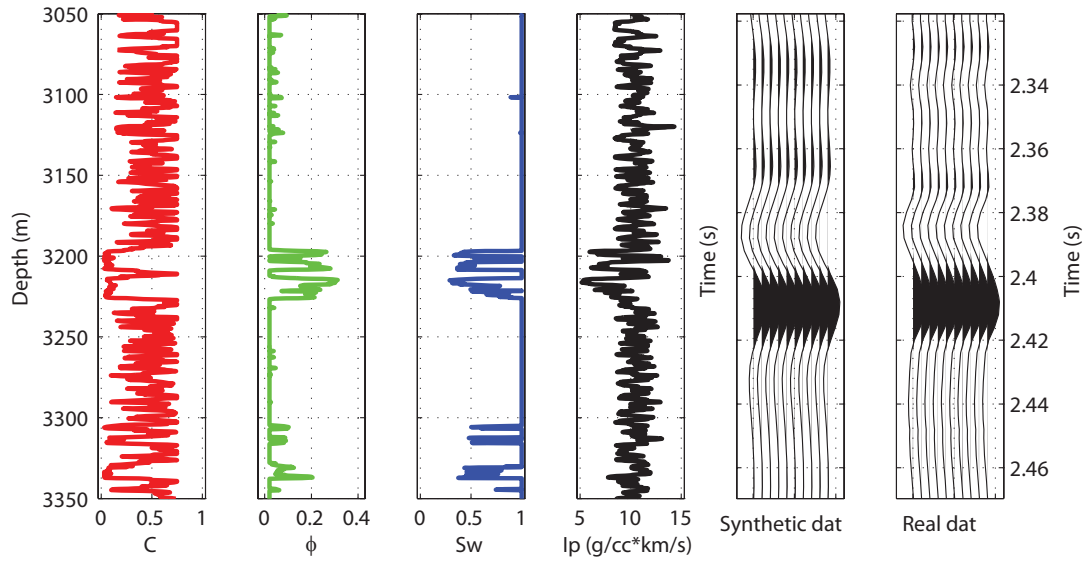
Figure 6.1. Well data from offshore Africa showing the 30-m thick gas reservoir between 3195 and 3225 m. The volume of clay, total porosity, water saturation, *P*-wave impedance, synthetic seismic stack calculated from the well data, and the real stack at the well location. Log curves are displayed versus depth, and seismic traces versus time.
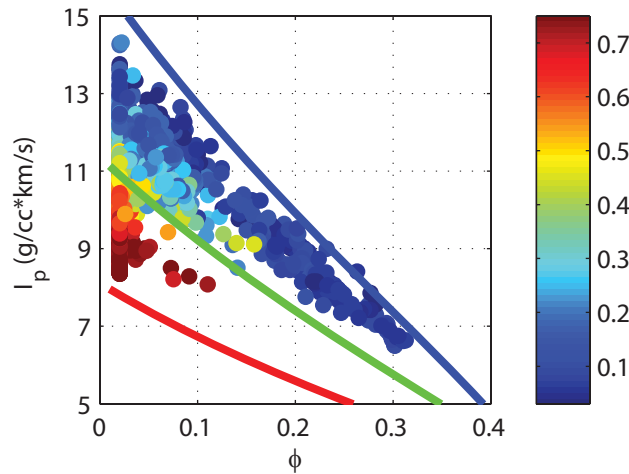
Figure 6.2. *P*-wave impedance versus porosity, color-coded by the clay content for the depth interval displayed in Figure 6.1. Model lines are from the stiff-sand model with clay content zero (blue), 0.5 (green), and 1.0 (red).

We set the range for the H prior distribution from 15 to 60 m (from half to twice the thickness of the reservoir at the well). The range of C was 0 to 0.2, whereas the ϕ range

was from 0.18 to 0.32. Lastly, the S_w range was set from 0.2 (the assumed irreducible water saturation) to 1.0. The lower limit of ϕ (0.18) was selected to limit the number of realizations although some clean sands show a lower ϕ. Sensitivity of synthetic seismic traces to small changes in each parameter guided the increment values. Specifically, these increments were 5 m for H, 0.01 for C and ϕ, and 0.1 for S_w. These ranges and increments within a full-grid sampling resulted in 28350 prior earth and corresponding seismic models. Construction of the three-layer models and synthetic full-stack traces followed the range and increment definitions. The synthetic seismic data were calculated from a *P*-to-*P* ray-tracing algorithm. Each of these synthetic traces was cross-correlated with the real trace at the well. Inversion parameters included acceptance of 15% of the total number of synthetic traces with an initial 90% correlation threshold. Results consisted of the full four-parameter conditional PDF and the marginalized PDFs.

Figure 6.3 contains the bivariate PDFs where each PDF is the probability distribution of two reservoir properties taken at a time (shown in color). With four reservoir properties in the inversion, six bivariate distributions result. These surface plots indicate that predictions of C and S_w within the *a priori* set limits are uncertain. Evidence for this is present in all the PDFs that contain C, S_w, or both, in that many of the values of these reservoir properties have a high probability of occurring. On the other hand, relatively narrow ranges of H and ϕ exist in the PDFs that include either of these two parameters. The bivariate PDF of H and ϕ illustrates that these two parameters are quite well correlated. Specifically, the inversion predicts a high probability of small modeled H occurring with a relatively high ϕ; a large modeled H has a high probability of occurring with a lower ϕ. This distribution also indicates that the most likely values of H and ϕ correspond to the values observed in the well data.
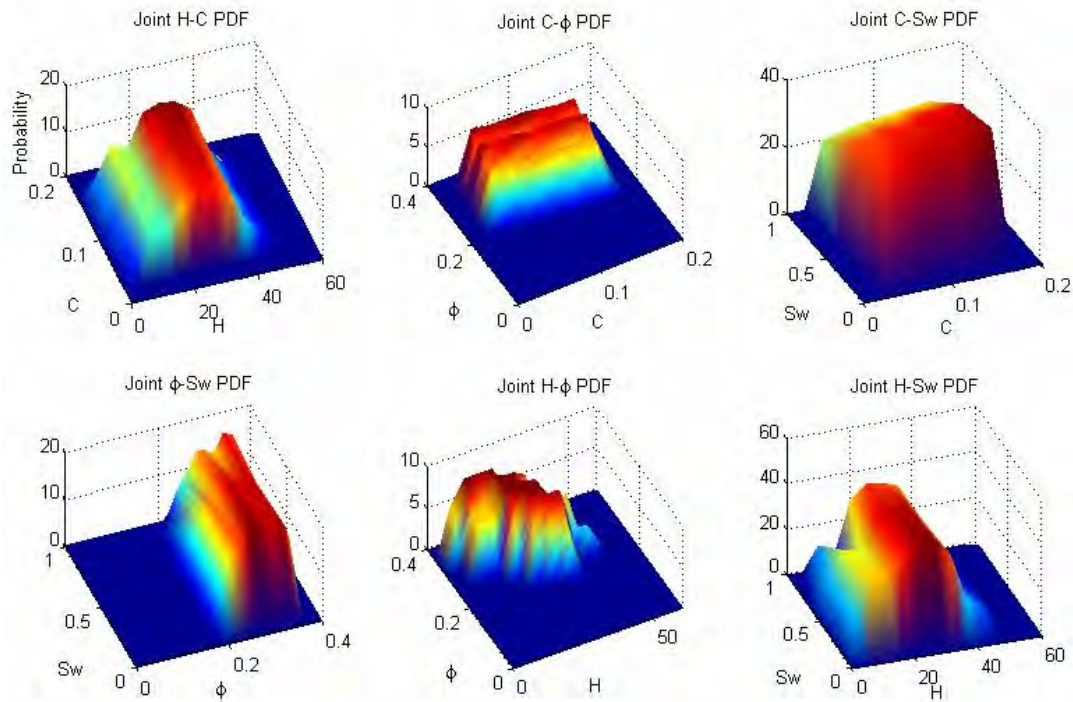
Figure 6.3. Bivariate PDFs for each of the 2-parameter combinations. The PDFs that include clay content or water saturation indicate that the predictions of these two parameters are highly uncertain. The broad appearances of these PDFs manifest that all possible values of these two parameters are nearly equiprobable. On the other hand, the thickness and porosity PDFs indicate the narrow ranges of these parameters. Moreover, we observe a clear and almost linear relation between these two parameters.

Posterior PDFs exist for each reservoir property taken by itself, also called marginal PDFs. However, these marginal PDFs do not directly illustrate how the reservoir properties combine to produce the same elastic response. Four trivariate posterior PDFs, (PDFs where three properties are taken at a time) exist, as well as the full four-parameter conditional PDF. However, displaying these multivariate PDFs is somewhat problematic. We feel that the bivariate posterior PDFs (Figure 6.3) suitably illustrate the relationships between the properties.

The posterior PDFs provide the values of the reservoir properties and the combinations thereof that have a high probability of occurrence. Accordingly, the most likely values or most likely combinations can be selected from any of the posterior PDF. Figure 6.4 shows the well data at the reservoir. Superimposed on these log curves are

values of the reservoir properties from the most likely combination of properties taken from the full conditional four-parameter posterior PDF. Extracting this most likely combination provides a value for each reservoir property, in which the four properties are not independent of one another. In other words, the four reservoir properties occur together to provide the corresponding elastic response. The values of the reservoir properties from this combination are $H = 35$ m, $C = 0.15$, $\phi = 0.22$, and $S_w = 0.6$. These predicted, most likely values fall fairly close to the actual values at the well.
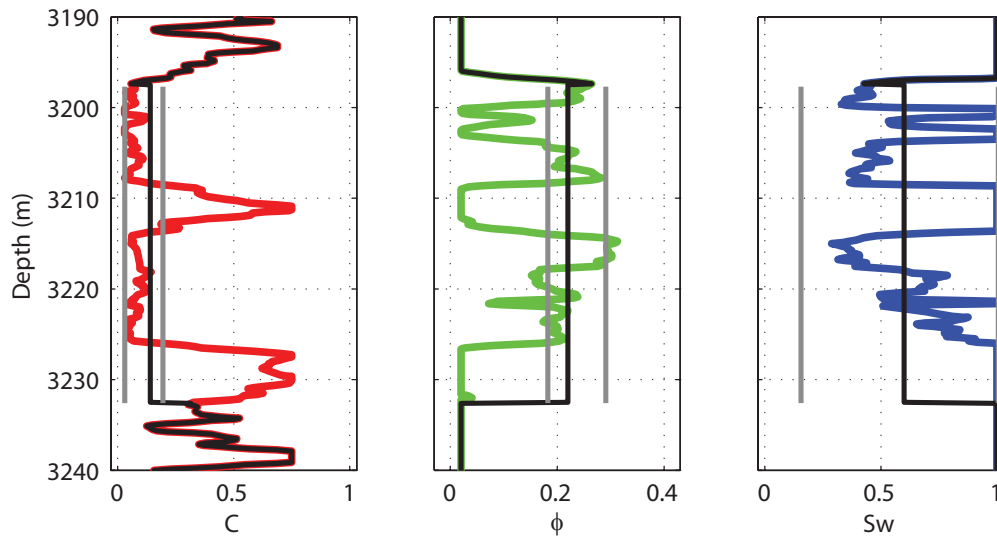
Figure 6.4. The full conditional posterior PDF of all four parameters from a 4-D histogram, which we elect not to display. Within the reservoir unit, the most likely values (black lines) are superimposed upon the actual well data. The gray lines indicate the minimum and maximum values of the 90th percentile ranges. The corresponding minimum and maximum values of thickness in the 90th percentile are 10 and 35 m, respectively, although not displayed.

6.3.2 North Sea

The North Sea gas reservoir is a 160-m succession of gas-filled intervals (Figure 6.5). Both the top and bottom of the reservoir can be delineated in the synthetic seismic data, as well as internal reflections. This is significantly different from the offshore Africa example, in which only the top of the reservoir could be seismically identified. Angle gathers from a location away from the well were available in the North Sea data set. We used angle stacks from near- and far-angle ranges.
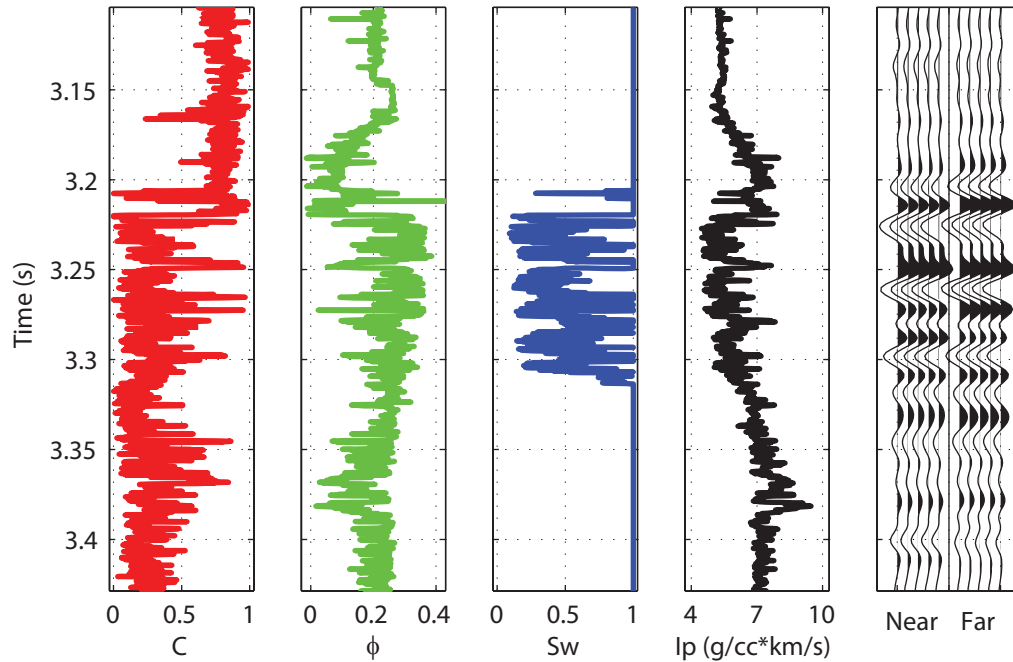
Figure 6.5. Well data from the North Sea gas reservoir from 3.21 to 3.32 s (160-m thick). From left to right are the clay content, porosity, water saturation, *P*-wave impedance, and synthetic seismic traces.

Because seismic data were not available at the well location, we had the opportunity to apply this method in an exploration sense. The procedure was the same in that the well data provide the basis to establish the rock-physics model and estimates of the ranges and increments for the prior distributions. The rock-physics model applicable here is the constant cement model (Avseth et al., 2000). Figure 6.6 confirms this selection as indicated by the model curves superimposed on the cross-plot of I_p versus ϕ, color-coded by C. The ranges and increments for the prior distributions used here were 100 to 200 m and 10 m, respectively, for H; zero to 0.2 and 0.02 for C; 0.1 to 0.3 and 0.01 for ϕ; and 0.2 to 1.0 and 0.2 for S_w. These choices resulted in 24255 earth models and synthetic seismic gathers.
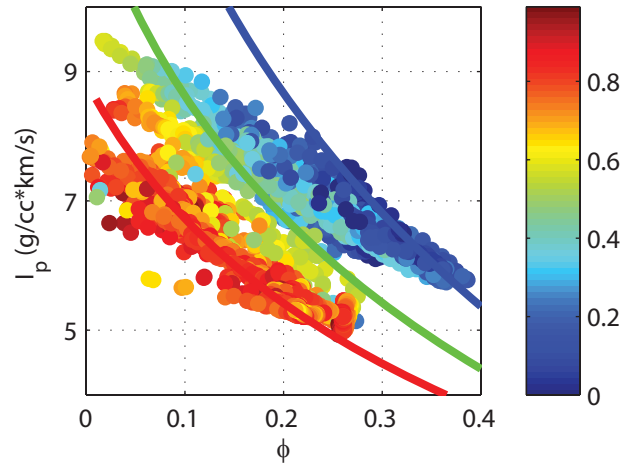
Figure 6.6. The *P*-wave impedance versus porosity, color-coded by the clay content for the depth
   interval shown in Figure 6.5. The model lines are from the constant cement model for zero
   clay (blue), 0.5 clay (green), and 1.0 clay content (red).

With these ranges and increments, the three-layer earth models were constructed for
each combination of reservoir properties. The P-to-P ray tracer provided the synthetic
angle gathers, from which we calculated near- and far-angle stacks over the same angle
ranges as in the real data. The synthetic-to-real match criterion was a 5% acceptance rate
with an initial 80% correlation threshold.

The resulting six bivariate PDFs are displayed in Figure 6.7. Three of them, $H - C$,
$C - S_w$, and $H - S_w$ exhibit a broad appearance, which means that most combinations of
in these three pairs have a high probability of occurring. The other three PDFs indicate
high probabilities for a limited number of combinations. Specifically, similar to the
offshore Africa example, the most dominant factors are H and ϕ. However, the relation
between these two parameters in this North Sea case differs from the first example.
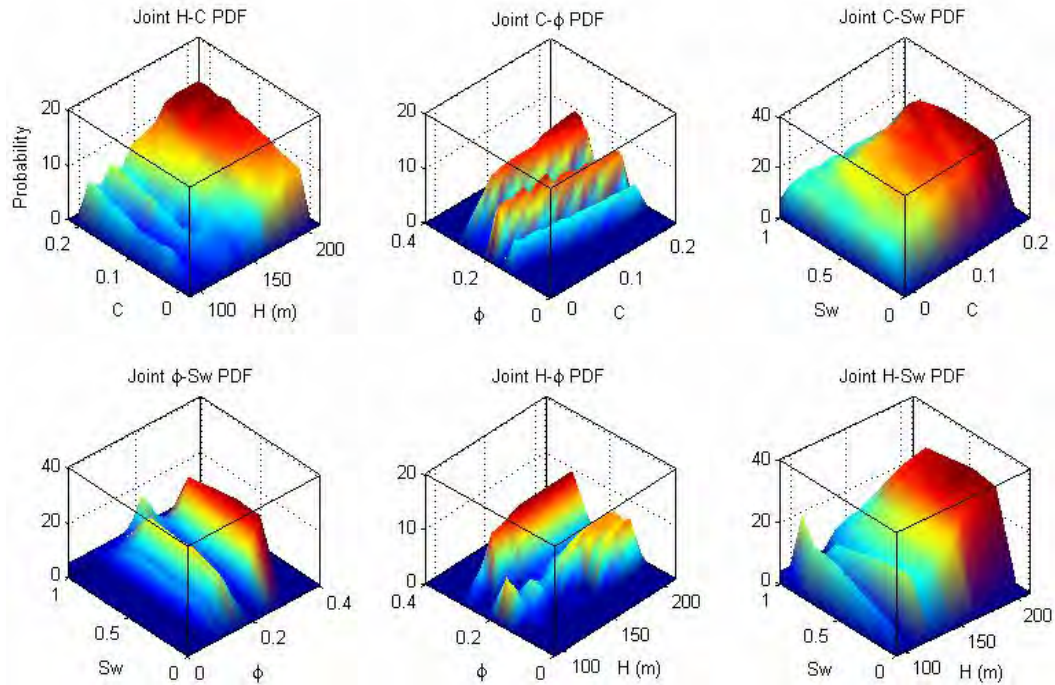
Figure 6.7. Bivariate PDFs for six two-parameter combinations. PDFs with the clay content or saturation component exhibit high uncertainty.

The calculation of the posterior PDFs yielded the most likely values and combinations of the four modeled reservoir properties. We selected the most likely combination from the full conditional four-parameter PDF: $H = 120$ m; $C = 0.18$; $\phi = 0.20$; and $S_w = 0.4$ (Figure 6.8). We see that thickness, porosity, and saturation are slightly underestimated, whereas clay content is predicted relatively well. Based on the bivariate PDFs in Figure 6.7, the most accurate predictions are for H and ϕ, with the predictions of C and S_w being the most uncertain.
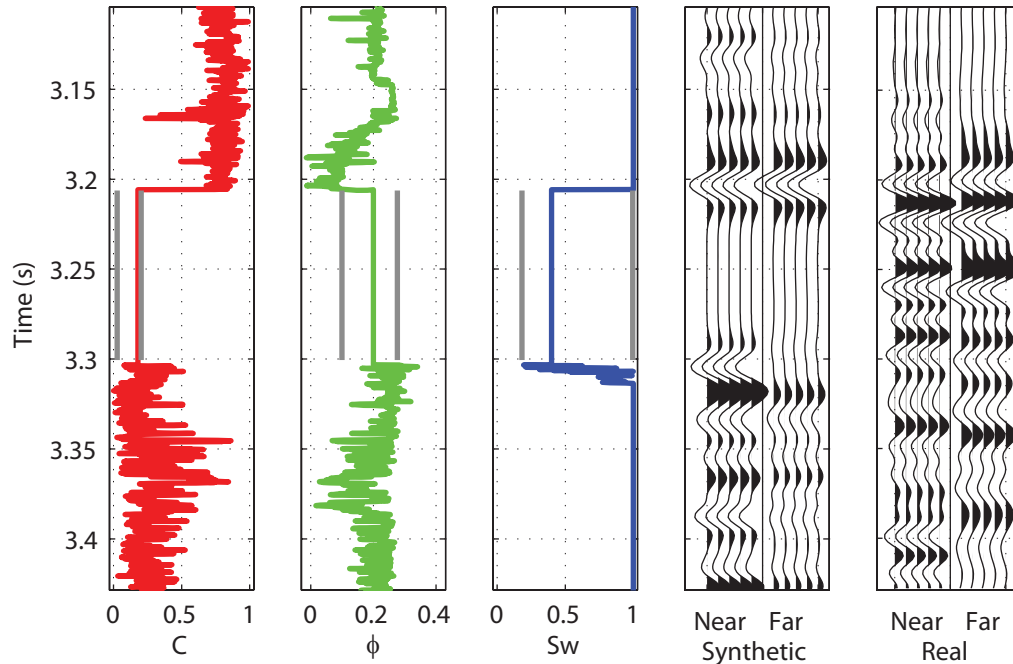
Figure 6.8. The most likely combination of reservoir properties from the full conditional posterior distribution includes thickness of 120 m, clay content of 0.2, porosity of 0.2 and saturation at 0.4. The corresponding most likely synthetic seismograms are displayed next to the real data. For the log curves, 90th percentile minimum and maximum bounds are plotted in gray. The corresponding bounds for thickness are 110 and 180 m, respectively.

6.4 Discussion

Both applications of the probabilistic seismic inversion reveal that H and ϕ are the most certain parameters to be predicted. In the offshore Africa example, where a $H - \phi$ trend and the associated uncertainty were obtained from the posterior distributions, it is apparent that the resolution of the seismic data prevents these two parameters from being predicted separately. However, the obtained linear trend between H and ϕ allows us to calculate the total pore volume (the product of H and ϕ) with high certainty. Results from the North Sea example do not reveal a trend or relationship between H and ϕ. The reason is that the thickness of the reservoir in this example was greater than the seismic resolution. As a result, H and ϕ can be predicted separately, without the need to establish a trend from the posterior PDFs.

Uncertainty dominates the prediction of S_w and C in both examples. This result is expected. The two rock-physics transforms used, the stiff-sand and constant-cement

models, have stiff frames, on which S_w has little effect. Regarding the uncertainty in C, lithology prediction often requires offset data, which were not available in the first example. This prevented an accurate prediction of C, although the selected range, 0-0.2, was relatively narrow. In the second example, the angle-dependent response of the real and synthetic data was relatively small, which did not permit us to pinpoint C within the zero to 0.2 interval.

6.5 Conclusions

These two examples show how a group of final earth models can be determined, corresponding to a collection of synthetic seismic traces that best match the real data. Those earth models contain combinations of reservoir properties, namely thickness, clay content, porosity, and saturation, and each property may have a relatively broad range of variation. Nevertheless, the results presented here are functional. Indeed, in the first case, we observe a clear trend between the output porosity and thickness, which means that their product is essentially constant. In the second case we fairly accurately isolate the porosity of the gas sand.

These results will vary depending on the geologic and rock-physics specifics. The two concrete examples demonstrate how to make this general methodology site-specific. Confidence in the answers will vary depending on the depositional setting and availability of seismic and control-well data. We anticipate that in some cases the results will be too uncertain to be used in decision making. On the other hand, with many *a priori* constraints, such as known porosity and saturation, our predictions will be quite definite.

6.6 Acknowledgements

Chapter 7
Sensitivity of the seismic-inversion method to saturation and user-defined parameters

"With every new answer unfolded, science has consistently discovered at least three new questions."

--Wernher Von Braun

7.1 Abstract

This work presents a two-part sensitivity analysis study based on synthetic data. The importance of this study is to demonstrate the ability of the seismic-inversion method presented in earlier chapters to detect fluid saturations and to examine how user-defined parameters affect the inversion results. A synthetic dataset provides the basis on which to test the different capabilities of the inversion. In the first test, all calibration work is done using a gas well, and the inversion is used to predict brine saturation in a second well using only seismic data. Two additional tests examine how changing three user-defined parameters affects the results. Those parameters are the fraction of matching synthetic traces to accept, the initial cross-correlation threshold, and the length of the cross-

correlation window. In the second test, the fraction of synthetic traces to accept is varied along with the initial correlation threshold. Third, the cross-correlation window length is varied while keeping the other parameters fixed. Results of the saturation test indicate that if the seismic signatures of gas- and brine-saturated sands are markedly different, then the inversion predicts the appropriate fluid and associated uncertainty. Varying the fraction of accepted synthetic traces shows that as long as the noise level in the seismic data does not become overly large, then accepting ten percent of the synthetic traces provides accurate results. Along with this, however, the final correlation threshold must be considered an important part of the inversion result. Changing the length of the cross-correlation window increases the influence of the normalization scheme, which tends to include low-energy synthetic traces corresponding to high porosity and high saturation values. In conclusion, the inversion can be used successfully for joint thickness, porosity, and saturation predictions, whereas precise mineralogic predictions remain difficult. The user-defined parameters must be calibrated properly at a well location to identify the optimal settings for them. If the seismic data is excessively noisy, the inversion results may be a function of random and unreliable matches between the real and synthetic seismic data. In all cases, the inversion may accept low-energy synthetic traces that do not represent the *in-situ* conditions, because of the normalization operation.

7.2 Introduction

A synthetic dataset provides the platform on which to test the sensitivity of the seismic-inversion algorithm presented in chapters 4−6. We test the sensitivity of the algorithm to variations in reservoir properties and conditions and variations in user-defined parameters. In practice, most seismic-inversion algorithms must be calibrated to the input data by including user-defined parameters that must be determined experimentally or through an optimization routine. The values assigned to these parameters typically affect the inversion results. Exploring how the results change requires a sensitivity analysis.

This work serves two purposes. The first is to explore the ability of the algorithm to predict fluid saturation in a synthetic dataset. The second examines the sensitivity of the results to variable values of two user-defined parameters: the fraction of synthetic traces to accept and the length of the cross-correlation window. These tests are performed using seismic data that contain different amounts of noise.

A synthetic reference dataset is constructed that incorporates often-observed problems and intricacies in real data. This dataset includes well-log and seismic data for different fluid scenarios (gas and brine). A rock-physics model links a vertical succession of rock properties and their associated elastic properties. The resultant seismic data serves as a proxy to recorded seismic data. To replicate better a realistic situation, Gaussian noise is added to the proxy seismic data.

Results show that for this synthetic dataset fluid saturations can be discriminated successfully. Moreover, the sensitivity tests reveal that the best results are achieved when fewer than 10% of the synthetic traces are accepted, although this result becomes obscured when seismic noise increases. An optimal cross-correlation window length accompanies this fraction of accepted traces. In all three tests, however, the inversion sometimes accepts incorrect reservoir-property combinations. These combinations are accepted because of a normalization calculation in the trace-comparison procedure.

7.3 Reference Data

We generated two reference datasets to serve as proxies for real data, one corresponding to a gas reservoir and the other to a brine-saturated sand interval. To construct the datasets, we defined well-log curves; converted them to elastic curves using a rock-physics model; computed the proxy seismograms; and added different amounts of Gaussian noise to the proxy seismic data. To create well logs, we defined mineralogy (clay/quartz mixture), porosity, saturation, and effective pressure curves over a depth interval of 600–1500 m. The synthetic reservoir was 27 m thick with its top at 1475 m (Figure 7.1). For the section above the reservoir, the geometry and log-curve values were constructed using normally distributed indicator variables. After constructing the curves

for the gas-saturated scenario, the soft-sand rock-physics model (Dvorkin and Nur, 1996) translated the rock properties to elastic properties (Figure 7.2). Once we calculated the elastic properties from the rock-physics model, we used Gassmann (1951) fluid substitution to generate elastic curves for the brine-saturated case.
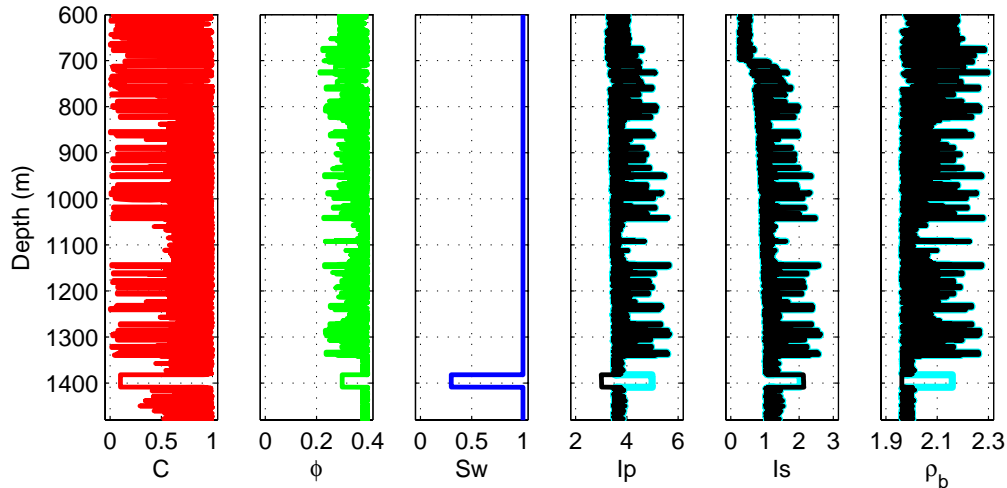
Figure 7.1. Reference well log data for the gas-reservoir and brine-sand scenarios. Elastic properties for the gas-saturated case are in black and cyan for the brine-saturated case.

We wanted our model to be sensitive to changes in thickness, lithology, porosity, and saturation of the reservoir sand. Accordingly, we chose to use the soft-sand rock-physics transform (Dvorkin and Nur, 1996), which describes soft or unconsolidated sands in terms of their elastic properties. The unconsolidated nature of these reservoir rocks allows the pore fluid to exert measurable changes in the effective elastic properties, so that changes in fluid saturation should be detectable in the corresponding seismic data if the overlying or underlying shales are different enough in the elastic domain. If we used a model for stiff or consolidated sand, it would be more difficult to detect fluid changes, because the stiffness of the rock matrix would dominate the effective elastic properties.
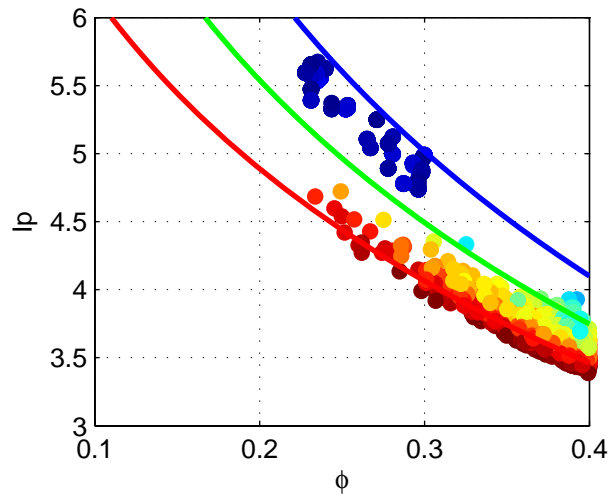
Figure 7.2. Reference well-log data in the brine-saturated case, plotted in porosity-impedance space. Soft-sand model lines for 0%, 50%, and 100% clay content overlie the data points.

After we generated elastic well-log curves, we used a P-P ray tracer to compute the corresponding reference seismic data. A 30 Hz, 100-sample Ricker wavelet was used at a 4 ms sampling rate. Thickness of the reservoir and the frequency of seismic data were designed so that the top and bottom of the reservoir could be delineated. For both sets of well data (gas and wet), angle gathers were computed from 0 to 30 degrees. We stacked traces from 0 to 15 degrees to form the near-offset angle-stack trace and from 16 to 30 degrees to form the far-angle stack. The inversion requires both these angle-stack traces. Because the well data are synthetic, they contain no noise and thus do not represent a realistic scenario. To introduce some variations in the seismic data, we added Gaussian random noise to the stacked traces in the amounts of 0.1%, 0.5%, and 1%. The percentage of noise was based on the energy of each trace. This was done for the reference seismic dataset corresponding to the gas reservoir. Figure 7.3 displays the proxy seismic data with 0%, 0.1%, 0.5%, and 1% noise, in which the diversion from the noise-free case is quite apparent.
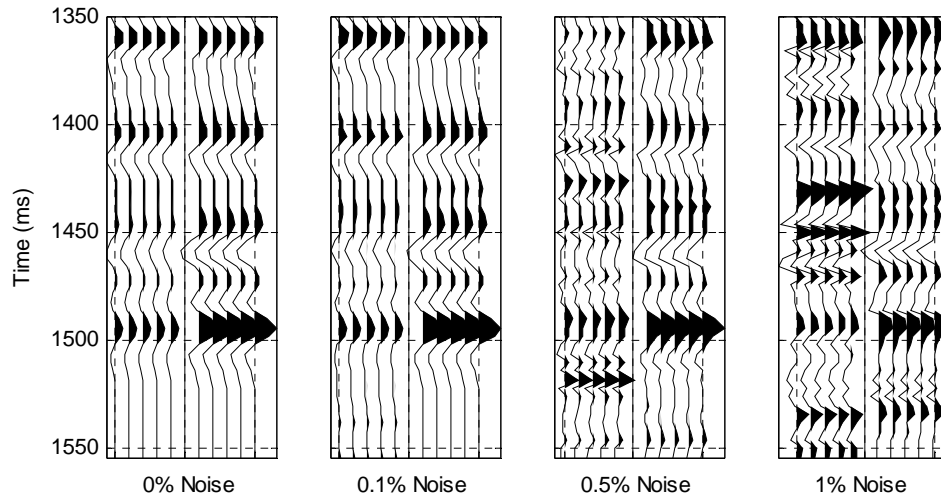
Figure 7.3. Reference seismic data with 0%, 0.1%, 0.5%, and 1% noise added. Degradation of the signal is clearly seen as noise increases. The top of the reservoir is at 1460 ms and the bottom is at 1490 ms. In each frame, five near-angle stacked traces are displayed in the left half and five far-angle stacked traces in the right half.

7.4 Inversion method and tests

The inversion algorithm computes the conditional joint posterior probability distribution function (PDF) of the reservoir properties given the measured seismic data. The reservoir properties are thickness H, clay content C, porosity ϕ, and saturation S_w. The measured seismic data in this case are the reference or proxy seismic data. The algorithm is designed to capture changes in the measured seismic response due to noise or natural variation. Additionally, it determines the ranges of underlying reservoir properties that can combine to produce a seismic response matching the measured response within some user-defined threshold. Cross-correlation is used to compare all the forward seismic models to each measured or proxy seismic response. The cross-correlation function is calculated over windows around the reservoir unit in both the measured and modeled seismic traces. The goal is to accept a minimum number of the forward models with a maximum cross-correlation coefficient. Coefficients are normalized by the geometric mean of the energies of the two correlated traces. Three user-defined parameters must be determined: 1) the fraction or number of synthetics to

accept; 2) an initial correlation threshold; and 3) the length of the cross-correlation window.

We define the prior range of H as 3 to 57 m with a 6-m increment. Clay content ranges from 0.0 to 0.2 with an increment of 0.02. Porosity ranges from 0.10 to 0.40 with a 0.01 increment. Saturation varies from 0.2 to 1 with a 0.10 increment. Given this parameterization, the total number of forward models is $10 \times 11 \times 31 \times 9 = 30690$. The rock-physics model used is the same one used to construct the reference data, the soft-sand model. All parameters for the rock-physics model were the same as those used for the reference data construction. As a result, no variability in the rock properties exists between the reference data and the forward models. To generate the seismic forward models, we computed the angle gathers and stacks over the same range as the reference data. The same wavelet and wavelet parameters were used. No noise was added to the seismic forward models. This full set of forward seismic models represents the possible seismic signatures given the variation in the underlying combinations of reservoir properties.

7.4.1 Saturation test

The first of our three sensitivity tests was a saturation-prediction trial. If this algorithm is to be used as a reservoir characterization tool in an exploration setting, then it should be able to detect fluid changes. To test this, we examine first how the inversion predicts the *in situ* conditions noiseless reference seismic data. Then we invert the data at the wet well to see whether different saturation conditions can be predicted.

Values of the proxy data in the well are H = 27 m, C = 0.10, ϕ = 0.30, and S_w = 0.3. We accepted 1% of the total number of synthetics at an initial correlation threshold of 0.6. The cross-correlation window length was 240 ms. The predicted values from the full conditional posterior were H = 27 m, C = 0.12, ϕ = 0.3, and S_w = 0.2. The final, iterated correlation threshold was 0.9963, which indicates the prediction of the input data is quite good.

The 4-D full conditional PDF cannot be displayed in its entirety because of its dimensionality. To visualize this PDF, a conditional form of it can be displayed by holding one parameter constant. For this purpose, C is held constant at 0.12. The 90th percentile values of $P(H, \phi, S_w | C = 0.12)$ are displayed in Figure 7.4. Although a discontinuous surface is displayed, noticeable characteristics are apparent. First, a ϕ value of 0.3 is predicted for H values ranging from 9 to 27 m, with S_w ranging from 0.2 to 0.3. A small portion of the surface sits at $\phi = 0.31$ with $H = 3$ m and a slightly higher S_w at 0.5. The uppermost portion outlines ϕ values of 0.33-0.34, $H = 3$ m, and $S_w = 0.8$ to 0.9. Therefore, the seismic responses for $H = 9$ to 27 m are quite similar for small S_w. As ϕ increases, H decreases and S_w increases. Even though resolution of the proxy seismic data was high enough, this PDF shows a trade off between H and ϕ.
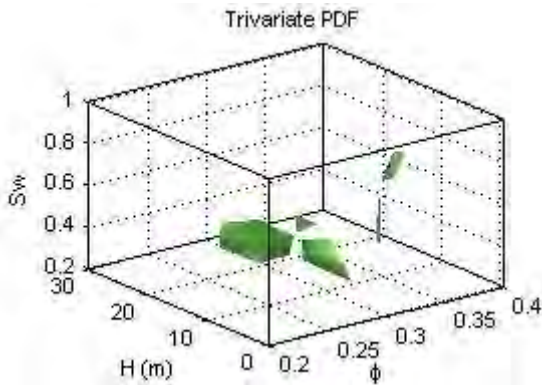
Figure 7.4. Iso-probability surface for the full conditional PDF with clay content equal to 0.12.

For the brine-saturated case, the measured parameters were the same as in the gas well, except $S_w = 1$. Inversion parameters were the same, with an acceptance of 1% of the total traces at an initial 0.6 correlation, and a 240-ms cross-correlation window. The predicted values were $H = 27$ m, $C = 0.0$, $\phi = 0.3$, and $S_w = 1$. The final correlation threshold was 0.879. In Figure 7.5 are the proxy seismic data for the brine-saturated scenario and the full conditional PDF conditional to $C = 0.12$. The most noticeable feature of the seismic data is the polarity reversal at 1460 ms compared to the 0% noise seismic data in Figure 7.6. In terms of the synthetic seismic traces used in the

comparison, only those with $S_w = 1$ have opposite polarity at the reservoir interval under examination. Therefore, in the comparison stage, depending on the number of synthetic traces accepted, only the traces with this polarity are accepted. This results in a narrow range of predicted reservoir-property values present on the iso-probability surface.
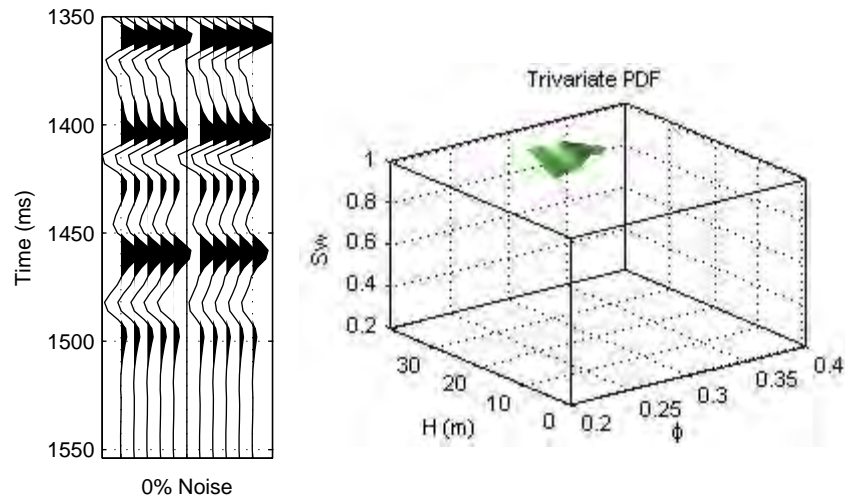
Figure 7.5. Proxy seismic data at the wet well (left). Five near- and five far-angle stacked traces are displayed. The posterior PDF (right) shows that a limited number of possible combinations or reservoir properties are likely to occur.

7.4.2 Variable accepted trace fractions

This test examines how the inversion results change as the number of accepted synthetic traces is varied. We show the most likely values for each of the reservoir properties from the posterior marginal, bivariate, trivariate, and full conditional PDFs. Figure 7.6 shows the most likely values for the marginal PDFs as a function of the fraction of synthetic traces accepted for the four noise levels. Blue corresponds to accepting 0.01 of the total number of synthetics and red to 0.40. The most likely values from the marginal PDFs for the different reservoir properties are independent from one another, just as they are in prior. Accordingly, the uncertainty in these values is higher than the uncertainty in the most likely values from any of the posterior multi-variate PDFs. Nonetheless, it is clear that the accuracy of the predicted values of any of the

reservoir properties decreases as the trace fraction increases but not in a monotonic or regular fashion. In terms of noise in the proxy seismic data, H predictions are most accurate at the 0.5% level. For C, the scatter in the results makes them difficult to interpret. Most likely values of porosity are most accurate for all noise levels when 5% or fewer of the traces are accepted. The same is true for S_w.
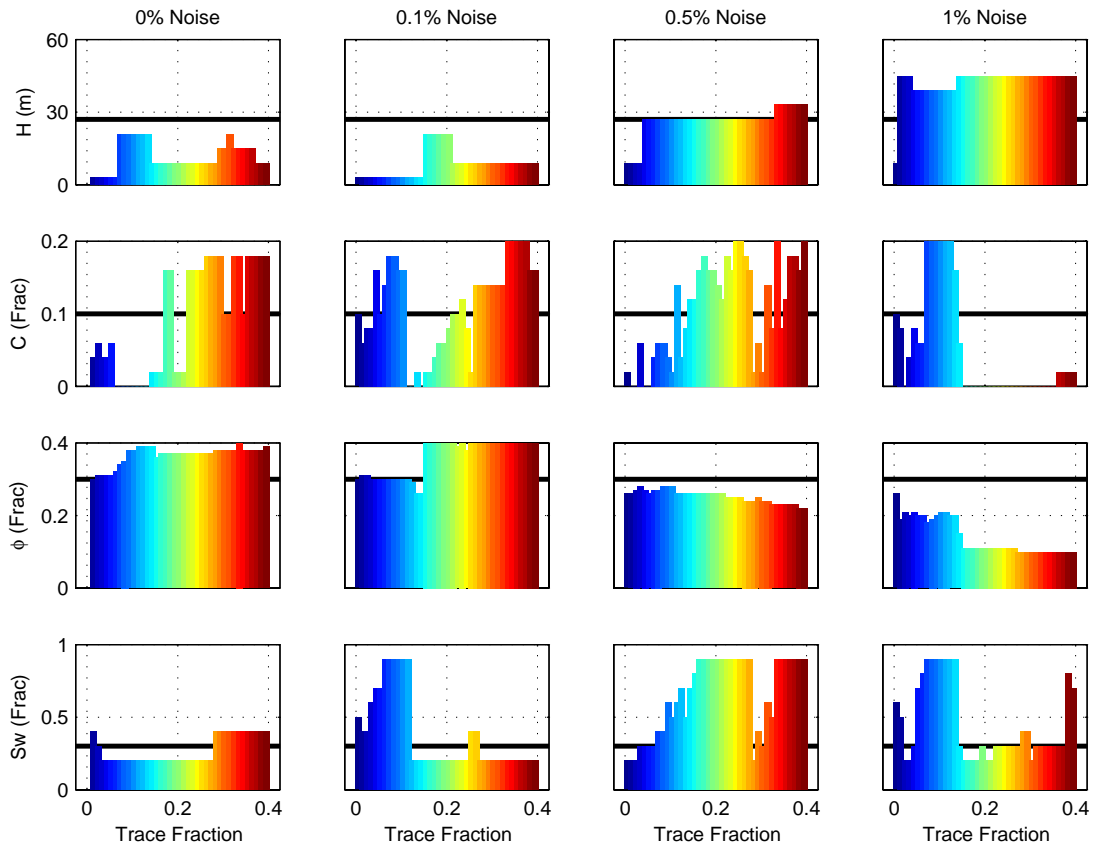
Figure 7.6. For each of the inversion scenarios with a different fraction of accepted traces, a posterior marginal distribution exists for each reservoir property. In each instance, the most likely value from that marginal PDF is selected and plotted here versus its corresponding accepted trace fraction. Cold colors correspond to lower trace fractions with blue indicating a minimum of 0.01 and red a maximum of 0.4. Horizontal black lines indicate the value of the reservoir property in the well data.

In Figure 7.7 are the most likely values from the bivariate PDFs. Color is the same as in Figure 7.6. The labels on the horizontal axes indicate the bivariate PDF from which the most likely value was extracted. Each reservoir parameter occurs in three of the six posterior PDFs. Drawing from the posterior bivariate PDFs means selecting the most

likely combination of reservoir properties. Accordingly, the most likely values are not independent from each other as they were in the marginal case.

Accuracy of the results should decrease with increasing noise, but quantifying that claim is not straightforward from these results. The relationship between H and ϕ begins to emerge, especially in the 0.1% and 0.5% noise cases, where H is over-predicted while ϕ is under-predicted. In fact, even at 1% noise, a combination of H and ϕ can still be observed. This is seen by looking at the H and ϕ values taken from the H-ϕ bivariate PDF. In the cases with less noise, H is under-predicted and ϕ is over-predicted. However, predictions of C and S_w lack an obvious pattern. Furthermore, a relationship between H and C emerges, with under-predictions of H corresponding to over-predictions of C. For very small H values, S_w increases, but this happens when the accepted trace fraction is less than 0.05 for noise levels of 0%, 0.1%, and 0.5%.
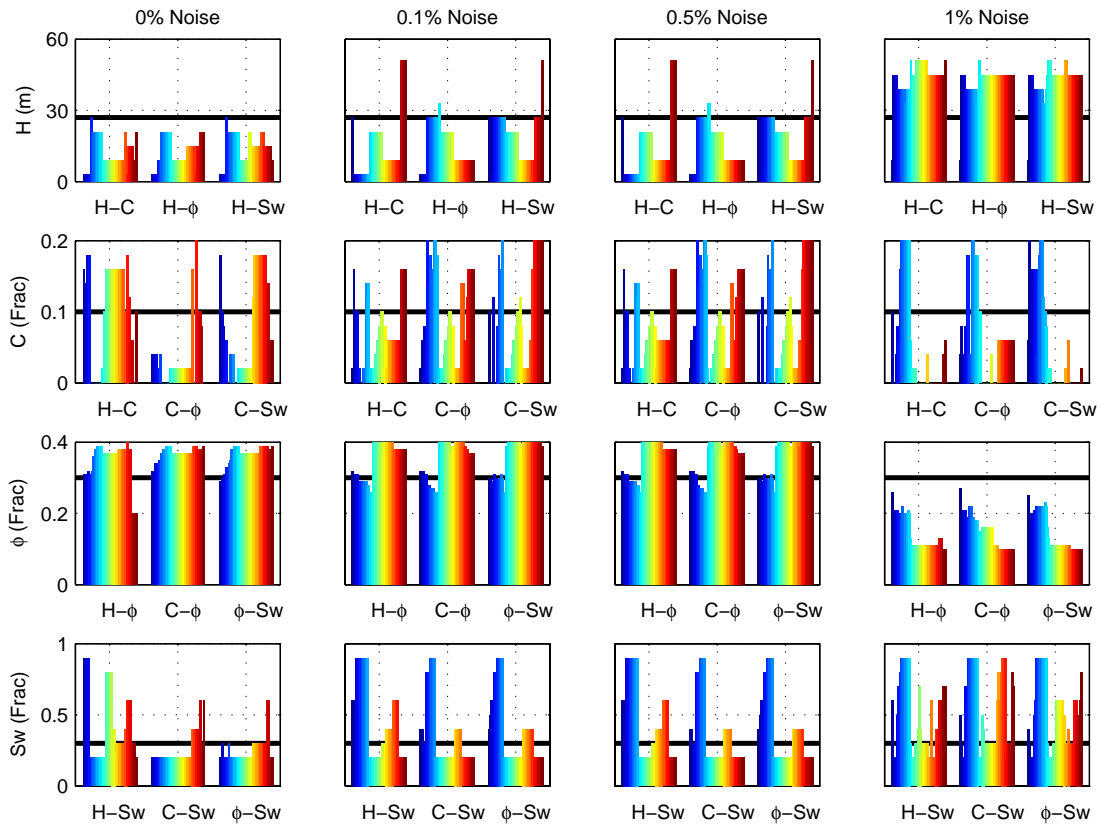
Figure 7.7. Most likely values from the posterior bivariate PDFs. For each noise level, three most likely values of the reservoir properties are possible for each accepted trace fraction. Blue corresponds to 0.01 fraction and red to 0.4. These most likely values are no longer independent from one another. The most likely combination of each reservoir-property pair for a given bivariate PDF was selected. The most-likely value changes as the fraction increases because in most cases, multiple combinations of reservoir properties is the most likely to occur. When this occurs, one combination is chosen at random, and often the most-likely value will change from one inversion to another.

Similar to the sets of most likely values from the bivariate posterior PDFs are those from the trivariate PDFs (Figure 7.8). As seen in the most likely values from the marginal and bivariate PDFs, the C parameter is the most uncertain, given the erratic appearances of the plots for all noise levels. We also see more clearly the relationship between H and ϕ, in which a larger H corresponds to a smaller ϕ and smaller H to higher ϕ. However, S_w predictions are scattered. When the accepted trace fraction is about 0.10, the best prediction of H, ϕ and S_w occurs, but C predictions are not always accurate. For these results, Figure 7.4 provides additional insight into the selection of the most likely values, particularly with 0% noise. As noise increases to 0.1% and 0.5%, the

inversion does quite well for H and ϕ. However, C and S_w predictions begin to degrade. At 1% noise, H is over-predicted and ϕ is under-predicted for scattered C and S_w values.
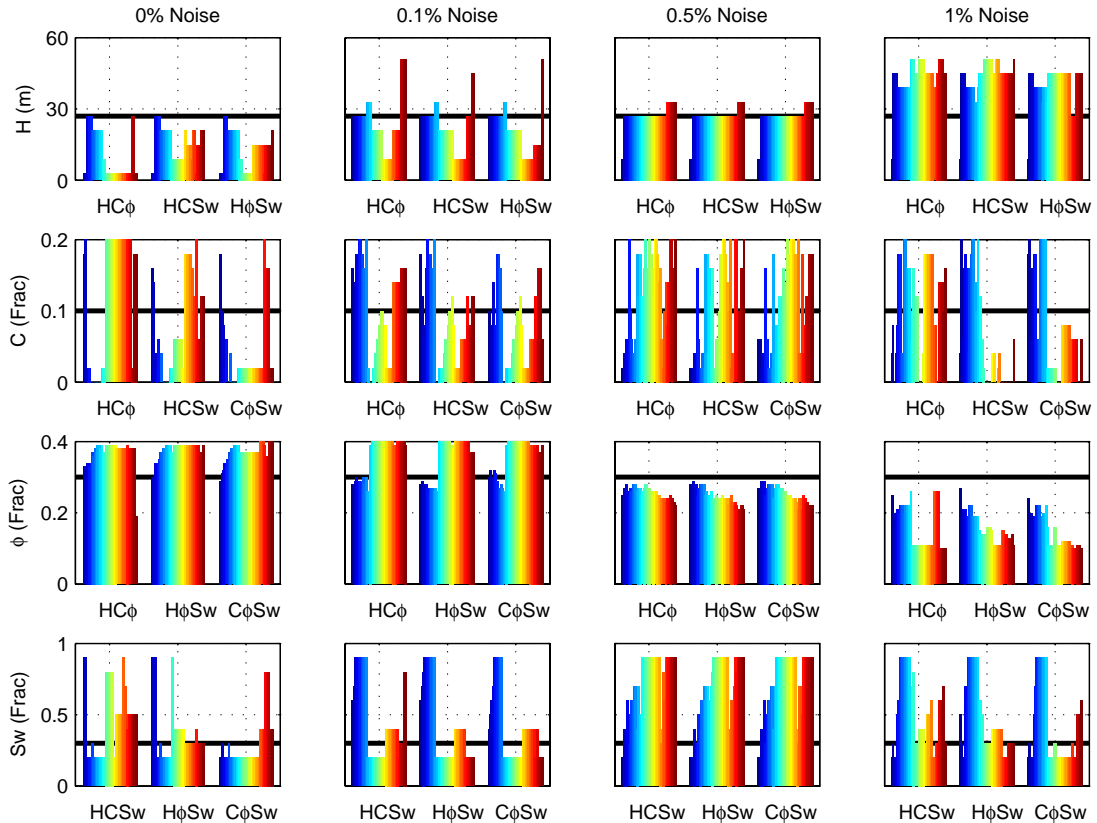
Figure 7.8. Most likely values from the posterior trivariate PDFs, in which combinations of three parameters are taken at a time. A relationship between thickness and porosity emerges, whereas predictions of clay content and saturation appear uncertain.

The final set of most likely values from this test come from the full conditional posterior PDF (Figure 7.9). In the zero-noise case, H-ϕ-S_w combinations are quite accurate for accepted trace fractions of 0.05 and less. Above this, H is under-predicted and ϕ is over-predicted, while C and S_w values appear to be random. When the noise increases to 0.1%, the optimal solution occurs at a trace fraction of 0.10. At greater fractions, again H is under-predicted and ϕ is over-predicted. At a smaller fraction, ϕ is under-predicted while S_w is over-predicted. At 0.5% noise, fairly accurate predictions of H and ϕ occur for accepted trace fractions of less than 10%, but C and S_w become

scattered. By the time the noise level reaches 1%, all predictions are relatively inaccurate, but H is consistently over-predicted with an under-prediction of ϕ.
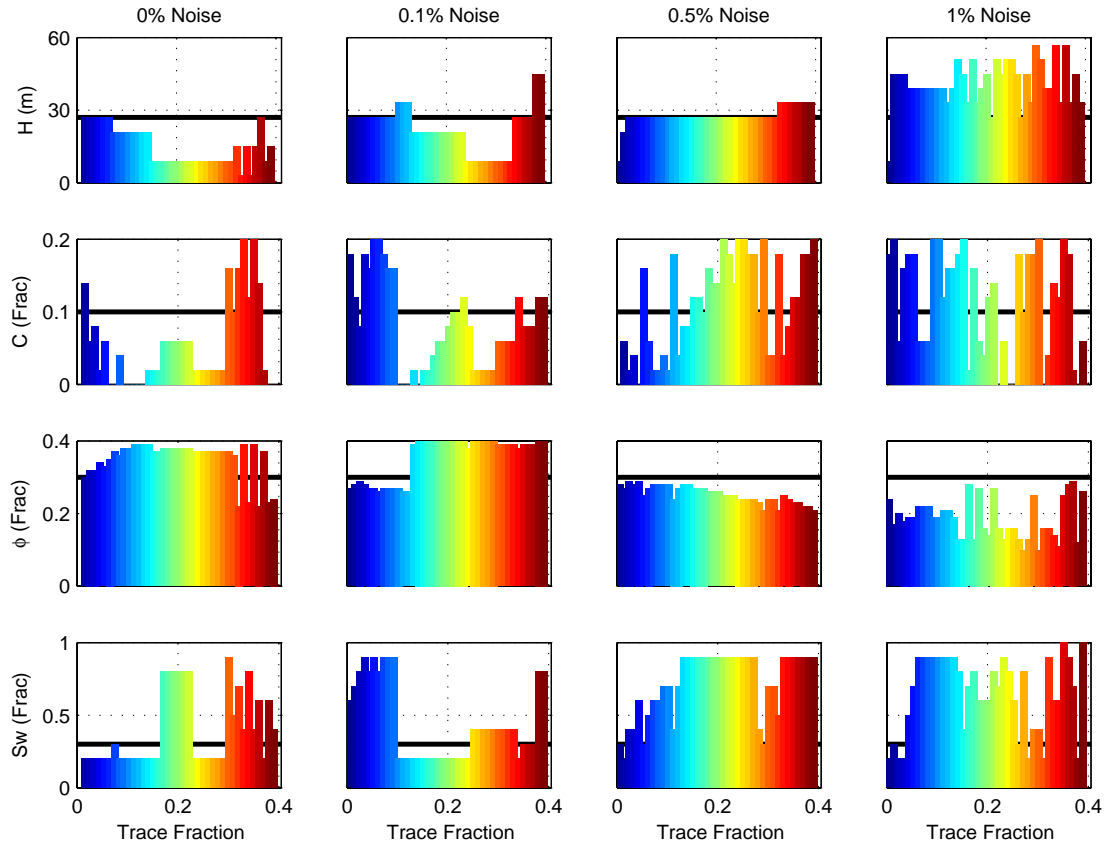
Figure 7.9. Most likely values from the full conditional posterior PDF. Accurate predictions of thickness-porosity-saturation combinations occur for noise levels less than 1% for certain accepted trace fractions.

Complementary to Figures 7.4-7.9 is a plot of the final correlation threshold as a function of the accepted trace fraction and noise level (Figure 7.10, left). Red corresponds to a high final threshold and blue to a smaller value. As expected, the correlation threshold drops as (1) the accepted trace fraction increases and (2) as the noise level increases. Figure 7.10 (right) displays the actual number of accepted synthetic traces as a function of noise level and trace fraction. This indicates how many combinations of synthetic reservoir models, out of 30690, were used to construct the posterior PDFs. If all traces were used without the acceptance/rejection criterion, computational memory requirements are too great to allow the numerical calculation of the likelihood function.
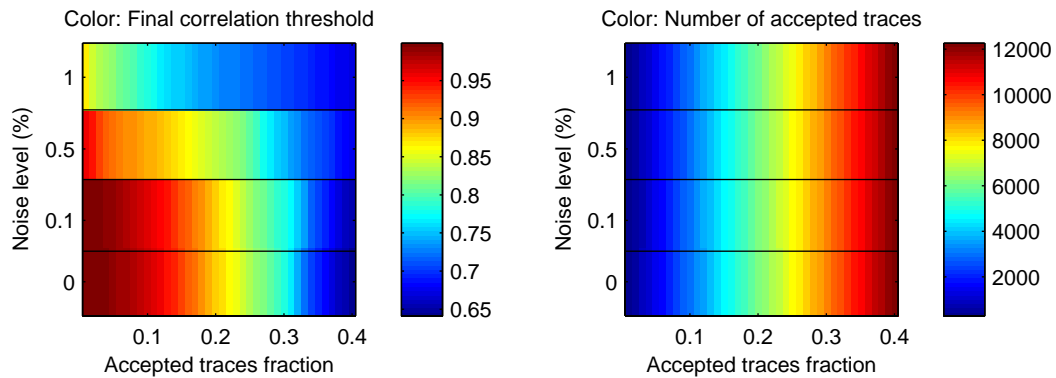
Figure 7.10 Final correlation values and number of synthetics accepted as a function of accepted trace fraction and noise level.

These two figures are important to display. The left figure, showing the final iterated correlation value, shows how low the threshold must become to accept the given number of traces. If it drops too low, to approximately 0.50, the correlation may become random, and the posterior PDFs would be constructed from this randomness. The plot on the right is important because enough traces must be accepted in order for the posterior PDFs to contain some scatter or uncertainty. If the number is too low, the solution approaches an incomplete deterministic state. If too many traces are accepted, the posterior PDFs are not substantially changed from their prior uniform states. Therefore, the inversion did not eliminate enough synthetic traces, and significant uncertainty lies in the posterior PDF.

7.4.3 Variable cross-correlation window lengths

This final test analyzes the inversion results when the length of the cross-correlation window varies from 40 to 320 ms (10 to 80 samples) with an increment of 16 ms. This is done for all four noise levels. First, the most likely values from the posterior PDFs are examined. Then a few selected posterior PDFs are analyzed along with some of the synthetic seismic traces. Looking at the reference seismic data (Figure 7.3), the travel-time thickness of the reservoir is 30 ms. When the cross-correlation window is defined, its center is located at the minimum amplitude corresponding to the top of the reservoir. Therefore, window durations shorter than 60 ms do not sample the lower portions of the reservoir.

The first set of results comes from the marginal most likely values. In these plots, the most likely value of the individual reservoir properties is plotted as a function of the corresponding window length. All four parameters exhibit noticeable variability as a function of window length and as a function of increasing noise in the seismic data. Blue corresponds to a 40-ms window and red to 320-ms window.
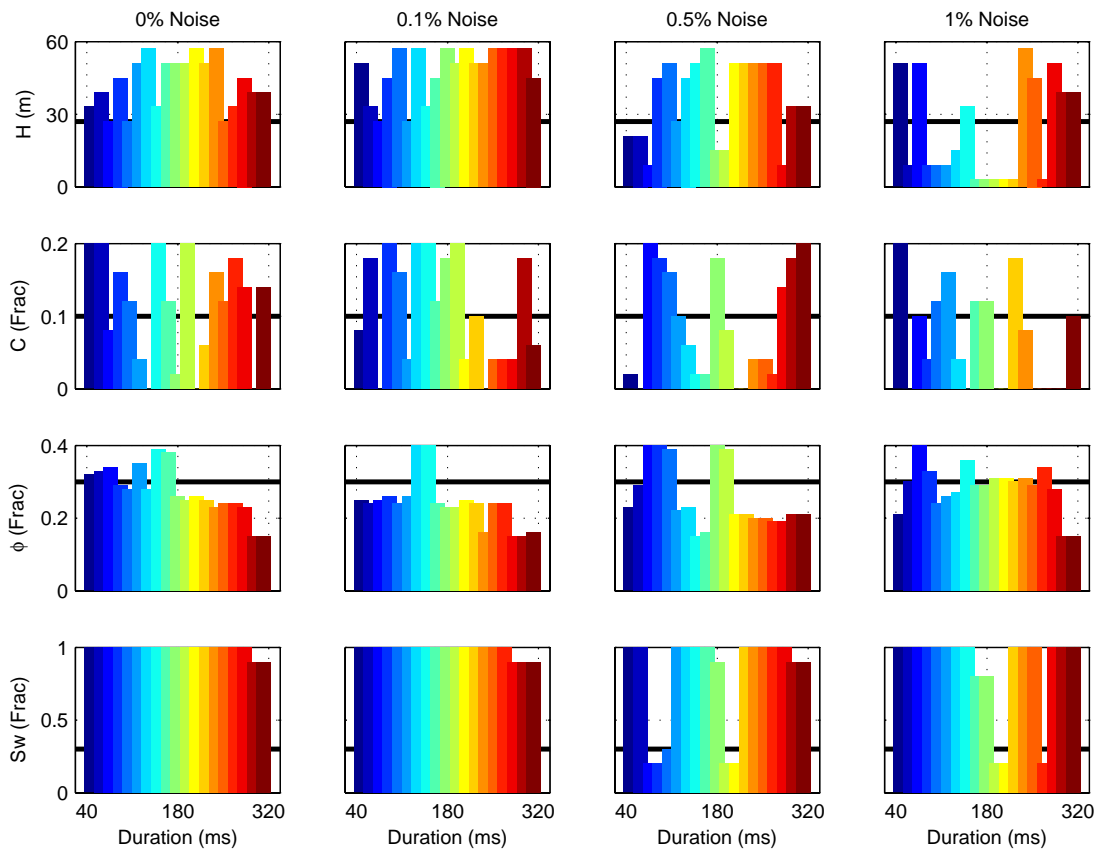
Figure 7.11 Marginal most likely values as function of cross-correlation window duration. Blue corresponds to 40 ms and red to 320 ms.

Next are the most likely values that come from the bivariate PDFs (Figure 7.12). Color is the same as in Figure 7.11, and the bivariate from which the value was drawn is indicated in the labels of the horizontal axes. As the noise increases, the changes in the predicted properties become more scattered. In addition, within a given noise level, the most likely values of H, C, and ϕ all change significantly, whereas S_w remains nearly constant. In the 0% noise case, it appears that H, C, and ϕ are all inaccurate. This is

due to the random selection of one most-likely combination. Notably, a trend appears of ϕ decreasing with increased window length. Some combinations of these values show very accurate results for some windows. Furthermore, the H-ϕ trade-off appears again. When noise reaches 0.1% to 0.5%, H is generally over-predicted and ϕ is under-predicted. For 1% noise, the relationship is difficult to discern.
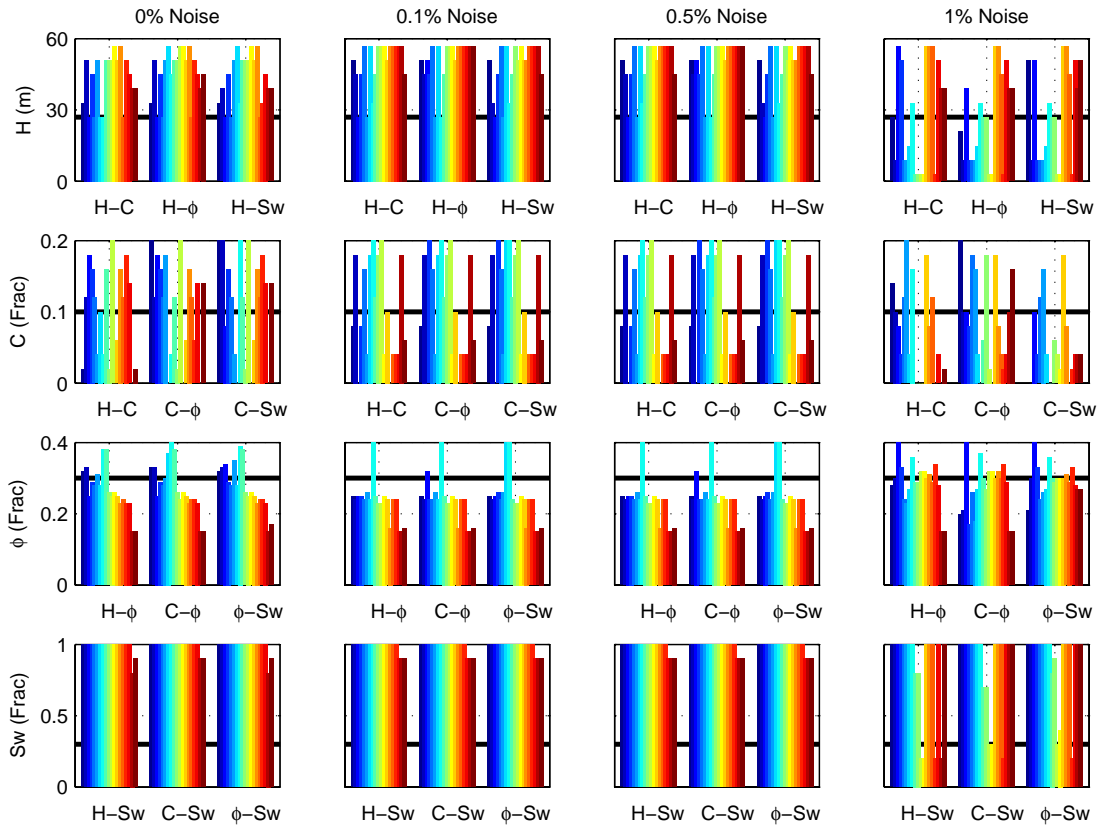
Figure 7.12 Most likely values selected from the six bivariate PDFs. Blue corresponds to 40 ms and red to 320 ms.

For the predictions from the trivariate PDFs, we expect H, ϕ, and S_w to be accurate (Figure 7.13). However, even for 0% noise, S_w is incorrect until the window duration is about 240 ms. Overall, H is over-predicted, and ϕ is under-predicted in all noise levels, for most windows. Significant scatter appears for both H and C for all four noise levels.
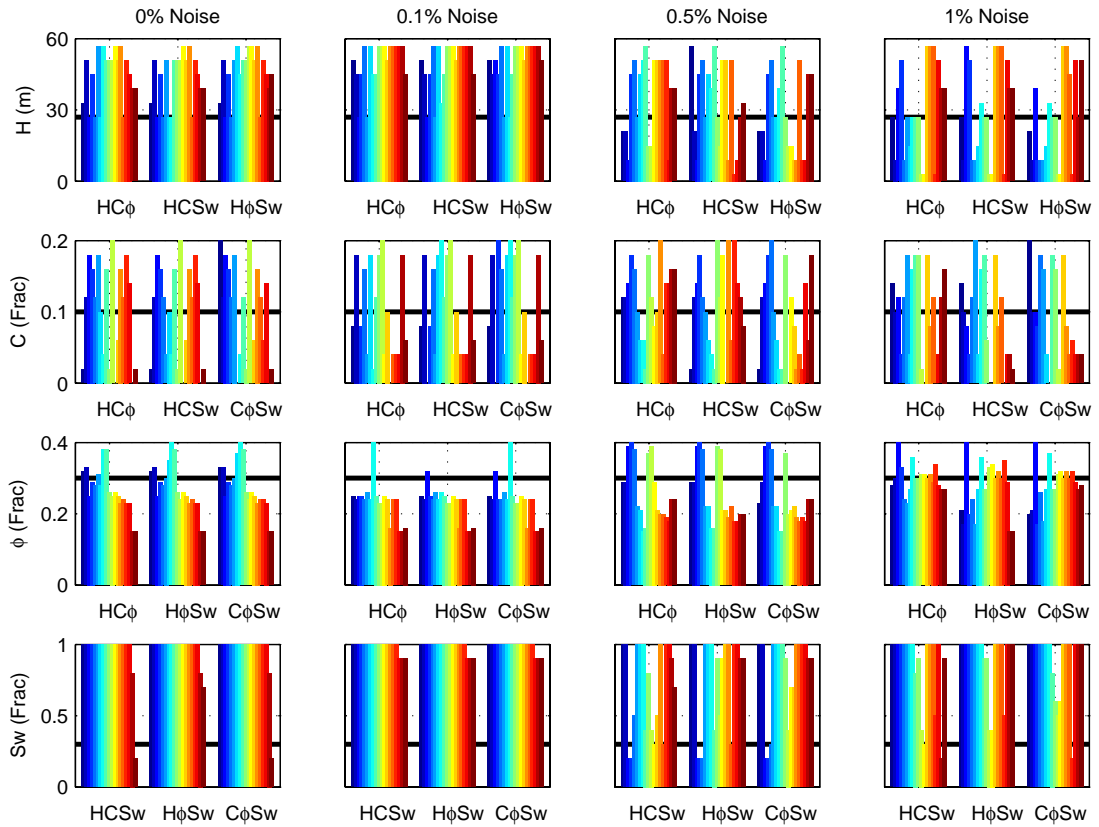
Figure 7.13 Most-likely values from the trivariate PDFs as a function of window length.

Next are the most likely values from the 4-D conditional PDF. Fairly good H and ϕ results occur for window lengths less than 60 ms and again greater than 232 ms, with noticeable scatter in C and S_w. Saturation is steadily predicted to be 1 until the window is >300 ms long. When noise increases to 0.1%, ϕ and H stabilize across the window-length axis. For 0.5%, noise, the H-ϕ relation holds, although it flips polarity for some windows. At 1%, the noise appears to take over, preventing reliable predictions.
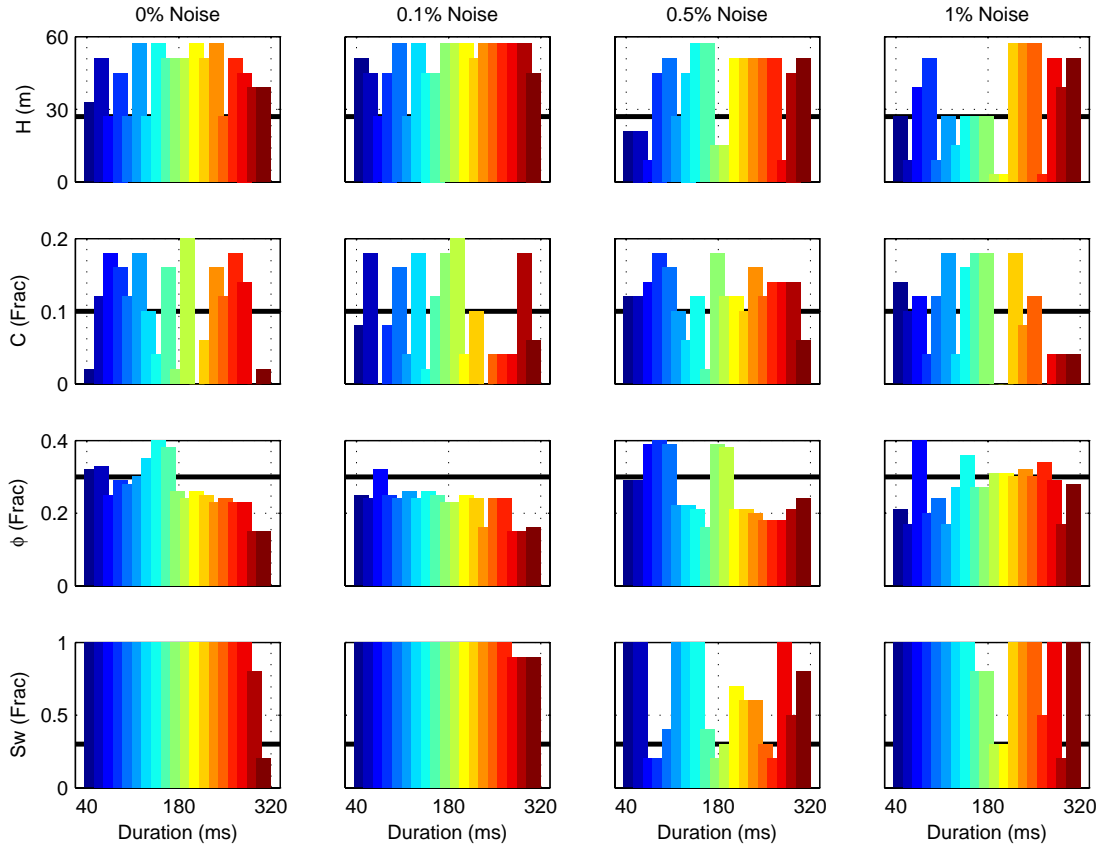
Figure 7.14. Most likely reservoir-property values as a function of window length, taken from the full conditional posterior PDF.

7.5 Discussion and conclusions

The first test regarding saturation predictions revealed that the inversion is capable of predicting saturation differences. This result has two implications. First, if the seismic signature of a gas sand is substantially different (i.e., opposite polarity) than that of brine sand, then the inversion reliably predicts the saturation differences. Second, the inversion may not be able to discriminate between small saturations, but it can predict the combinations of H, ϕ, and S_w that result in a similar seismic response. Clay content, however, remains a difficult parameter to quantify even in this synthetic scenario.

The sensitivity analysis of the inversion to the fraction of accpeted matching synthetic traces reveals some expected results. First, the informal objective function in the algorithm is to accept a minimum number of synthetic traces with a maximum correlation

value. The posterior conditional PDF is calculated from this minimum number of matches. If this number is too small, the posterior PDF does not represent the statistical solution. Conversely, if the number is too large, then the inversion does not reduce the prior uniform states enough for the posterior PDF to be informative. As expected, when substantial noise exists in the seismic data, the inversion struggles to find enough matching synthetic traces that have a high correlation coefficient. If a significant amount of noise is present and too few traces are accepted, it is difficult to determine whether the accepted traces match the real trace or the noise. The inversion may operate on noisy seismic data. However, to accept a suitable number of traces for a reliable posterior PDF, the correlation threshold may have to drop to a level at which random correlations provide the matching criteria. Therefore, properly applying the inversion to any dataset will require an estimate of the noise in the seismic data to aid in determining the fraction of synthetic traces to accept. This noise estimation and calibration step can be performed at the calibration well location, assuming the noise content away from the well does not change drastically.

The results from the variable cross-correlation window lengths show scatter within individual noise levels for all the most likely values. The explanation for this has to do with the cross-correlation calculation. After computing the cross-correlation function, the algorithm normalizes it by the geometric mean of the two input traces. The geometric mean is the square root of the product of the energies of the two traces (Sheriff, 1991). This is necessary to ensure that all the coefficients to fall between -1 and 1. Therefore, if one trace has a small energy, then dividing by that small number increases the observed correlation coefficients.

Figure 7.15 demonstrates this effect. On the left are traces for a $H = 27$ m, $C = 0.10$, ϕ from 0.1 to 0.4, and $S_w = 0.3$. On the right are traces with $H = 27$ m, $C = 0.10$, ϕ from 0.1 to 0.4, and $S_w = 1$. What we observe here is that for $\phi > 0.35$, $S_w = 0.3$ traces have a distinct trough that occurs at the reservoir level. However, for $S_w = 1$, it is quite apparent that the energies for traces with $\phi > 0.3$ are much less than for $S_w = 0.3$. The inversion accepts traces with both saturation values.
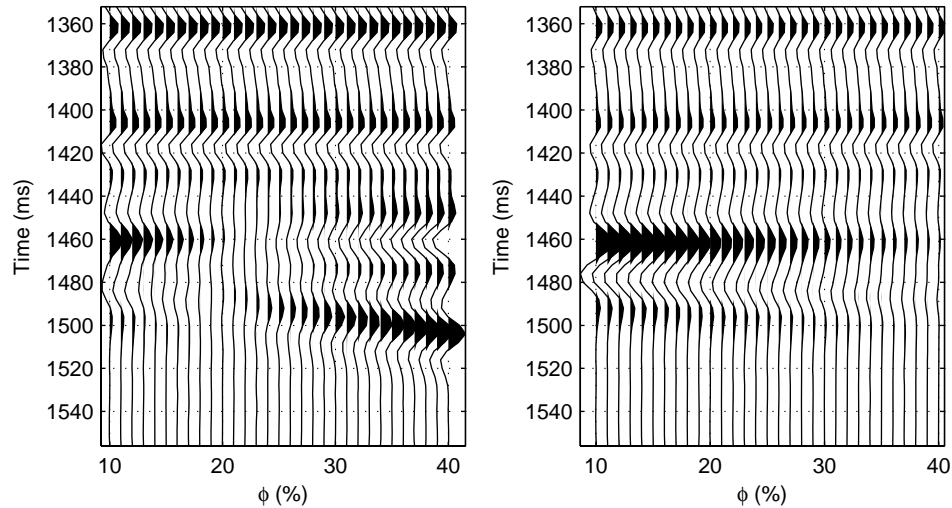
Figure 7.15. Synthetic seismic traces with 27-m thickness, clay content of 0.10, porosity from 10 to 40%, and saturation 0.3 on the left and 1 on the right. These traces, which differ by only saturation, illustrate the loss in energy in the high-porosity traces for high saturations.

The scatter observed in the plots of most likely values is a result of accepting traces with high probability of occurring with various combinations of the reservoir properties. Figure 7.16 shows a 90th percentile iso-probability surface through a PDF that illustrates this. The H-ϕ-S_w trivariate PDF comes from the 0% noise case with a cross-correlation window of 184 ms. It is clear that multiple areas of the PDF lie on this iso-probability surface. All ϕ values are contained on this surface, as are all S_w values. In addition, the smaller H values are present, as well as the largest H value. As can be seen, randomly selecting a H-ϕ-S_w combination from this surface provides many possible solutions.

Figure 7.16. Iso-probability surface through the thickness-porosity-saturation trivariate PDF for 0% noise and a cross-correlation window of 184 ms. It illustrates the many combinations of reservoir properties that are likely to occur, including some that do not represent the *in-situ* conditions.
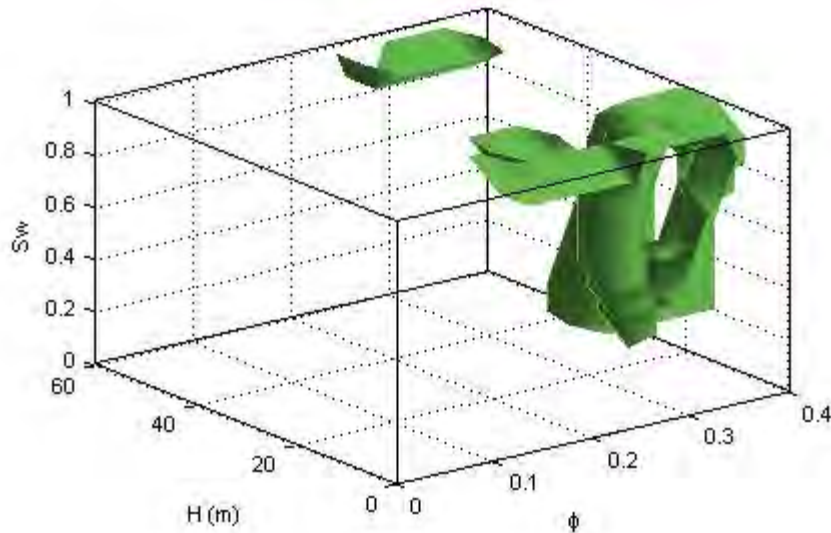
This effect of low energy was observed in previous chapters on real data. Varying the cross-correlation window exacerbated the sensitivity of the inversion to this energy factor. When this inversion is used, the results must be monitored and iterated to prevent this factor from coming into play. Alternatively, a different comparison scheme, such as the L_2 norm, could be implemented to avoid this situation. If this scheme is used, scaling the synthetic data to the real data becomes a serious issue that is avoided in the correlation routine.

In conclusion, the inversion is quite sensitive to the cross-correlation window duration for a given percentage of accepted traces. Therefore, to determine the optimal values for these parameters, they should be identified in a joint optimization scheme. All work up to this point, using both real and synthetic data, was done by experimentally finding these values. However, an algorithm could be defined to do this. It would likely come in the form of an objective function to minimize the number of matching traces, maximize the correlation, and minimize the window duration to speed the cross-correlation calculation.

Appendix
Guide to practitioners

A.1 Purpose

The purpose of this guide is to provide potential users and/or developers with a succinct and straightforward description of the workflow. As such, this appendix provides a guide for reproducibility. The steps and methods are described graphically in addition to supporting text. The relevant equations with comments for each workflow step are provided in Chapter 4.

A.2 Prior interpretation and rock physics model

For the inversion to run, a prior interpretation of the seismic data must demarcate the potential reservoir unit. Figure A.1 contains an example of this type of interpretation. Attribute analysis, structural or stratigraphic interpretation, or amplitude analysis are potential methods, already in practical use, that could provide the necessary prior interpretation.

A rock physics model is necessary to relate the elastic properties to the reservoir properties. It is established from calibration well data, from well data in an analogous setting, or is assumed if no well data are present. Although calibration well data could be used directly in the forward problem, use of the model regularizes the forward simulation and extends the data beyond the ranges present in the calibration well data (Figure A.1).
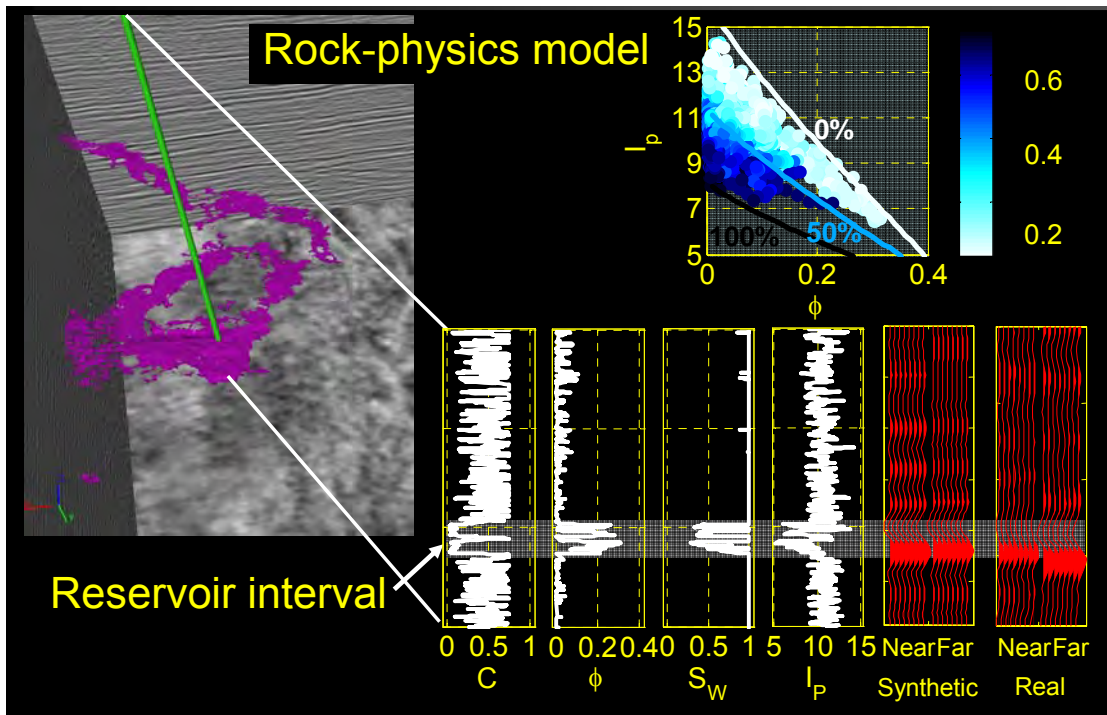
Figure A.1. Examples of the prior interpretation and rock-physics model established from calibration well data. Conventional interpretation methods could be used for the prior seismic interpretation. If well data are not available, a rock-physics can be assumed.

A.3 Forward problem

The first step of two in the forward problem is to define the ranges and increments of the model reservoir properties for prior uniform probability distribution functions (PDFs). These types of distributions are used to be as least-committal as possible. The ranges can be determined from geologic information and inferences based on well data. The increments can be defined by: (1) Directly estimating of the tolerance of the output to rough increments. (2) Determining the relative importance of the reservoir properties and assigning small increments to the most important parameters and larger values to the less significant ones. In this case, importance relates to how significantly a change in a reservoir property affects the corresponding elastic and seismic response. (3) Through an optimization routine that minimizes the number of combinations and assigns minimum increments that can be detected in the seismic data.

The second step in the forward problem involves the construction of three-layer models, in which the middle layer is the reservoir unit. Within the modeled reservoir unit, an exhaustive simulation of the modeled reservoir properties performed. Each model is converted to elastic properties, and synthetic seismic data are calculated for each model (Figure A.2). A convolution-based P-P ray-tracing algorithm (courtesy, Gary Mavko) was used throughout the chapters (Figure A.3). However, any synthetic seismogram algorithm could be used that appropriately models the real data. If zero-offset stack data from a geologically simple area are used, vertical incidence synthetic data may be sufficient. On the other hand, for a geologically complex area, the modeling algorithm may need to incorporate full-waveform effects.
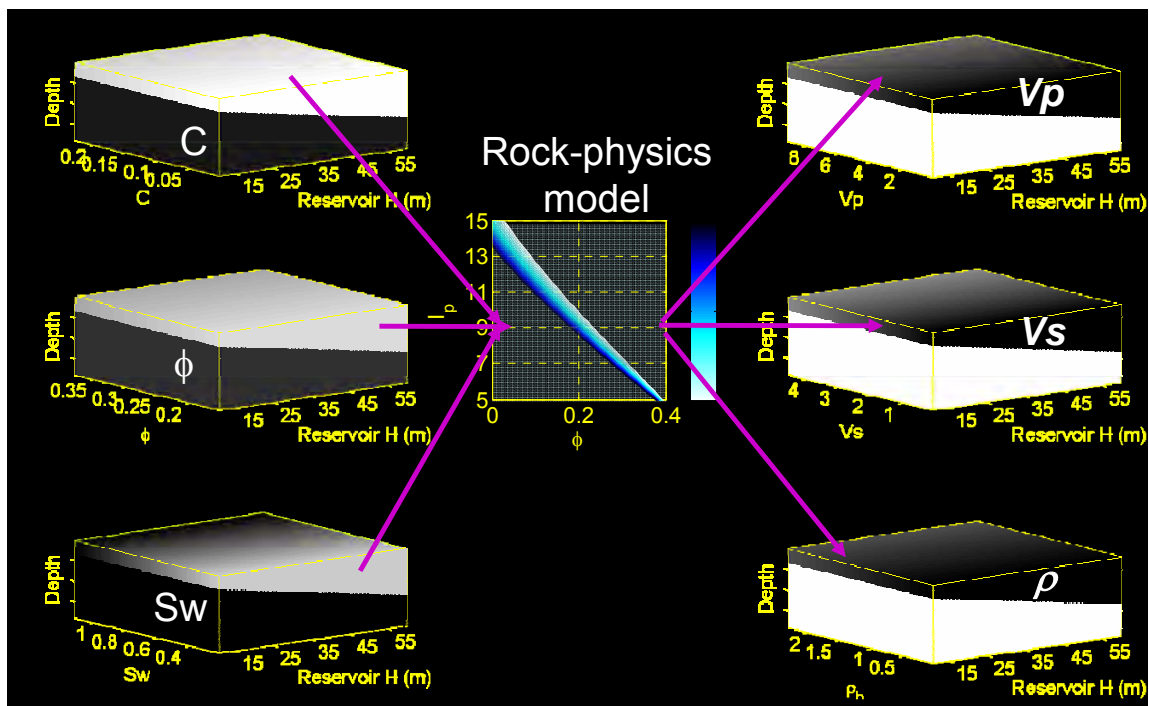

Figure A.2. In the forward problem, an exhaustive simulation of the model reservoir parameters is performed in the modeled reservoir unit. The rock physics model converts these values to the corresponding elastic properties.
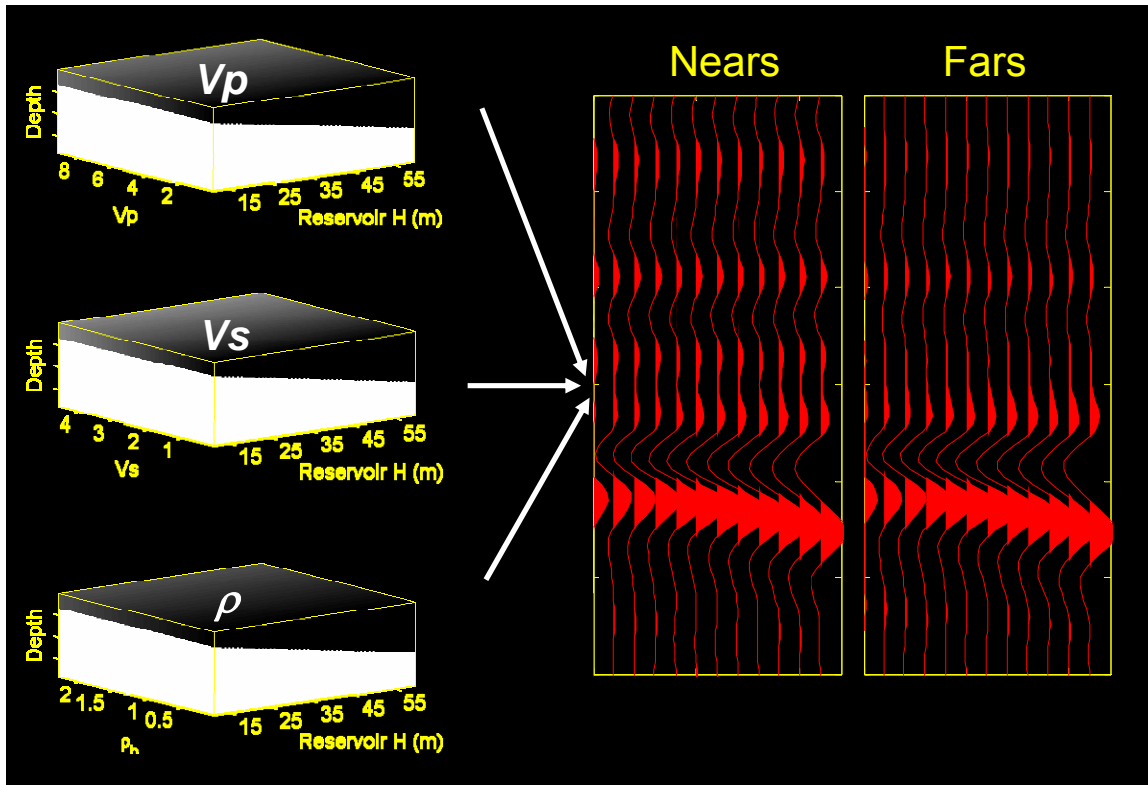
Figure A.3. Synthetic seismic data are calculated for each elastic-property model. Any algorithm to generate the synthetic data could be used as long as it includes enough wave-propagation effects to appropriately model the real data.

A.4 Inverse problem

In the inverse problem, windows are defined in the real and synthetic data around the potential reservoir unit (Figure A.4, left). Cross-correlation functions are calculated between the real traces and all the synthetic traces. After normalizing these functions by the geometric mean of the energies over the respective windows, the elemental cross-correlation coefficients (n and f) are found as the maximum value in the function. The full-grid search then finds the global maximum coefficients (N and F).
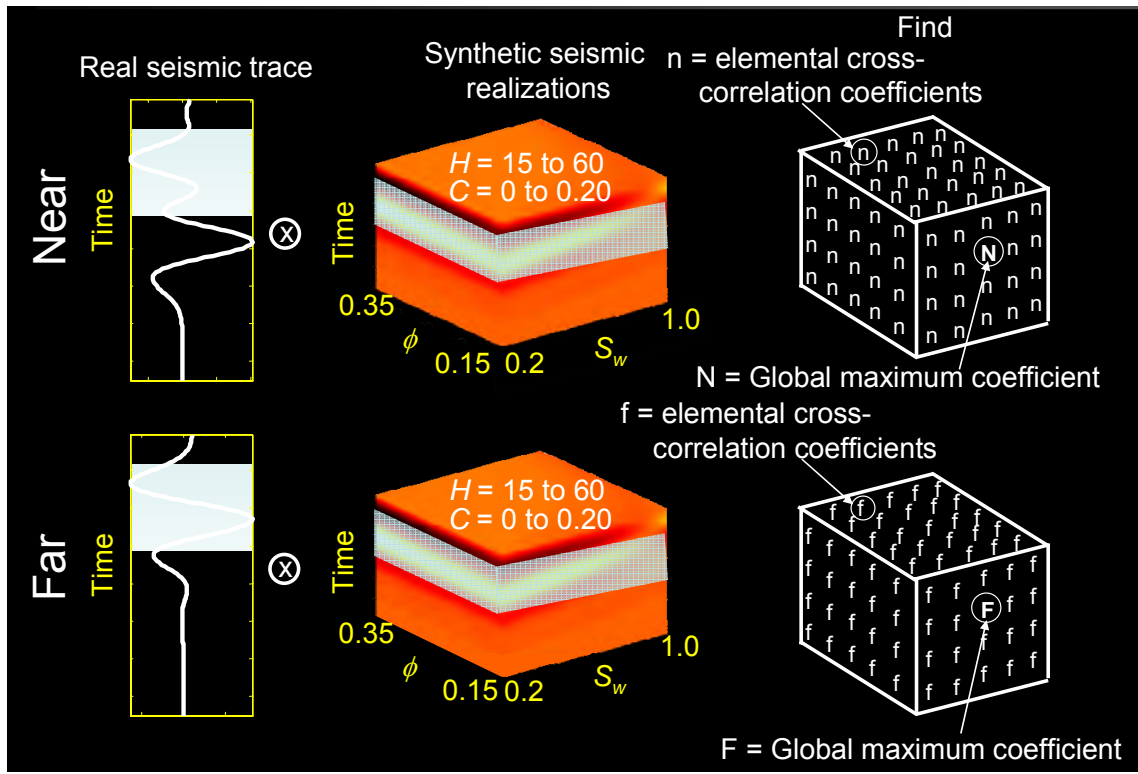
Figure A.4. Cross correlation provides the means of comparing the real and synthetic seismic traces. A full-grid search finds the global maximum coefficients (N and F) from the elemental coefficients (n and f).

After the elemental and global maxima coefficients are found, the acceptance/rejection criterion is implemented. The percentage of traces to accept (P) and the initial correlation threshold (ε) are defined (Figure A.5). To accept a given synthetic trace, both the near and far synthetic traces must match the real data within the correlation threshold. In all other instances, the synthetic traces are rejected. The model reservoir properties corresponding to the matching synthetic traces are used to construct the likelihood function. This function is non-parametric, and its shape and form are determined by the values P and ε.
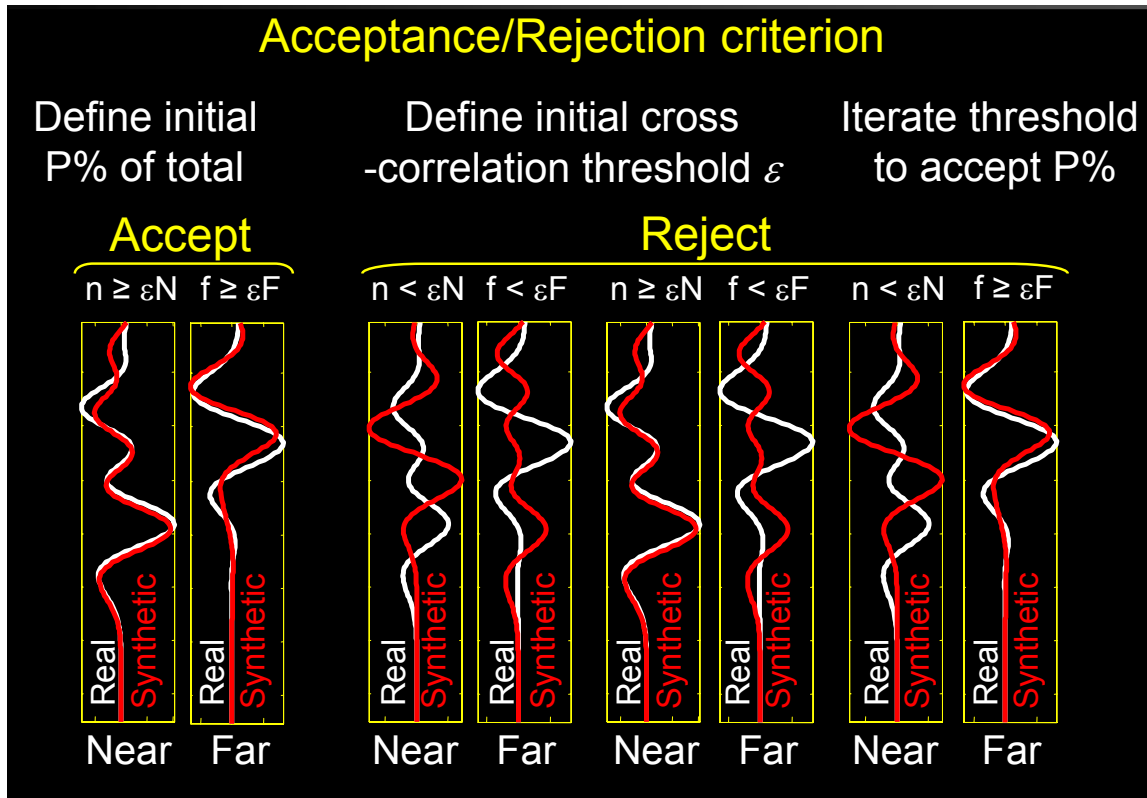
Figure A.5. The user defines the percentage (P) of synthetic traces to accept and the correlation threshold (ε). Both the near and far synthetic traces must meet or exceed the threshold in for them to be accepted.

A.5 Results and analysis

After the posterior distributions are calculated, the results at the calibration well should be analyzed to detect trends and patterns (Figure A.6). If no calibration well is present, then pseudo wells can be examined (see Chapter 7) to train the user to identify any trends. If the results do not match the calibration data, the prior ranges and increments can be modified. In addition P, ε, and the correlation-window length can be updated. Last, quality control can be performed by performing blind tests if additional well data are present.

Figure A.6. After performing the inversion, the posterior PDFs at the calibration well should be analyzed to identify any trends present. If trends appear, then the presence of them can be determined at locations away from the well data.
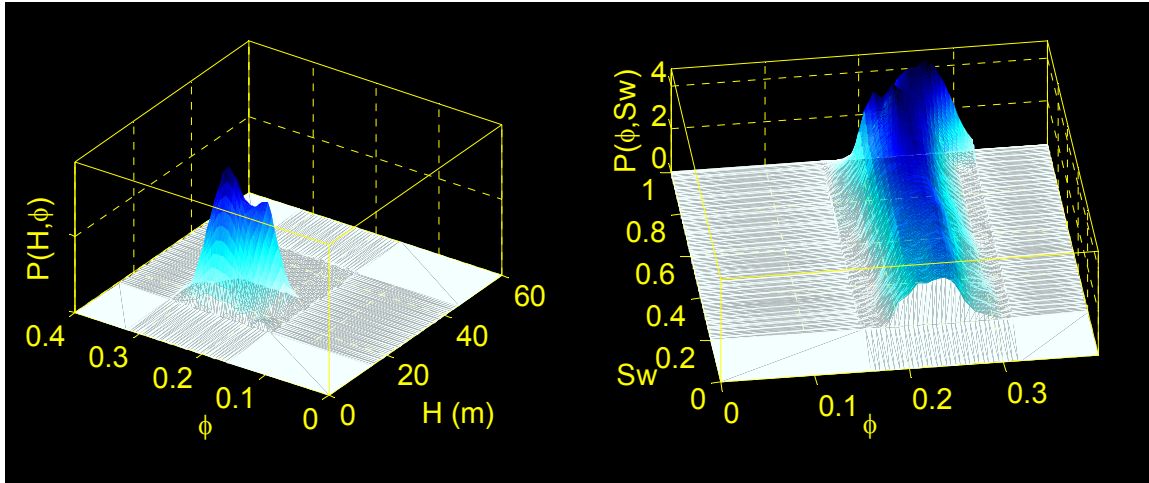
References

Acevedo, H., and W. D. Pennington, 2003, Porosity and lithology prediction at Caballos Formation in the Puerto Colón Oil Field in Putumayo (Colombia): The Leading Edge **22**, 1135–1141.

Avseth, P., J. Dvorkin, G. Mavko, and J. Rykkje, 2000, Rock physics diagnostic of North Sea sands: Link between microstructure and seismic properties: Geophysical Research Letters, **27**, 2761–2764.

Avseth, P., T. Mukerji, and G. Mavko, 2005, Quantitative seismic interpretation: Cambridge University Press.

Bachrach, R., 2006, Joint estimation of porosity and saturation using stochastic rock-physics modeling: Geophysics, **71**, no. 5, O53–O63.

Backus, G.E., 1962, Long-wave elastic anisotropy produced by horizontal layering: Journal of Geophysical Research, **67**, 4427–4440.

Batzle, M., and Z. Wang, 1992, Seismic properties of pore fluids: Geophysics, **57**, 1396–1408.

Bosch, M., 2004, The optimization approach to lithologic tomography: Combining seismic data and petrophysics for porosity prediction: Geophysics, **69**, 1272–1282.

Bosch, M., P. Barton, S. Singh, and I. Trinks, 2005, Inversion of traveltime data under a statistical model for seismic velocities and layer interfaces: Geophysics, **70**, no. 4, R33–R43.

Buland, A., and H. Omre, 2003, Bayesian linearized AVO inversion: Geophysics, **68**, 185–198.

Carlin, B. P., and T. A. Louis, 2000, Bayes and empirical Bayes methods for data analysis, 2nd ed.: Chapman and Hall.

Castagna, J. P., M. L. Batzle, and R. L. Eastwood, 1985, Relationships between compressional-wave and shear-wave velocities in clastic silicate rocks, Geophysics, **50**, 571–581.

Chen, J., G. M. Hoversten, D. Vasco, Y. Rubin, and Z. Hou, 2007, A Bayesian model for gas saturation estimation using marine seismic AVA and CSEM data: Geophysics, **72**, no. 2, WA85–WA95.

Coléou, T. Allo, F., Bornard, R., Hamman, J., and Caldwell, D., 2005, Petrophysical Seismic Inversion: SEG Expanded Abstracts **24**, 1355.

Connolly, P. and M. Kemper, 2007, Statistical uncertainty of seismic net pay estimations: The Leading Edge, **26**, 1284–1289.

Dvorkin, J., and M. A. Gutierrez, 2002, Grain sorting, porosity and elasticity: Petrophysics, **43**, 185–196.

Dvorkin, J., and A. Nur, 1996, Elasticity of high-porosity sandstones: Theory for two North Sea data sets: Geophysics, **61**, 1363–1370.

Gal, D., J. Dvorkin, and A. Nur, 1998, A physical model for porosity reduction in sandstones: Geophysics, **63**, 454–459.

—— 1999, Elastic-wave velocities in sandstones with non-load-bearing clay: Geophysical Research Letters, **26**, 939–942.

Gallop, J., 2006, Facies probability from mixture distributions with nonstationary impedance errors: 76th Annual International Meeting, SEG, Expanded Abstracts, 1801–1804.

Gassmann, F., 1951, Über die elastizität poröser medien: Vierteljahrsschrift der Naturforschenden Gesellschaft in Zürich, **96**, 1–23.

Gastaldi, C., D. Roy, P. Doyen, and L. Den Boer, 1998, Using Bayesian simulations to predict reservoir thickness under tuning conditions: The Leading Edge, **17**, 589–593.

Goldberg, I., and B. Gurevich, 1998, A semi-empirical velocity-porosity-clay model for petrophysical interpretation of P- and S-velocities: Geophysical Prospecting, **46**, 271–285.

González, E. F., 2006, Physical and quantitative interpretation of seismic attributes for rocks and fluids identification: Ph.D. thesis, Stanford University.

Greenberg, M. L. and J. P. Castagna, 1992, Shear-wave velocity estimation in porous rocks: Theoretical formulation, preliminary verification and applications, Geophysical Prospecting, **40**, 195–209.

Gunning, J., and M. E. Glinsky, 2004, Delivery: An open-source model-based Bayesian seismic inversion program: Computers and Geosciences, **30**, 619–636.

—— 2007, Detection of reservoir quality using Bayesian seismic inversion: Geophysics: **72**, R37–R49.

Han, D. -H., 1986, Effects of Porosity and Clay Content on Acoustic properties of Sandstones and Unconsolidated Sediments: Ph.D. dissertation, Stanford University.

Han, D.-H., A. Nur, and D. Morgan, 1986, Effects of porosity and clay content on wave velocities in sandstones: Geophysics, **51**, 2093–2107.

Hashin, Z., and S. Shtrikman, 1963, A variational approach to the elastic behavior of multiphase materials: Journal of Mechanics and Physics of Solids, **11**, 127–140.

Hill, R., 1952, The elastic behavior of crystalline aggregate: Proceedings of the Physical Society, **A65**, 349–354.

Kass, R., and L. Wasserman, 1996, The selection of prior distributions by formal rules: Journal of the American Statistical Association, **91**, 1343–1370.

Kowallis, B. J., L. E. A. Jones, and H. F. Wang, 1984, Velocity-porosity-clay content systematics of poorly consolidated sandstones: Journal of Geophysical Research, **89**, 10355–10364.

Larsen, A. L., M. Ulvmoen, H. Omre, and A. Buland, 2006, Bayesian lithology/fluid prediction and simulation on the basis of a Markov-chain prior model: Geophysics, **71**, no. 5, R69–R78.

Loures, L. G. L., and F. S. Moraes, 2006, Porosity inference and classification of siliciclastic rocks from multiple data sets: Geophysics, 71, no. 5, O65–O76.

Malinverno, A., and R. L. Parker, 2006, Two ways to quantify uncertainty in geophysical inverse problems: Geophysics, **71**, no. 3, W15–W27.

Marion, D., 1990, Acoustical, mechanical, and transport properties of sediments and granular materials: Ph.D. thesis (unpublished), Stanford University.

Mavko, G., C. Chan, and T. Mukerji, 1995, Fluid substitution: Estimating changes in Vp without knowing Vs, Geophysics, **60**, 1751–1755.

Mavko G., T. Mukerji, T. and J. Dvorkin, 1998, The rock physics handbook, Tools for seismic analysis in porous media, Cambridge University Press.

Mindlin, R. D., 1949, Compliance of elastic bodies in contact: Transactions of the American Society of Mechanical Engineers, **71**, A-259.

Neff, D. B., 1990, Incremental pay thickness modeling of hydrocarbon reservoirs: Geophysics, **55**, 556–566.

—— 1993, Amplitude map analysis using forward modeling in sandstone and carbonate reservoirs: Geophysics, **58**, 1428–1441.

Nur, A., G. Mavko, J. Dvorkin, and D. Galmudi, 1998, A key to relating physical properties to porosity in rocks: The Leading Edge, **17**, 357–362.

Raymer, D. S., E. R. Hunt, and J. S. Gardner, 1980, An improved sonic transit time-to-porosity transform: 21st Annual Meeting, Society of Petrophysicists and Well Log Analysts, Paper P.

Riedel, M., S. E. Dosso, and L. Beran, 2003, Uncertainty estimation for amplitude variation with offset (AVO) inversion: Geophysics, **68**, 1485–1496.

Scales, J. A., and L. Tenorio, 2001, Prior information and uncertainty in inverse problems: Geophysics, **66**, 389–397.

Sengupta, M., and R. Bachrach, 2007, Uncertainty in seismic-based pay volume estimation: Analysis using rock physics and Bayesian statistics: The Leading Edge, **26**, 184–189.

Spikes, K. and J. Dvorkin, 2005, Simultaneous model-based inversion for lithology, porosity, and fluid: Exploration Geophysics, **36**, 360–356.

Spikes, K. T. and J. P. Dvorkin, 2005, Gassmann-consistency of velocity-porosity transforms: The Leading Edge, **24**, 581–583.

Spikes, K., T., Mukerji, J. Dvorkin, and G. Mavko, 2007, Probabilistic seismic inversion based on rock-physics models: Geophysics, **72**, 5, R87–R97.

Tarantola, A., 1987, Inverse problem theory: Methods for data fitting and model parameter estimation: Elsevier Science Publ. Co., Inc.

Thomas, E.C., and S. Stieber, 1975. The distribution of shale in sandstones and its effect upon porosity: SPWLA Logging Symposium Transactions.

Tosaya, C.A., 1982, Acoustical properties of clay-bearing rocks: Ph.D. thesis, Stanford University.

Tosaya, C., and A. Nur, 1982, effects of diagenesis and clays on compressional velocities in rocks: Geophysical Research letters, **9**, 5–8.

Wyllie, M. R. J., A. R. Gregory, and L. W. Gardner, 1956, Elastic wave velocities in heterogeneous and porous media: Geophysics, **21**, 41–70.

Wyllie, M. R. J., A. R. Gregory, and L. W. Gardner, 1958, An experimental investigation of factors affective elastic wave velocities in porous media: Geophysics, **23**, 459–493.

Yin, H., 1992, Acoustic velocity and attenuation of rocks: Isotropy, intrinsic anisotropy, and stress induced anisotropy: Ph.D. thesis, Stanford University.